Investigating Disordered Positive Electrode Materials for Lithium-Ion Batteries Using $Li_{(1+x)}Ti_{2x}Fe_{(1-3x)}O_2$
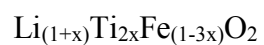
by

Stephen Glazier

Submitted in partial fulfillment of the requirements
for the degree of Master of Science

at

Dalhousie University
Halifax, Nova Scotia
August 2015

To my parents, who never doubted me, even when I did.

Table of Contents

List of Tables

List of Figures

Abstract

Typical positive electrode materials for lithium-ion batteries have ordered structures, containing well defined lithium percolation networks through the entire structure. Another type of structure which has until recently received little attention is the disordered rock-salt structure. These materials have in the past exhibited poor capacity and cycling performance due to the lack of structure-spanning lithium networks. Recent theoretical works have modelled the available lithium content in favourable sites for lithium percolation in various disordered structures.

This work compared the recent model to experimental results obtained from structural and electrochemical studies on $Li_{(1+x)}Ti_{2x}Fe_{(1-3x)}O_2$ ($0.00 \leq x \leq 0.28$) with various degrees of disorder, synthesised using solid state synthesis methods. Charge-discharge cycling studies of coin cells were used to confirm the model as well as to explore various cycling conditions and electrochemical mechanisms responsible for trends in performance. x-ray diffraction was used to characterize structural parameters and the degree of disorder at various temperatures and compositions. Fe and Ti K-edge x-ray absorption spectroscopy (XAS) of pristine materials and oxygen K-edge XAS of cycled electrodes were used to analyze structural trends and electrochemical processes such as oxygen charge compensation.

List of Symbols and Abbreviations Used

a, b, c	Unit cell lengths
α, β, γ	Unit cell angles
BSE	Back Scattered Electron
c	Speed of light
ccp	Cubic Close Packed
CE	Coulombic Efficiency
DEC	Diethyl Carbonate
DFT	Density Functional Theory
d_{hkl}	Plane spacing
EC	Ethylene Carbonate
EV	Electric Vehicle
EXAFS	Extended X-Ray Absorption Fine Structure
FY	Fluorescence Yield
G	Reciprocal lattice vector
h	Planck's constant
(*h k l*)	Miller indices
I	Intensity
ICE	Internal Combustion Engine
ICP	Inductively Coupled Plasma
ICP-OES	Inductively Coupled Plasma Optical Emission Spectroscopy
k	Wave vector
λ	Wavelength

linac	Linear accelerator
M-M	Metal – Metal bond
$\mu(E)$	Absorption coefficient
NMP	1-methyl-2-pyrrolidone
φ	Phase shift
Ψ	Wave function
ppb	Parts per billion
PVDF	Polyvinylidene fluoride
$\boldsymbol{q}$	Scattering vector
q	Capacity
RF	Radio Frequency
$\boldsymbol{R_s}$	Bravais lattice vector
SEM	Scanning Electron Microscopy
SOC	State Of Charge
TEY	Total Electron Yield
θ	Scattering angle
TM	Transition Metal
TM-O	Transition Metal – Oxygen bond
V	Voltage
XANES	X-Ray Absorption Near Edge Structure
XAS	X-Ray Absorption Spectroscopy
XRD	X-Ray Diffraction
Z	Atomic number

Acknowledgments

I would like to first thank my supervisor, Dr. Jeff Dahn for his support, suggestions, and criticisms. I have learned so much during my degree from him and know I can learn a great deal more in the future. I would like to thank my other committee member, Dr. Mark Obrovac for taking time to provide feedback on my work and reading this thesis.

Many thanks also go to the Dahn lab members, specifically Jim Li, John Camardese, and Ramesh Shunmugasundaram for their help, collaboration, and useful discussions on positive electrode materials.

I would like to thank the Canadian Light Source Synchrotron for their collaboration and hosting my internship from May to July 2015. I would like to thank members of the CLS Industrial Division Toby Bond and Jigang Zhou for their help in collecting data and cell preparation for XAS, as well as Joel Reid and Ning Chen for useful discussions on synchrotron XRD and XAS, respectively.

I would also like to thank the DREAMS program at Dalhousie and NSERC for providing financial support for this work.

Finally I would like to thank all of my family and friends for supporting me through this work. Without their support this would not have been possible.

Chapter 1: Introduction

1.1 Motivation for the Study of Lithium Ion Battery Positive Electrode Materials

Lithium ion batteries are currently used in many electronic applications as rechargeable energy storage devices. Typically in the past they have been implemented in portable electronics due to their high energy density, low cost and lifetime. Batteries used in portable electronic applications such as cell phones, laptop computers, tablets, smartwatches, *etc.* require a lifetime on the order of hundreds of cycles before other components reach their end of life or become obsolete. Other more recent applications of lithium ion energy storage include use in electric vehicles (EV) including range extended EVs which pair a small, traditional combustion engine with the electric system, as well as residential, commercial and grid level energy storage. These applications however require lifetimes on the order of thousands or tens of thousands of cycles to compare with existing technologies.

Electric vehicles have seen a surge of interest from the press and public in recent years with the contrast in increasing gasoline prices and decreasing price of large scale of lithium ion batteries, creating more economically and environmentally efficient consumer options over conventional internal combustion engine (ICE) vehicles. For comparison, the average commuter vehicle (classified as weighing less than 4.5 tonnes) in Nova Scotia was driven 16,802 km in 2009.[1,2] The average cost of gasoline in Nova Scotia in 2014 was $1.183 per litre.[3] Assuming a fuel efficiency of a standard mid-size passenger car to be equivalent to a 2015 Ford Fusion (5.6 L/100 km combined highway and city), the average annual fuel cost of a gasoline powered car in Nova Scotia would be $1113.10.[4] Table 1 compares prices and specifications of high and low end EVs currently on the market and their operating

costs per year. These estimates do not include maintenance costs, however EV annual maintenance costs have been reported up to 35% less than that of conventional ICE vehicles due to less complex components than required in an ICE.[5–7]

Table 1.1: Examples of EVs on the current automotive market [8–11]

Vehicle (2015)	Capacity (kWh)	Range (km)	Cost (USD)	Battery Cost (USD)	Electricity cost/yr. *	Cost/ yr.
Tesla Model S	85	435	$87500	$25000	$491	$3616
BMW i3	18.8	190	$42400	$13725	$249	$1964
Chevrolet Spark EV	23	122	$29170	$15000	$472	$2347
Ford Focus EV	23	132	$25995	$15000	$437	$2312

*Electricity costs = $0.14947 per kWh in Nova Scotia

Non-EV versions of the Focus and Spark are comparable to the EV price minus the battery cost. Therefore due to the battery cost of most EVs accounting for approximately half the cost of the vehicle, it is fair to combine the battery cost in the annual operating estimate, which accounted for 80-92% of the total yearly cost, where the rest was due to electricity costs. In comparison to the fuel cost per year in a gasoline vehicle, EVs are much more expensive to drive. In order for EVs to become a viable option for consumer transportation the cost of lithium ion technology must decrease by at least a factor of two. All of the batteries listed above claim a round trip efficiency greater than 90%, and energy costs contribute to 8-20% of operating costs, therefore improving efficiency would not lead to a substantial cost improvement.

One way to reduce the cost would be to increase battery lifetime. A warrantied lifetime of 8 years (or in most cases 160,000 km, whichever occurs first) may seem impressive, however, when compared to the large capacity and range, these systems are not expected to withstand a large number of cycles. Using the assumptions above, the average Nova Scotia driver would drive 134416 km in 8 years. Therefore the Telsa Model S is warrantied

for an equivalent of 302 cycles over 8 years of driving. The Chevrolet Spark EV is warrantied for an equivalent of 1101 cycles. These lifetimes are still on the order of most portable electronics and would need to be doubled in order to lower operating costs to that of gasoline vehicles. Improving rate performance, temperature and charge management, and internal chemistry are a few ways of improving the lifetime. Another way of reducing the cost of operating an EV is to decrease the cost of the battery itself. By using cost effective materials and synthesis methods the cost of a lithium ion battery can be substantially decreased. Using high energy density materials may also increase capacity and/or reduce the weight of a battery, increasing the range and in turn reducing the lifetime cost by reducing the number of cycles required throughout its lifetime. Materials containing Fe, Ti, Mn and Ni are of interest due to their low cost, and was the motivation for studying the $LiFeO_2$, Li_2TiO_3 solid solution in this work. If materials similar to the ones presented in this thesis are found to be commercially viable for applications such as EVs and grid storage, the energy storage portion of the cost of use could be significantly reduced.

The typical materials cost of a standard 18650 cylindrical lithium ion cell is shown in Table 2. For the purpose of this thesis, a cell refers to an individual lithium ion device, whereas a battery refers to a collection of cells connected and managed in a larger scale. The positive electrode material accounts for over 25% of the materials cost.

3

Table 1.2: Cost per component of a commercial 18650 cell in 2010 [12]

Cell Component	Cost (USD)
Positive Electrode Material (NMC)	$0.258
Aluminum Foil	$0.028
Separator	$0.209
Electrolyte	$0.219
Negative Electrode Material	$0.028
Copper Foil	$0.044
Binder	$0.029
Conductive Carbon	$0.003
Processing	$0.139
Packaging	$0.054
Total	$1.011

It must also be noted that these prices do not include the cost of a management system. In large applications such as EVs multiple cells are connected and temperature and charge regulated in order to monitor, improve, and optimize performance.

All components of lithium ion cells contribute to their cost, capacity, energy density, lifetime and safety. Though significant work has been done on all components, electrode materials have a profound impact on every aspect of cell improvement, specifically positive electrodes due to the high cost impact.

Since positive electrode materials account for a large portion of the cost of a Lithium ion battery and are a large contributor to the lifetime, energy density and capacity it is crucial to investigate new, cost effective positive electrode materials to implement in next generation large scale lithium ion technology.

1.2 Lithium Ion Batteries

1.2.1 Battery Components

The inner components of a lithium ion cell can be separated into four major components: positive and negative electrodes, separator, and electrolyte. The positive and negative electrode materials are typically coated double sided on aluminum and copper foil current collectors, respectively. The separator is then rolled between the electrodes in a "jelly roll" configuration, as shown in Figure 1.1. The electrolyte is then injected into the cell and wets the separator.

The positive electrode is a mixture of active material, typically a lithium transition metal (TM) oxide such as $LiCoO_2$ (LCO), a binding agent such as polyvinylidene difluoride (PVDF), and a carbon conductor such as carbon super-S. The negative electrode is a mixture of active material (typically graphite) and binder. A typical separator is made from a porous polyolefin thin film which allows ion transport in the electrolyte between electrodes. Electrolytes are composed of a lithium salt such as lithium hexaflourophosphate ($LiPF_6$) typically dissolved in an organic carbonate mixture such as ethylene carbonate (EC) mixed with diethylene carbonate (DEC).
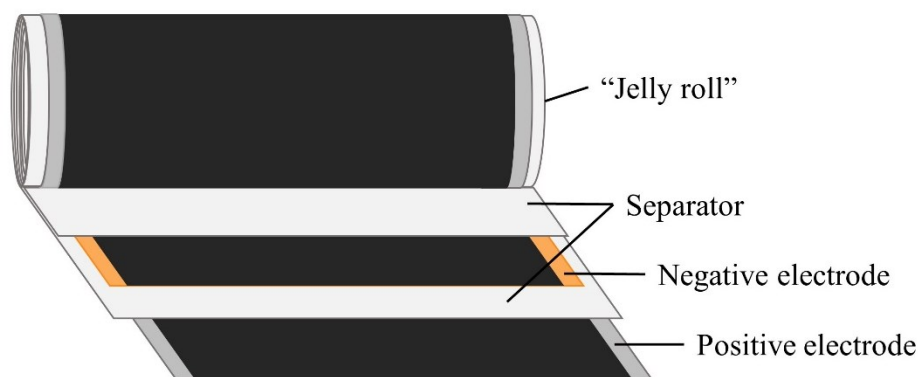
Figure 1.1: The typical "jelly roll" configuration of a commercial cylindrical lithium ion cell

Figure 1.2 demonstrates the basic operation of a lithium ion cell: Upon charge, when a current is applied from the negative to the positive electrode in an external circuit, lithium ions are extracted (deintercalate) from the positive electrode structure and inserted into the negative electrode structure (intercalate). A lithiated negative electrode material has higher chemical potential than a positive electrode material, thus the energy supplied to charge the cell is "stored" in the negative electrode. When a load is connected to a charged cell, the reverse process occurs spontaneously, and electrons flow through the circuit from negative to positive electrode using stored energy to perform work in the circuit. The positive electrode shown in Figure 1.2 is $Li_{1-x}CoO_2$, an ordered-layered material, and the negative electrode is graphite (Li_xC_6). At a completely discharged state $x = 0$, and at a charged state $x = 0.7$, meaning during charge Li^+ ions move from positive to negative electrode (left to right in figure), and the reverse on discharge, as described above.
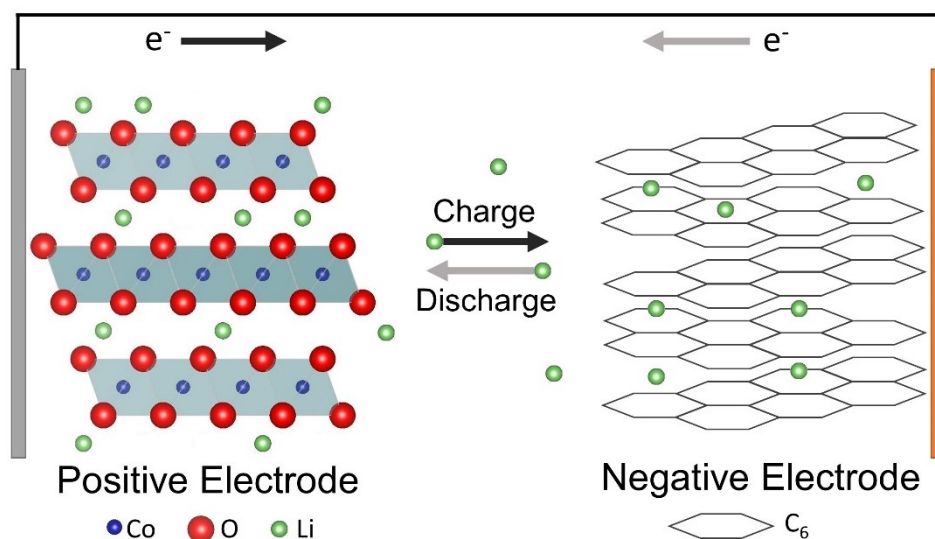
Figure 1.2: A simplified model of electrode interaction during charge and discharge of a Lithium ion cell. The separator and electrolyte are not included for simplicity.

The performance and lifetime of a cell depend on the materials chosen for each component. For the purpose of this thesis, and for reasons described in the previous section, only positive electrode materials will be discussed in detail.

1.2.2 Positive Electrode Materials

Many different structures and chemistries have been found to reversibly intercalate/de-intercalate lithium ions. In order for a structure to facilitate these changes it must satisfy at minimum two structural requirements:

1. The structure must facilitate reversible "migration networks" for lithium to intercalate and de-intercalate

2. The networks must span the entire structure

Many structures fulfill these requirements, most of such structures are ordered-layered and spinel structures. Figure 1.3 illustrates two ordered-layered structures, rhombohedral $R\bar{3}m$ and monoclinic C2/m as well as cubic spinel $Fd\bar{3}m$. In layered structures such as $LiCoO_2$ ($R\bar{3}m$), oxygen, lithium and transition metals arrange into separate layers. Two-dimensional networks are formed in the lithium layer allowing reversible lithium percolation between layers of CoO_2. In monoclinic C2/m such as Li_2MnO_3 it is useful to write the formula in terms of the layer populations, *ie.* $Li[Li_{0.33}Mn_{0.67}]O_2$. Transition metals (TM) in the TM layer order into a hexagonal super-lattice surrounding Li sites. In the spinel structure such as $LiMn_2O_4$ shown in Figure 1.3, lithium "tunnel" networks are formed.

$LiCoO_2$ is still currently used in many commercial applications due to its stable capacity of up to 190 mAh/g and lifetime of several thousand cycles.[13,14] Significant work has been done on layered TM oxides in order to reduce the amount of Co present due to its cost and toxicity. Replacing Co with Mn and Ni in materials such as $Li(Ni_{0.33}Mn_{0.33}Co_{0.33})O_2$ (NMC) has shown improvements in capacity, cycle life, and safety over traditional LCO and is gaining popularity in commercial cells.[15–22] Work by Brown *et al.* and McCalla *et al.* that used combinatorial methods characterised single phase regions in the Li-Ni-Mn-Co-O system and allowed for specific regions of interest to be targeted for study.[18,19]
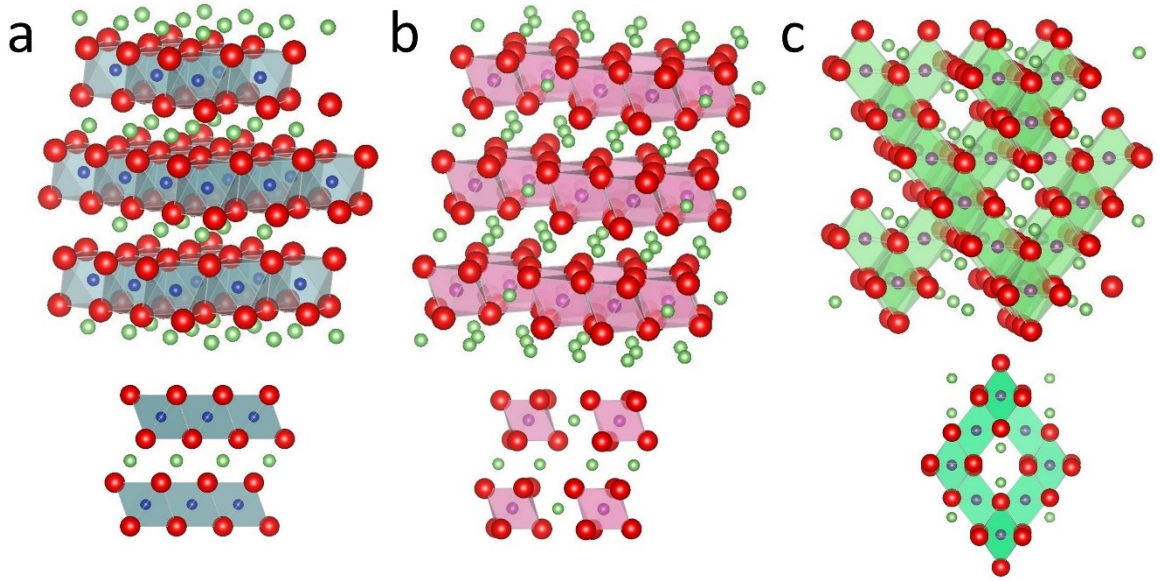
Figure 1.3: Bulk structure (upper) and site geometry (lower) of common layered a) R$\bar{3}$m and b) C2/m and spinel c) Fd3m space groups. Red atoms are oxygen, green lithium and coloured atoms in oxygen polyhedral are transition metals.

Some works in layered materials have focussed on lithium-rich materials such as Li[Li$_{0.02}$Mn$_{0.56}$Ni$_{0.16}$Co$_{0.8}$]O$_2$ in order to increase the amount of available lithium, increasing the capacity and energy density of the material.[23] In lithium rich materials, excess lithium is contained in the TM layer.

Another type of layered structure that has not seen much interest until recently is the disordered cubic rocksalt structure, Fm$\bar{3}$m. This structure will be discussed in detail in the following section.

1.3 Disordered Electrode Materials

The disordered rocksalt (Fm$\bar{3}$m) structure is a layered structure of the form Li$_{(1+x)}$M$_{(1-x)}$O$_2$ in which lithium and TM share the same site and are randomly distributed in the metal

layer in octahedral sites, as shown in Figure 1.4. These materials such as α-LiFeO₂ (shown

in Figure 1.4) have not received very much attention due to their poor electrochemical

performance.[24–26] When cations and lithium are not ordered in the structure their ability to

satisfy the two conditions mentioned in the previous section becomes limited. Potential

percolation networks are no longer simple slabs or linear paths, but rather they are complex

winding networks that may terminate in the bulk before reaching the surface.   In Figure

1.4a, multiple lithium atoms are trapped in the structure by iron rich regions and have no

path to the surface, while some regions have more lithium population and form a large

network.   Figure 1b shows a closer view of a section with lithium deficient (left) and rich

(right) regions.   As this pattern is expanded to a bulk level, very few uninterrupted

percolation networks are left.
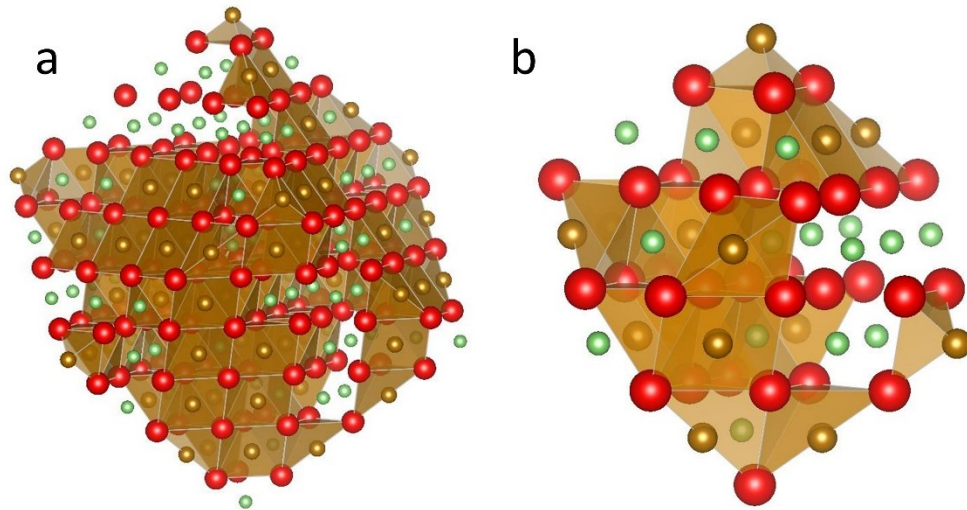
Figure 1.4: Disordered rocksalt Fm$\bar{3}$m. TM and Li atoms occupy the cation sites, randomly distributed through the structure.   Oxygen atoms are red, lithium green, and TM brown.

Lee *et al.* and Urban *et al.* recently have described the building blocks of lithium percolation networks in layered materials as "n-TM channels".[27,28]   The use of the word channel misrepresents the geometry of these building blocks, so this thesis will use the term n-TM sites instead. This notation refers to tetrahedral sites with oxygen at each vertice, where each face neighbours a Li or TM octahedral site.   The number of TM surrounding the tetrahedral site is represented by "n". For example, as shown in Figure 1.5a, ordered-layered $R\bar{3}m$ contains both 1-TM and 3-TM sites, where lithium diffusion through tetrahedra can occur in 1-TM sites, giving way to the 2-D slab networks mentioned earlier.   Disordered $Fm\bar{3}m$, however, does not have such clearly defined distribution and arrangement of sites due to the random distribution of lithium and TM.   This leads to a statistical distribution of 0, 1, 2, 3 and 4-TM sites depending on the lithium content. These sites are shown in Figure 1.5b. Therefore as the lithium content is increased, the probability of finding large, structure spanning networks increases.
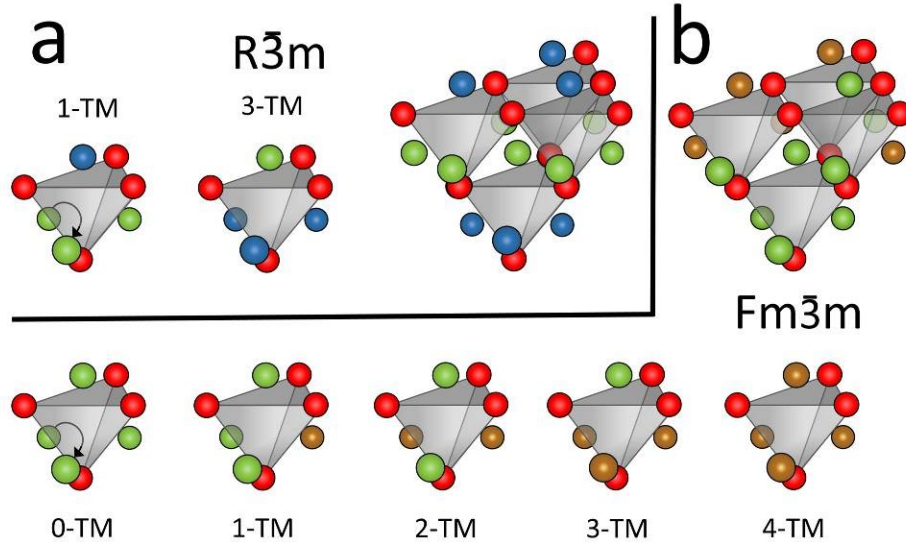
Figure 1.5: a) 1-TM and 3-TM sites present in ordered R$\bar{3}$m and their bulk "slab" arrangement b) n-TM sites n = 0..4 present in disordered Fm$\bar{3}$m and an example of bulk arrangement. Green atoms represent lithium, red oxygen, and blue/brown represent transition metals.

The probability of finding each n-TM site can be calculated using the stoichiometry of Li$_{1+x}$M$_{1-x}$O$_2$ with $0.00 \leq x \leq 0.33$. The probability of each site type (p_{nTM}) is shown in Figure 1.6 and was calculated using

$$p_{0TM} = \left(\frac{1+x}{2}\right)^4 ,$$

(1.1)

$$p_{1TM} = \left(\frac{1+x}{2}\right)^3 \left(\frac{1-x}{2}\right)^1 ,$$

(1.2)

$$p_{2TM} = \left(\frac{1+x}{2}\right)^2 \left(\frac{1-x}{2}\right)^2 ,$$

(1.3)

12

$$p_{3TM} = \left(\frac{1+x}{2}\right)^1 \left(\frac{1-x}{2}\right)^3 ,$$

(1.4)

$$p_{4TM} = \left(\frac{1-x}{2}\right)^4 .$$

(1.5)
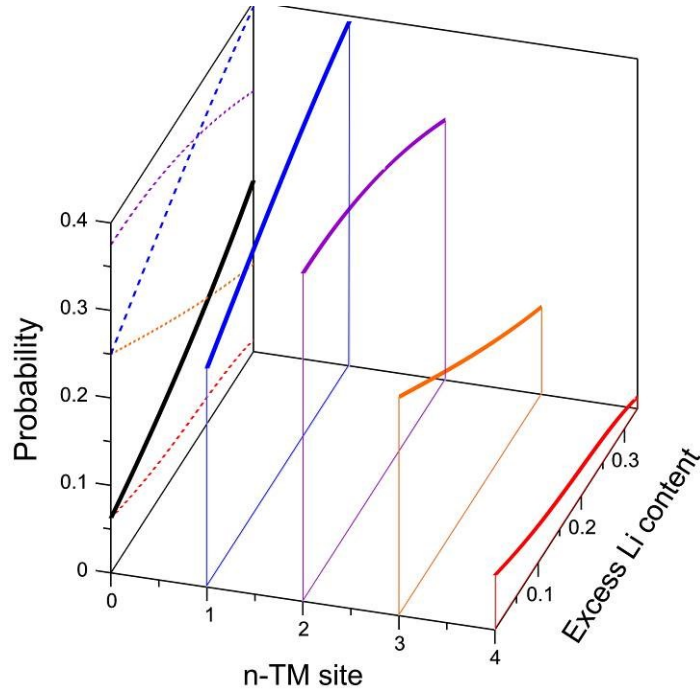
Figure 1.6: The probability distribution of n-TM sites with increasing lithium content. As lithium is increased from $x = 0$ the normal distribution around 2-TM becomes weighted towards 0 and 1-TM.

With increasing lithium content the distribution centered about 2-TM sites shifts towards 0-TM and 1-TM sites.

Lithium diffusion occurs through oxygen tetrahedra from one lithium site to another, as shown above by the curved arrows in Figure 1.5. In this case, lithium diffusion can occur, if energetically favourable, in 0, 1 and 2-TM sites. However, Lee *et al.* also showed

using density functional theorem (DFT) that due to smaller layer spacing in disordered materials, only 0-TM sites allow for lithium diffusion.[27] Considering Figures 1.4 and 1.6 it becomes clear why stoichiometric disordered LiMO$_2$ materials perform poorly: When expanded to a bulk system (hundreds of nanometers), the likelihood of a percolating network of lithium to span to the surface of the structure is extremely unlikely since only 7% at $x = 0.00$ to 20% at $x = 0.33$ of all sites are 0-TM. Therefore a method of determining the critical lithium content in order to form percolating networks, and determining how much lithium is available in those networks, is needed.

Two methods of finding the probability of a percolating network are the "brute force" method, using statistics and nearest neighbour geometry, and Monte Carlo methods. Considering the first approach, each lithium ion is located in an octahedral site, surrounded by 8 n-TM oxygen tetrahedra. Each surrounding tetrahedra is at maximum 3-TM, as they all contain the central lithium. The octahedral lithium can therefore be part of between zero and eight 0-TM networks. Therefore the probability of lithium being in at least one 0-TM site (p_{0TMnn}) can be found using a choose summation of n sites (n = 1..8)

$$p_{0TMnn} = \sum_{n=1}^{8} \binom{8}{n} (p_{0TM})^n (1 - p_{0TM})^{8-n} \ ,$$

$$(1.6)$$

where p_{0TM} is as described in Equation 1. Expanding to the next nearest neighbour, the probability that any the (minimum) two 0-TM sites connect to a third (p_{0TMnnn}) is then

$$p_{0TMnnn} = \left(\sum_{n=1}^{8} \binom{8}{n} (p_{0TM})^n (1 - p_{0TM})^{8-n} \right) \left(\sum_{k=1}^{7} \binom{7}{k} (p_{0TM})^k (1 - p_{0TM})^{7-k} \right) .$$

$$(1.7)$$

14

This calculation method continues to become more intensive with increasing cluster size. In order to calculate on a large scale Monte Carlo simulations are necessary.

Lee *et al.* recently performed Monte Carlo simulations with increasing lithium content, as well as increasing disorder, or cation mixing, where disorder is defined as the ratio of TM in the lithium layer to the total TM population, or $\frac{TM_{Li}}{TM}$.[27] This was performed using computational percolation methods developed by Newman and Ziff.[29] In the method, 0-TM sites were distributed randomly throughout a bound lattice based on the lithium population probability as well as layer mixing probability. Each time a 0-TM site was placed, the algorithm checked adjacent sites. Each time an adjacent 0-TM site was found the algorithm labels both sites as part of the same network, or "cluster", and labels the root of the cluster as the first site. If one cluster connected with another the larger of the two was used to define the new cluster and the root of the larger cluster then defined all sites in the new cluster. If two sites in the same cluster were joined by an intermediate site, the difference in displacement from the intermediate and two joined sites to the root site was determined, and within the lattice boundary was equal to one lattice spacing. When a boundary site was placed the algorithm checked the corresponding opposite boundary for a 0-TM site as well. If the opposite boundary was a 0-TM site and also in the same cluster as the placed boundary, "cluster wrapping" occurred, which returned a root displacement difference of greater than one spacing and all sites in the cluster become a structure spanning percolating network. A simplified diagram of a 2-dimensional square grid is shown in Figure 1.7.

The periodic wrapping probability is the probability this wrapping occurs in a certain sized bound region at specific lithium and disorder levels. The periodic wrapping

15

probability was found by Lee *et al.* to converge for layered structures around a 16x16x16 lattice (4096 sites), showing little improvement using a 32x32x32 lattice (32768 sites) and computing in significantly less time.[27] The ratio of accessible lithium was then found by the ratio of lithium in wrapped pathways (all non-wrapping pathways are trapped) to the total lithium content.
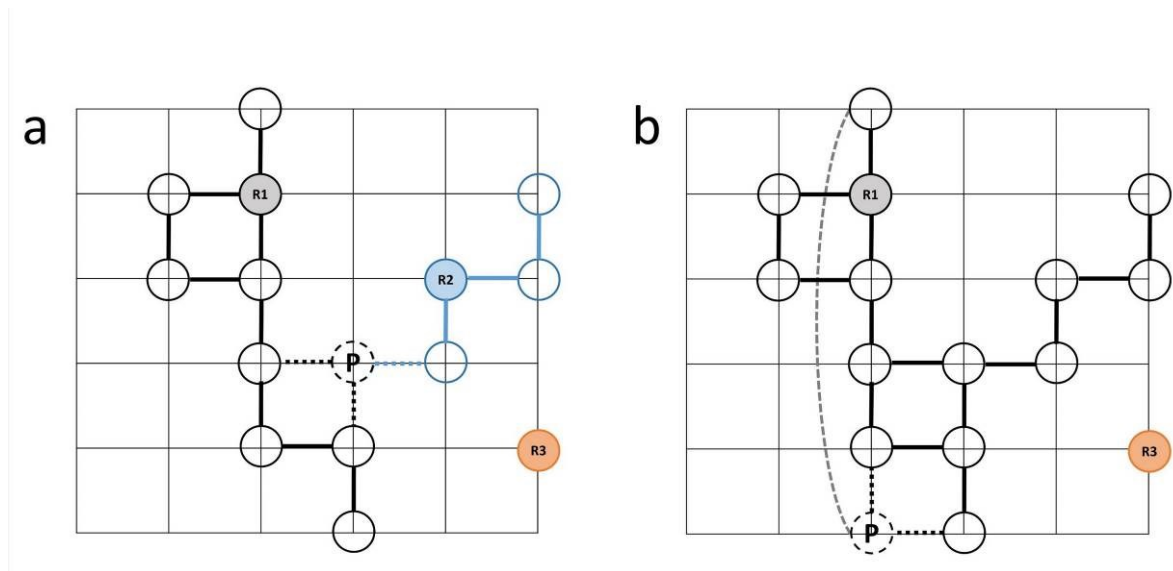
Figure 1.7: A simplified diagram of the site placement algorithm. In a) three root sites R1, R2, and R3 exist. When site P is placed, the cluster with root R2 becomes part of cluster R1.   In b), when P is placed "cluster wrapping" is achieved as the difference in displacement from joined networks and P to R1 is greater than one lattice unit.

The purpose behind this type of algorithm and the use of cluster wrapping is that if a sufficiently sized bound region is found to "wrap" consistently at a specified lithium content, then when expanded to bulk scale, 0-TM sites will exist through the entire structure. The results from Lee *et al.* are shown in a "heat map" in Figure 1.8. The accessible lithium content is shown from red (zero accessible lithium) to blue (1.5 lithium per formula unit). The black line in Figure 1.8A is x_c, the critical lithium concentration for 0-TM percolation. This map only considers 0-TM percolation, where, as disorder levels

decrease, layer spacing will increase until 1-TM and possibly 2-TM sites are favourable, but that is out of the scope of this thesis.
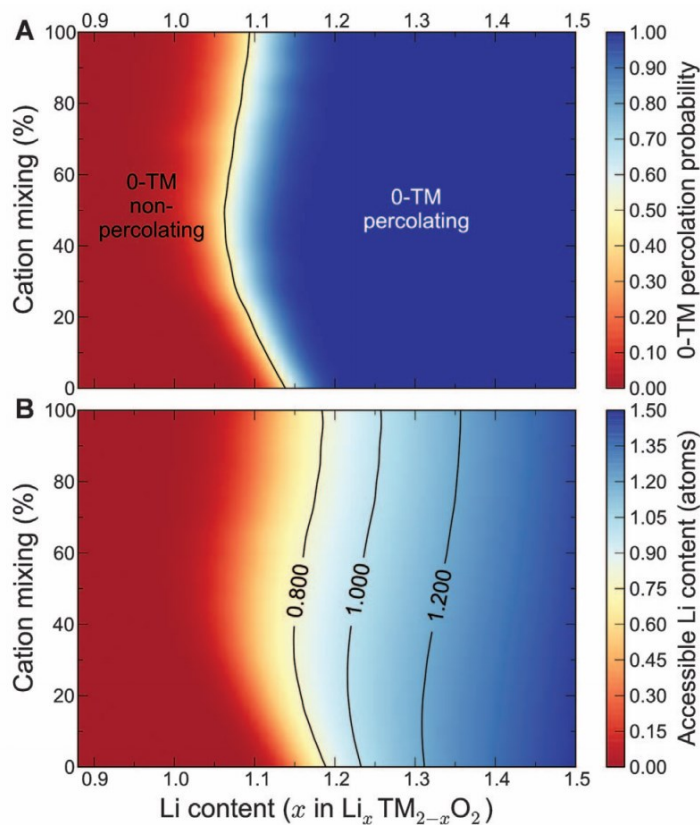
Figure 1.8: Results of Monte Carlo simulations by Lee *et al.* showing A) the periodic wrapping probability and B) Accessible lithium content in 0-TM percolating networks. From Lee, J., Urban, A., Li, X., Su, D., Hautier, G., Ceder, G. *Science* (2014), **343**, 519–522. Reprinted with permission from AAAS.

Figure 1.8 demonstrates that regardless of disorder, sufficient lithium, above $x \approx 0.20$ in $Li_{(1+x)}M_{(1-x)}O_2$ (note x is defined differently in Figure 1.8) is required in order for approximately one lithium per formula unit to be accessible. In a disordered rocksalt structure disorder is 100%. The available lithium *vs.* x data from the 100% mixing line in Figure 1.8B is shown by a black line in Figure 1.9.
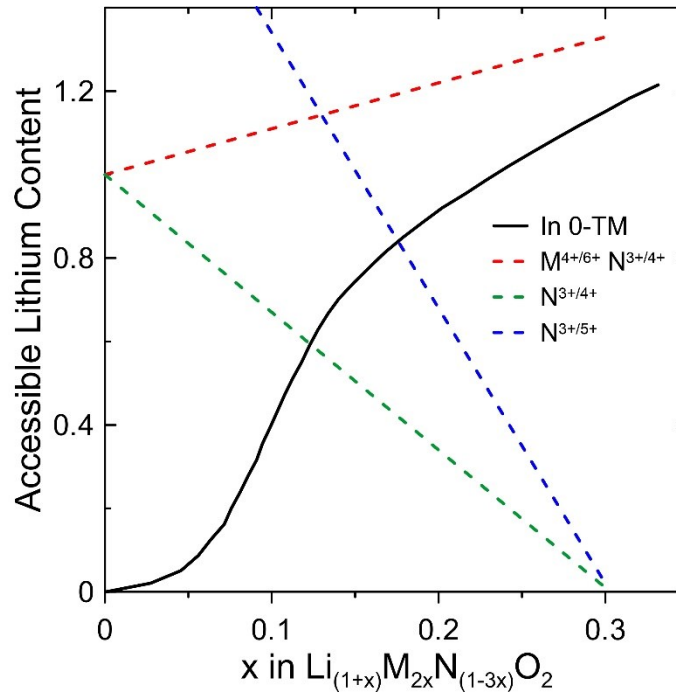
Figure 1.9: Available lithium content with increasing x due to 0-TM networks (black line), $M^{4+/6+}$ and $N^{3+/4+}$ redox, $N^{3+/4+}$ redox, and $N^{3+/5+}$ redox. For the latter two choices increasing lithium content decreases theoretical capacity once the redox and 0-TM lines intersect. 0-TM data digitized from Urban et al. [28]

Increasing lithium content increases the number of 0-TM sites available, however typical TM choices in electrode materials such as Co, Mn, Ni and Fe limit the theoretical amount of useful lithium due to their redox capabilities. As x increases, the average charge of $Li_{(1+x)}M_{(1-x)}O_2$ must remain zero. It is then useful to write the formula as $Li_{(1+x)}M_{(1-x)y}N_{(1-x)(1-y)}O_2$, where y is determined by charge balancing the chemical formula depending on cations M and N When M has a charge of 4^+ and N a charge of 3^+, the formula becomes $Li_{(1+x)}M_{2x}N_{(1-3x)}O_2$ where $0 \leq x \leq 0.33$. Depending on the possible oxidation states of M and N the theoretical capacity can be very low at high x. Three examples are shown in Figure 1.9. It should be noted that redox limited materials have been found to overcome limited capacity by exhibiting anion redox, such as in the case of Li_2MnO_3.[30]

In the work by Lee *et al.,* layered $Li_{1.211}Mo_{0.467}Cr_{0.33}O_2$ was found to disorder during charge/discharge cycling. The redox capabilities of Mo and Cr are that of the red line in Figure 1.9 therefore all available 0-TM lithium should have been accessible. The predicted capacity of the percolation model agreed very well with experimental results, however only the $x = 0.211$ composition was reported.[27,28]

Since these recent models have come to light, there has been more interest in disordered materials. Twu *et al.* investigated disordered $Li_xNi_{2-4x/3}Sb_{x/3}O_2$, finding increasing lithium increased capacity as well as capacity retention over many cycles.[31] Yabuuchi *et al.* investigated materials of the form xLi_3NbO_4-(1-x)MO and xLi_3NbO_4-(1-x)LiMO$_2$ with inactive Nb^{4+} which achieved high capacity from reversible oxygen redox (O^{2-}/O^{1-}) charge compensation up to 300 mAh g^{-1}.[32]

Past work on disordered materials, specifically of the form $Li_{(1+x)}Ti_{2x}Fe_{(1-3x)}O_2$ have found low reversible capacity and varying electrochemical performance with variations in lithium content, offering no explanation for the observed capacities.[24,25] Materials containing Ti and Fe are of great interest due to their low cost, safety, and availability. They are also of interest to this work for their reported ability to form a disordered structure along the compositional line $Li_{(1+x)}Ti_{2x}Fe_{(1-3x)}O_2$ to at least $x = 0.2$.[25]

Due to the necessity of high lithium content in disordered positive electrode materials, more work in understanding charge compensation processes such as oxide redox is necessary, as well as multi-redox transition metals such as $Mo^{4+/6+}$. Additionally, to date no work has shown experimental evidence of disordered materials following the percolation theory model Lee *et al.* predicted.

1.4 This Thesis

The primary goal of this thesis is to validate theoretical models by Lee *et al.* and aid in the understanding and design of disordered positive electrode materials. This work aimed to experimentally support Lee's models on highly disordered materials by synthesising a $Li_{(1+x)}Ti_{2x}Fe_{(1-3x)}O_2$ solid solution line from $0 \leq x \leq 0.33$ and observing how increasing lithium and decreasing redox capacity affected the performance of the material. Structural and electrochemical characterisation the material both pristine and *ex-situ* at multiple states of charge (SOC) was used to answer the following questions:

1. Can the degree of disorder be precisely characterised and controlled?

2. Do models by Lee *et al.* predict experimental performance of disordered materials?

3. What are the electrochemical mechanisms present in disordered materials and how do they limit performance?

4. How can charge compensation *via* oxygen redox aid in optimizing capacity and material design?

Chapter 2 of this thesis describes the experimental methods used in this research. Chapter 3 describes the results of structural and chemical characterisation of the synthesised materials. Chapter 4 will discuss the electrochemical results and compare Lee's model with this work. Chapter 4 and 5 will address question 4 using different charge-discharge protocols and *ex-situ* x-ray Absorption studies. Chapter 6 will discuss conclusions and propose future work. By answering the above questions, this work will aid in the future development of disordered material theory and design of novel, high capacity positive electrode materials.

Chapter 2: Experimental

2.1 Experimental Design

The solid solution (2x) $Li_2TiO_3 \bullet$ (1-3x) $LiFeO_2$ ($0.00 \leq x \leq 0.33$) was chosen due to its ability to exhibit high levels of cation disorder at different values of x as well as its expected $Fe^{3+/4+}$ redox reactions during charge and discharge.[24,25] In this document the simplified notation $Li_{(1+x)}Ti_{2x}Fe_{(1-3x)}O_2$ will be used.

Seven compositions were chosen along the solid solution ranging from $x = 0.00$ to $x = 0.30$. According to redox capacity, at $x = 0.33$, Li_2TiO_3 should have zero capacity due to electrochemically inactive Ti. If the model by Lee *et al.* is correct, $LiFeO_2$ should exhibit near zero capacity as well, as no 0-TM sites should form spanning networks. Therefore to form an understanding of how 0-TM and redox affect disordered materials, choices of x were spaced between endpoints: $x = 0.00, 0.05, 0.10, 0.15, 0.20, 0.23, 0.30$.

Synthesis conditions were varied in order to investigate the effect of temperature on structure as well as performance. Elemental analysis was performed in order to determine the exact compositions using inductively coupled plasma optical emission spectroscopy (ICP-OES). ICP-OES results were used in the refinement of powder x-ray diffraction (XRD) data, used to structurally characterize samples. XRD refinements were used to determine sample phases, lattice parameters and disorder (cation mixing). Scanning electron microscopy (SEM) was used to determine particle size and morphology. x-ray absorption spectroscopy (XAS) techniques probed local electronic and atomic structure to determine TM and oxygen valence states as well as TM migration during charge. Finally, test coin cells were made and electrochemical characterisation was

performed using charge/discharge cycling in order to compare performance to theoretical models.

The following sections outline each of the techniques mentioned above in detail, as well as the procedures used in this work for each technique.

2.2 Materials Synthesis

Chosen compositions were synthesised by mixing appropriate ratios of lithium carbonate (Li_2CO_3) (Chemetall, $\geq$ 99%), iron (iii) oxide (Fe_2O_3) (Sigma-Aldrich, $\geq$ 99%), and titanium dioxide (TiO_2) (Fisher, $\geq$ 99%). Powder precursors were made by mixing the measured amounts by hand in a mortar and pestle for 5 minutes with 5% and 10% excess lithium (over the target composition) to account for lithium loss during heating. 5 g of each lithium excess composition was synthesized (7 compositions x 2 excess contents) except x = 0.15, where 20 g of the 10% excess Li sample was synthesized for temperature dependence experiments.

Precursors with 5% excess Li were heated for 20 hr at 700°C while 10% excess samples were heated at 800°C. Heating was performed in a Vulcan 550 Benchtop Muffle Furnace (NeyTech) with both heating and cool down rates of 10°C/min. 3 g of each sample (2.5 for x = 0.30) was heated in an alumina ceramic "boat". Figure 2.1a shows the precursor materials and 2.1b shows the heated materials at each temperature. Precursors ranged from brick red (x = 0.00) to a very light red at x = 0.30. After heating, the 800°C series gradually transitioned from dark brown (x = 0.00) to light brown (x = 0.30) and the 700°C series started as a dark red-brown and transitioned to a light brown, except for the x = 0.20 composition, which was a light yellow-brown. The transition of the samples to lighter

colour with increasing lithium content is an indicator of the band gap of the samples. A material with a larger bandgap will absorb less wavelengths of light and therefore reflect more colours, so lighter samples should be less conductive. This "rule of thumb" may explain why larger amounts of carbon conductor was needed in order for cells to perform well in Section 4.1.
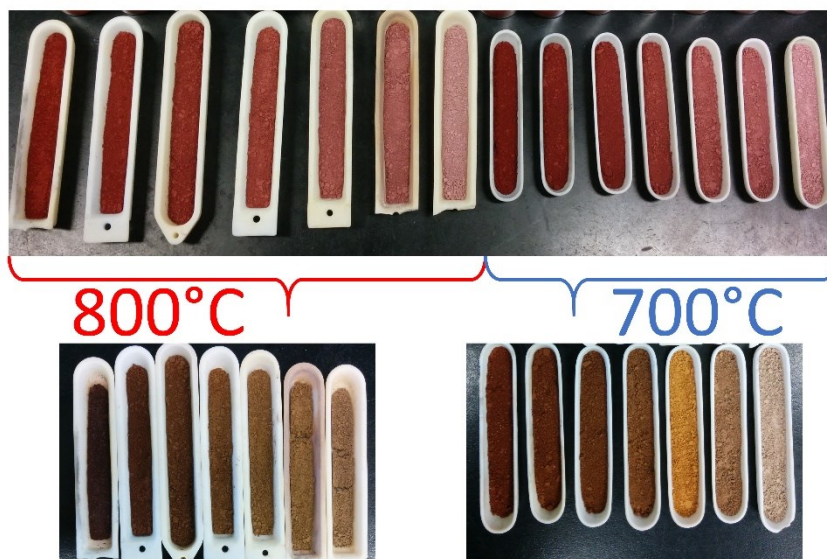
Figure 2.1: Powder precursors (top) and heated samples (below) heated at 800°C (left) and 700°C (right). Samples increase in x from left ($x = 0.00$) to right ($x = 0.30$).

Samples were then weighed and compared with the expected mass of the target composition (assuming all 5-10% excess lithium was lost during heating). These results are shown in Table 2.1. Almost all samples were within 2% of the expected mass, however the 800°C $x = 0.30$ composition had 5.4% excess mass over the target. This may have been due to poor weighing technique (loss of sample), as the 700°C sample was within 2.7% of target mass, or the $x = 0.30$ samples may have contained multiple phases or excess Li_2CO_3

after heating. The characterization of phases and exact compositions are explained in the following sections.

In addition to the two series above, the $x = 0.15$ composition was heated to 600°C, 700°C , 750°C, 800°C, 900°C, and 1000°C in a separate experiment, under the same conditions above. These masses were not recorded.

Table 2.1: Mass analysis for 700°C and 800°C series

x (700°C)	Precursor (g)	Heated (g)	Expected (g)	Difference (g)	% Difference
0.00	3.00	2.39	2.40	-0.01	-0.42%
0.05	3.04	2.45	2.39	0.06	2.45%
0.10	2.98	2.34	2.30	0.04	1.71%
0.15	2.99	2.34	2.26	0.08	3.42%
0.20	3.04	2.28	2.25	0.03	1.32%
0.23	3.02	2.25	2.21	0.04	1.78%
0.30	3.04	2.20	2.14	0.06	2.73%
x (800°C)					
0.00	3.02	2.44	2.41	0.03	1.23%
0.05	3.02	2.40	2.37	0.03	1.25%
0.10	3.00	2.36	2.31	0.05	2.12%
0.15	3.01	2.33	2.28	0.05	2.15%
0.20	3.00	2.26	2.22	0.04	1.77%
0.23	3.02	2.23	2.21	0.02	0.90%
0.30	2.49	1.86	1.76	0.10	5.38%

2.3 Elemental Analysis

2.3.1 ICP-OES

Elemental analysis is a technique widely used to determine trace elements as well as accurately determine overall compositions of materials. The technique used in this work is inductively coupled plasma optical emission spectroscopy (ICP-OES).

An inductively coupled plasma (ICP) is created by a copper radio frequency (RF) coil. Between 700-1500 W is supplied to the RF coil at a frequency 27-40 MHz.[33] This creates electromagnetic fields of the same frequency at the tip of the plasma torch. The plasma chamber maintains a continuous argon flow. A spark from a Tesla coil is used to ionize argon atoms and create electrons, both of which accelerate in the high frequency fields and collide with other argon atoms in an ionizing chain reaction, creating a high temperature plasma. The "tear" shaped plasma is formed by the continuous flow of argon in the chamber.

Samples tested using ICP-OES are aqueous (powders dissolved in acid in this work) and introduced into the apparatus first into a nebulizer which creates a fine mist. The mist is carried into the ICP which then evaporates the solvent. The sample then vapourizes into gaseous molecules, and finally atomizes (decomposes into individual atoms). This process generally happens in the first centimeter of the ICP, at temperatures of 7000 to 10000 K. The sample atoms are then ionized between 1-3 cm into the plasma at temperatures of 6000-7000 K and exciting electrons. Energized atoms emit photons at a specific energy given by

$$E_2 - E_1 = E_{photon} = \frac{hc}{\lambda} \, ,$$

(2.1)

where E_2 and E_1 are the excited and relaxed energy levels, respectively, E_{photon} is the energy of the emitted photon, h is Planck's constant, c is the speed of light and λ is the photon wavelength. Each element will therefore emit a unique spectra of wavelengths. The emitted light is separated into its spectrum and directed by an optical system including a prism, mirrors, and diffraction gratings onto an array of many (sometimes hundreds of

thousands) of silicon photodetectors. Some approaches, such as the one used in this study, apply monochromators to select very specific wavelength regions allowing for the use of less complex photodetectors (22528 in this study).[34] These photodetectors charge as photons of the desired wavelength hit the surface. The intensity of the photons at each detector corresponds to the concentration of the particular excitation, and therefore the element. The optics adjust for each element such that the array detects a narrow region around a characteristic wavelength with high accuracy.

2.3.2 Experimental Preparation

ICP-OES analysis uses high precision standards of known concentration in order to create a calibration curve to determine compositions of measured samples. Standards should "bracket" the concentration range of samples so that no sample lies outside the range of standards.

The apparatus used in this study was a Perkin Elmer Optima 8000 ICP-OES Spectrometer. The detection limit of lithium was 0.1 µg/L, or parts per billion (ppb). Limits for Ti and Fe were approximately 2-5 ppb. The detector was known to saturate at lithium concentrations of over 2 ppm. Due to the varying mass ratios of Fe and Ti to Li, careful consideration was taken to design a concentration window in which measurements were performed.

A 0 ppm "blank" was used, as well as two standards: one containing 0.5 ppm Li and 1 ppm Ti, Fe, Mn, Ni, Co, another containing 1 ppm Li and 2 ppm Ti, Fe, Ni, Mn, Co. Only Li, Fe and Ti were used in this study. Standards were prepared by accurately pipetting 1000 ppm single-element standards (Sigma-Aldrich) and diluting with 2% HNO_3. The 2%

HNO$_3$ used for sample preparation was prepared using deionized water (18.2 MΩ cm). In order to stay approximately in the 0.5 – 2 ppm bracketed region, ~10 mg of each sample was added to 2 mL aqua-regia and left overnight to dissolve fully. Approximately 10 µL (some samples contained air bubbles) was then pipetted and diluted with ~12 mL of 2% HNO$_3$. Samples containing air bubbles had an additional ~5 µL added. The target sample concentrations were designed such that measurement errors (such as those caused by air bubbles) were not likely to cause sample concentrations to lie outside of the measurement concentration window. Only one measurement (Fe in the 800°C x = 0.00 sample) was slightly outside the calibration window (2.282 ppm $vs.$ 2 ppm).

Measurements took place in the Department of Dentistry at Dalhousie. Measurements were taken in axial geometry, where the optical path was in line with the plasma axis. This geometry allowed for optimal resolution. If samples saturated the detector, radial geometry (perpendicular to the plasma) could have been used to decrease the signal, however the detector never appeared to saturate. All calibration curves were linear, with an R^2 value of 0.999411-1.00000. The R^2 value indicates the goodness of fit. Table 2.2 shows the composition per formula unit results from the 700°C and 800°C composition series as well as the 600-1000°C temperature series.

Figure 2.2 shows how the data in Table 2.2 compares to target compositions. All samples except for x = 0.30 compositions were within the apparatus' uncertainty of 2% of the target compositions.

The 700°C series (synthesized with 5% excess Li) was slightly more Li deficient than the 800°C (synthesized with 10% excess Li) series for all samples, though both series were slightly below target values for each composition. This may have be due to long heating

times. As temperature was increased, lithium loss also increased, as expected. The 600°C

sample was not included in Figure 2.2 because it was found to be multi-phase (see Chapter

3).

Table 2.2: ICP-OES results: Normalized composition per formula unit to a total of population of 2.000 (all compositions accurate within 2%)

700°C	Li	Ti	Fe
0.00	0.985	0.004	1.011
0.05	1.032	0.108	0.860
0.10	1.084	0.209	0.707
0.15	1.127	0.313	0.560
0.20	1.174	0.434	0.392
0.23	1.207	0.481	0.312
0.30	1.263	0.636	0.101
800°C	Li	Ti	Fe
0.00	0.998	0.004	0.998
0.05	1.042	0.107	0.851
0.10	1.097	0.207	0.696
0.15	1.132	0.313	0.555
0.20	1.187	0.414	0.399
0.23	1.209	0.485	0.306
0.30	1.280	0.621	0.099
Temperature	Li (target 1.15)	Ti	Fe
600°C	1.146	0.308	0.546
700°C	1.128	0.311	0.561
750°C	1.133	0.313	0.554
800°C	1.130	0.299	0.571
900°C	1.119	0.313	0.568
1000°C	1.121	0.318	0.561
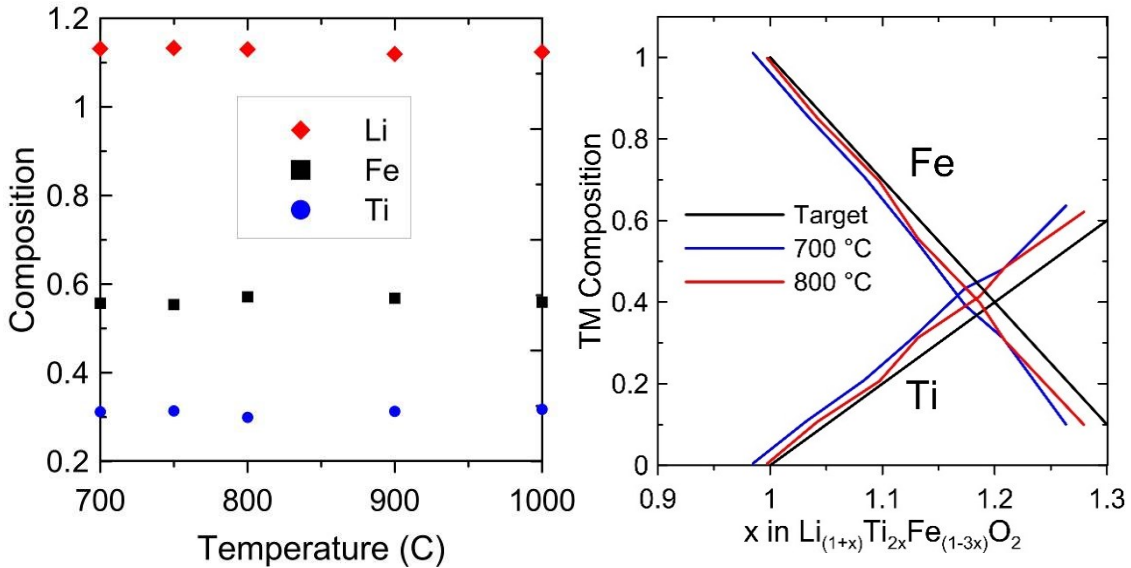
Figure 2.2: Elemental analysis results per formula unit for 700°C and 800°C series (left) plotted versus measured lithium content to demonstrate proximity to target compositions (black lines) and temperature series (right). All compositions except $x = 0.30$ were within the measurement uncertainty.

2.4 Scanning Electron Microscopy (SEM)

Scanning electron microscopy was used in this work to characterize the size and morphology of sample particles. SEM was used due to its ease of use, direct imaging capability and nanometer resolution making it optimal for analyzing small particles.

An SEM bombards a sample with an electron beam, typically created by a cold field emission or thermionic emission. In this work both techniques were used. Thermionic emission occurs when a heated filament (CeB_6 in this case) excites Ce outer shell electrons, creating free surface electrons.[35] Cold field electron emission uses a room temperature tungsten single crystal sharpened to a tip diameter of 10-100 nm.[36] A strong electric field caused by an extraction anode lowers the work function such that tunnelling occurs.[37] These electrons are accelerated away from the filament by a separate anode, and focused

into a beam. The electron beam is then raster scanned across the surface of a sample. Electrons undergo elastic and inelastic scattering upon interacting with sample surface atoms. This work used a back scattered electron (BSE) detector. BSEs are caused by elastic scattering off the sample. The intensity of a BSE signal corresponds to the mean atomic number (Z) of the area the beam interacts with, so higher Z corresponds to a brighter signal. A BSE detector is typically a Si wafer comprised of many sectors which communicate with software to turn the BSE signal into an image.

In this work, a Hitachi S-4700 SEM (cold field emission) was used at the Dalhousie Engineering campus, as well as an in-house Nano Science Instruments-Phenom Pro Desktop SEM (thermionic emission). The Hitachi was used due to its high resolution and fine-tunable controls for nano-sized particles. Powder samples were mounted on double-sided carbon tape, then on an aluminum SEM pin stub mount. Images were then taken at different magnifications for use in qualitative analysis.

2.5 X-Ray Diffraction (XRD)

X-rays are a powerful tool in electronic, local atomic, and bulk scale characterization, due to the wavelength range of x-rays being on the same order of magnitude as the atomic scale. An x-ray can interact with a substance by either scattering or absorbing.

X-rays that exhibit elastic scattering in a material can be used to obtain crystallographic information on the sample including lattice parameters, atomic structure and ordering, and phases present (inelastic scattering results in different diffracted wavelengths, causing interference and contributes to the background).[38] This technique is called X-Ray Diffraction.

2.5.1 X-Ray Diffraction in Crystallography

In crystallography, a structure is defined by a repeating unit cell with lattice parameters a, b, c which define the lengths of the cell, and angles α, β, γ, as shown in Figure 2.3a. A Bravais lattice is a structure which spans an infinite set of points by translational operations. Every position in a Bravais lattice is defined by a unique lattice vector

$$\boldsymbol{R} = n_1 \boldsymbol{a_1} + n_2 \boldsymbol{a_2} + n_3 \boldsymbol{a_3} \ ,$$

(2.2)

where n_1, n_2, n_3 are integer coefficients and $\boldsymbol{a_1}, \boldsymbol{a_2}, \boldsymbol{a_3}$ are primitive vectors. The reciprocal lattice is described by reciprocal vectors

$$\boldsymbol{G} = h\boldsymbol{b_1} + k\boldsymbol{b_2} + l\boldsymbol{b_3} \ ,$$

(2.3)

where h, k, l are integer coefficients, also known as Miller indices, and $\boldsymbol{b_1}, \boldsymbol{b_2}, \boldsymbol{b_3}$ are reciprocal primitive vectors that are orthogonal to two lattice vectors, *ie*.

$$\boldsymbol{b_1} = 2\pi \frac{\boldsymbol{a_2} \times \boldsymbol{a_3}}{\boldsymbol{a_1} \cdot (\boldsymbol{a_2} \times \boldsymbol{a_3})} \ , \quad \boldsymbol{b_2} = 2\pi \frac{\boldsymbol{a_3} \times \boldsymbol{a_1}}{\boldsymbol{a_2} \cdot (\boldsymbol{a_3} \times \boldsymbol{a_1})} \ , \quad \boldsymbol{b_3} = 2\pi \frac{\boldsymbol{a_1} \times \boldsymbol{a_2}}{\boldsymbol{a_3} \cdot (\boldsymbol{a_1} \times \boldsymbol{a_2})} \ ,$$

(2.4)

yielding the condition

$$\boldsymbol{a_i} \cdot \boldsymbol{b_j} = 2\pi \delta_{ij} \ ,$$

$$\boldsymbol{R} \cdot \boldsymbol{G} = 2\pi n \ .$$

(2.5)

Miller indices h, k, l describe crystallographic planes based on where they intersect the crystal axes. Identical h, k, l planes have spacings d_{hkl} determined by h, k, l as well as the

lattice parameters a, b, c, α, β, and γ. A plane which intercepts the points $u\hat{a}_1, v\hat{a}_2, w\hat{a}_3$, where u, v, w are fractional atomic coordinates is denoted $(h\ k\ l) = (u^{-1}\ v^{-1}\ w^{-1})$ and repeats every spacing d_{hkl}. A plane that never crosses an axis is said to have an intercept at infinity. For example, in an R$\bar{3}$m structure, the plane parallel to the a and b axis and intercepts the c-axis with a d spacing of $c/3$ is the (003) plane.
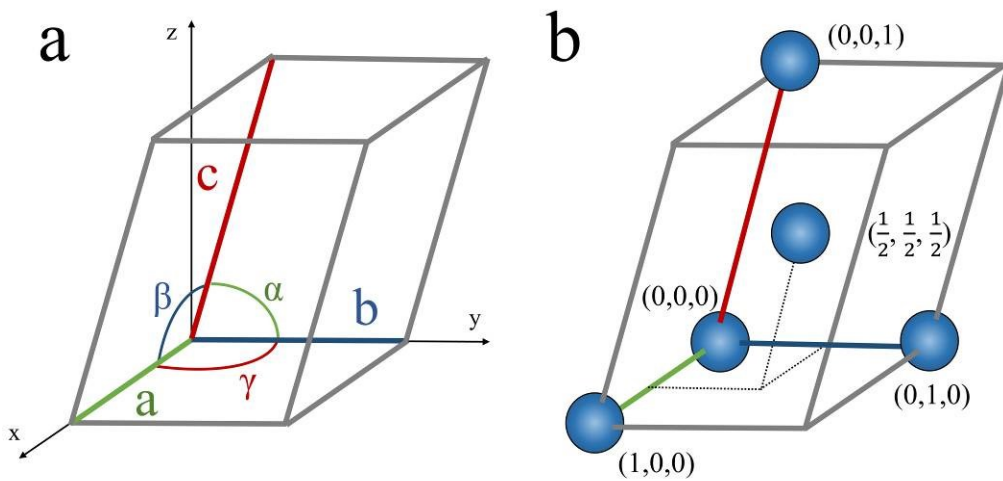
Figure 2.3: a) Lattice parameters a, b, c and α, β, γ define the unit cell lengths and angles respectively. The unit cell repeats throughout the structure. b) Atomic positions described by fractional atomic coordinates.

When an x-ray penetrates a material, they can elastically scatter off atoms at the angle of incidence off identical $(h\ k\ l)$ planes with plane spacing d_{hkl}. In order for measured diffraction to occur, these two x-rays must interfere constructively. Bragg's law defines the criteria required for this constructive interference. When two x-rays scatter off atoms in a material, one may travel further than the other, resulting in a path length difference L, shown in Figure 2.4. By inspection of Figure 2.4, in order for constructive interference to

occur, $L = \lambda n$, where n is an integer and λ is the wavelength of the incoming x-rays. Therefore, writing L in terms of d_{hkl} and θ, the Bragg equation is obtained

$$n\lambda = 2\, d_{hkl} \sin\theta \; ,$$

(2.6)

The scattering vector, $\boldsymbol{q}$, is the difference between the diffracted ($\boldsymbol{k_f}$) and incident ($\boldsymbol{k_i}$) beams. The path difference L introduces a phase shift φ between the diffracted x-rays. The superposition of the two waves scattering off two atoms as shown in Figure 2.4 can be written

$$\Psi(\boldsymbol{r}, t) = \psi(\boldsymbol{r}, t)(1 + e^{i\,\varphi}) \; ,$$

(2.7)

where $\Psi(\boldsymbol{r}, t)$ is the resulting superposition of the two waves, and $\psi(\boldsymbol{r}, t)$ are the x-rays' wave functions. With respect to Figure 2.4, the phase shift can be written

$$\varphi = \boldsymbol{k_f} \cdot \boldsymbol{s} - \boldsymbol{k_i} \cdot \boldsymbol{s} = \boldsymbol{q} \cdot \boldsymbol{s} \; ,$$

(2.8)

where $\boldsymbol{s}$ may also be written as the difference between the two atoms' Bravais lattice vectors, which is itself a Bravais vector, $\boldsymbol{R_s}$. Equation 2.7 shows that in order for constructive interference to occur, the following condition must apply:

$$\boldsymbol{q} \cdot \boldsymbol{s} = \boldsymbol{q} \cdot \boldsymbol{R_s} = 2\pi n \; .$$

(2.9)

The condition in Equation 2.5 shows in order for Equation 2.9 to be true, $\boldsymbol{q} = \boldsymbol{G}$, which means $\boldsymbol{q}$ must be perpendicular to an $(h\,k\,l)$ plane in order for diffraction to occur. Therefore in order for every $(h\,k\,l)$ plane to be detected in an XRD experiment, a sample needs to be exposed to the incident beam at every orientation over a broad range of angles.
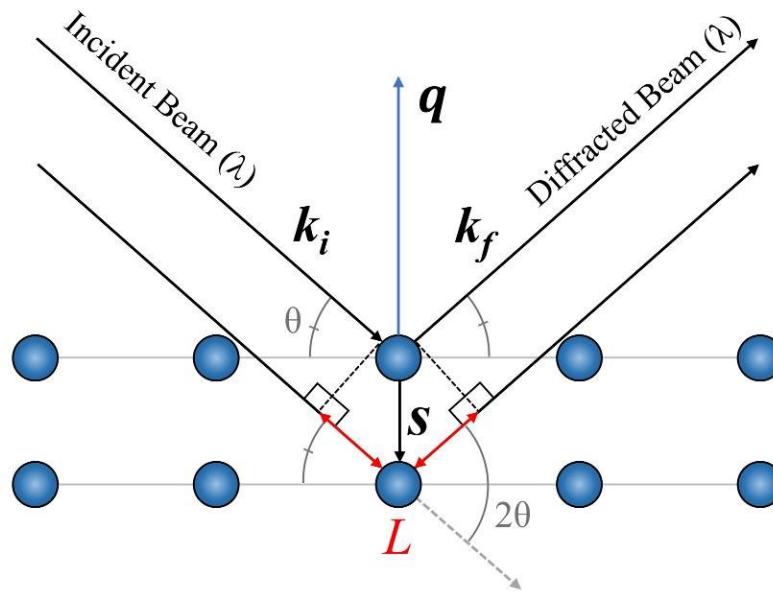
Figure 2.4: Diagram of the Bragg condition: Two incident x-ray beams scattering off identical $(h\,k\,l)$ planes at an angle of 2θ from the incident beam. The two diffracted beams are in phase if the conditions in (2.4) are met. The scattering vector, q must also be perpendicular to the $(h\,k\,l)$ planes in order for coherent scattering to occur.

XRD patterns contain peaks which occur at angles that correspond to each $(h\,k\,l)$ plane, and may be used to extract lattice parameters and information about atomic structure and ordering. The following sections discuss XRD methods used in this work as well as the fitting of XRD patterns.

2.5.2 X-Ray Diffractometers

In this work, two XRD techniques were used. The majority of samples were analyzed using a Seimens D-5000 Bragg-Brentano Diffractometer. Select samples were also measured at the Canadian Macromolecular Crystallography Facility at the Canadian Light Source Sychrotron in Saskatoon, SK. The D-5000 was used due to its ease of use and access, while CMCF was used due to its high flux, precision and very high signal to noise

ratio. Figure 2.5 demonstrates the difference in signal to noise in a sample of $LiFeO_2$. Both

methods rely on different x-ray generation and experimental geometries.
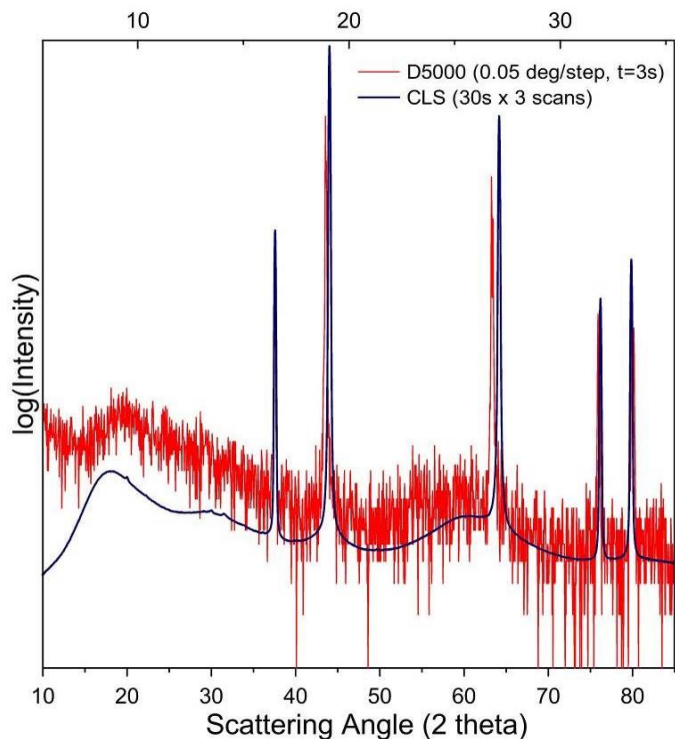
Figure 2.5: An example of XRD data collected on an in-house D-5000 diffractometer (red line, lower *x* axis) and at CMCF (blue, upper *x* axis) demonstrating the difference in signal to noise. For the purpose of comparison, the intensities were scaled logarithmically to the same order of magnitude. Note peaks were not expected to align due to the difference in wavelength of the x-rays in the experiments (1.542 Å *vs.* 0.6889 Å).

The D-5000 produces x-rays using a copper x-ray tube. A heated cathode expels

electrons by thermionic emission, bombarding a Cu target anode at a current of 30 mA and

40 kV bias, exciting core 1s electrons. Allowed electron energy level transitions from 2p

to 1s and 3p to 1s fill the electron holes, emitting Cu-Kα (λ = 1.5418 Å) and Cu-Kβ (λ =

1.3922 Å) radiation, respectively.[39] The x-rays then leave the tube through a window and

travel through divergent slits which control the width (divergence) of the beam at the

sample. The x-rays then interact with the sample. Elastically scattered x-rays then pass

through an anti-scatter slit, receiving slit, and a monochromator to remove Cu-Kβ and fluorescence x-rays before reaching a scintillator detector. This geometry is shown in Figure 2.6.
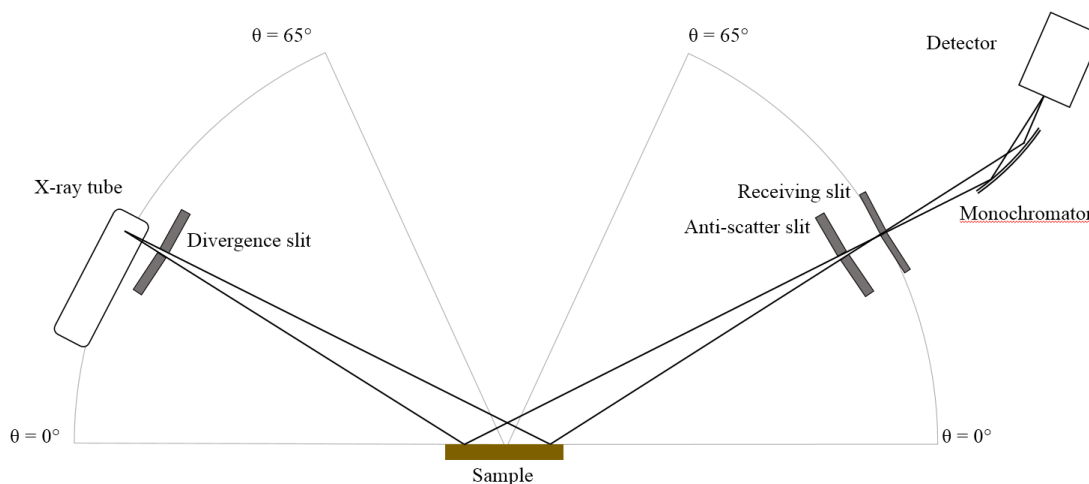
Figure 2.6: A schematic of the D-5000 Bragg-Brentano goniometer and basic optical path. The D-5000 has a range of $0° \leq 2\theta \leq 130°$.

Samples measured on the D-5000 were packed level into a well in a stainless steel sample holder and mounted into the sample stage. Patterns were collected between scattering angles 10 - 85° for 3 seconds with a 0.05° step size.

A synchrotron generates x-rays in a very different way from an x-ray tube. A linear accelerator (linac) accelerates electrons to 250 MeV and injects them into a "booster ring" which accelerates the beam up to 2.9 GeV.[40] The beam is then introduced to the storage ring, which consists of multiple straight sections, separated by two bending magnets and periodic magnetic fields, or "insertion devices". When electrons pass through a large magnetic field in a bending magnet or insertion device, a force is applied, changing the trajectory of the electron and emitting synchrotron radiation, which covers an energy range from infrared to hard x-rays (6 meV to 100 keV).[40] This radiation is fine tuned in advanced

optical systems to select precise wavelengths and can be used for a variety of applications, such as XRD and XAS in this work.

The experimental setup used at CMCF involved a rotating sample stage in which a 0.5 mm diameter polyimide capillary containing a powder sample was mounted. The sample stage was aligned with the beam and a detector (4096x4096 Rayonix MX300 CCD x-ray detector) with 9 charge-coupled device sections in a 3x3 grid. The detector was set at a distance of 150 mm in line with the sample, and a beam energy of 18 keV was selected (λ = 0.6889 Å), yielding a scan range of approximately 5 - 45°. Data collection was approximately 30 seconds per scan, and 3-5 scans were taken and summed per sample, at 180° of capillary rotation per scan. This geometry used is called Debye-Scherrer, which makes use of 3-dimensional scattering of x-rays in Debye-Sherrer cones.[38] A simplified example is shown in Figure 2.7, and the experimental setup is shown in Figure 2.8.

In order to calibrate collected data, a sample pattern of LaB_6 was collected and used as a calibration standard in the software GSASII.[41] An empty kapton capillary was also measured and used for background subtraction. 2-Dimensional images obtained from the detector were integrated using the GSASII software in order to obtain patterns to use in fitting and analysis.
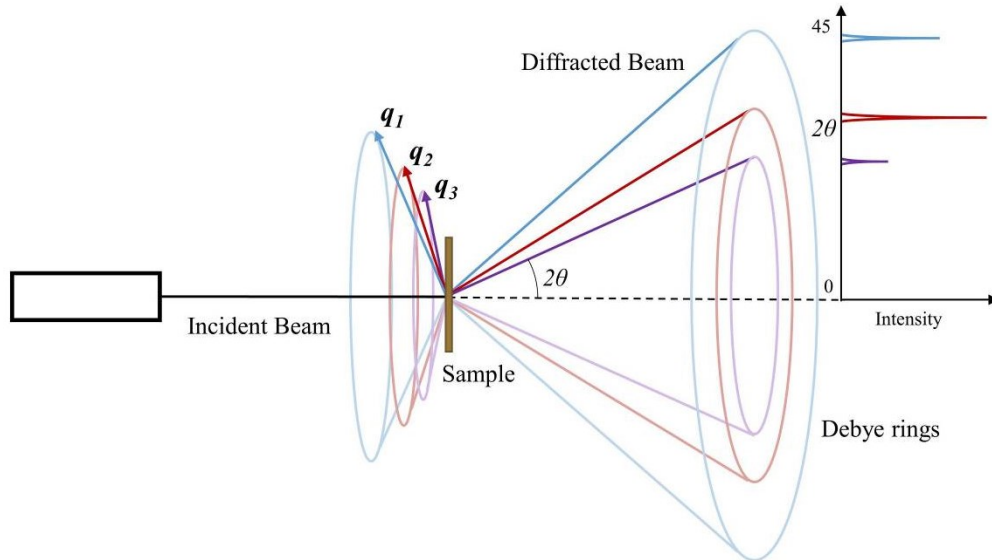
Figure 2.7: Debye-Scherrer geometry for powder XRD. X-rays scatter at an angle 2θ from the incidence beam. The detector creates a 2-dimensional image based on the intensity of incoming x-rays. The signal is integrated and transformed into a standard XRD pattern. Three peaks on the right are due to scattering from ($h\ k\ l$) planes with scattering vector "cones" q_1, q_2, q_3 have Debye rings and corresponding peaks in the diffraction pattern.
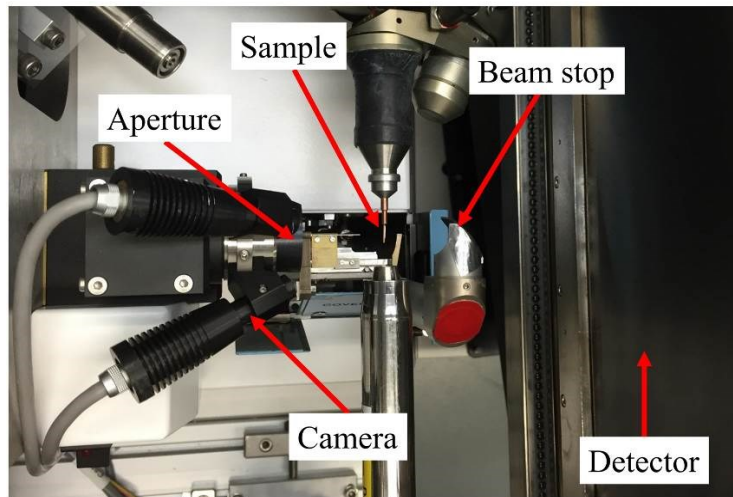
Figure 2.8: The experimental configuration at CMCF. The beam comes from the labelled aperture on the left, interacts with the sample and the diffracted x-rays reach the detector on the right. The beam stop protects the detector from prolonged exposure to the high intensity of the transmitted beam. A camera allows for user observation when the beamline is in operation.

2.5.3 Calculation of X-Ray Diffraction Data

XRD patterns, if treated correctly, may lead to a very clear understanding of a sample. Information of impurities, multiple phases, and many structural parameters may be interpreted through calculations and proper fitting techniques. A common method of XRD pattern calculation is the Rietveld method, which is implemented in this work.[42] In order to calculate diffraction data, the space group (which describes translational symmetry information), lattice parameters $(a, b, c, \alpha, \beta, \gamma)$, atom positions and the x-ray wavelength must be known. Other parameters, such as preferred particle orientation and grain size, stress/strain, atomic thermal effects, *etc.* may be used in calculations and refinement in order to better fit experimental data.

The intensity of which an x-ray is scattered off an atom depends on the atom position in the lattice, its $(h\ k\ l)$ plane, and which element it scatters off. The intensity of a specific peak is dependent on many factors, and is given by

$$I(2\theta) = I_o P(2\theta) L(2\theta) F^2(h, k, l) M(h, k, l) DW(h, k, l) \ ,$$

(2.10)

where I_o is the incident beam intensity, $P(2\theta)$ is the polarization factor, $L(2\theta)$ is the Lorentz correction, $F(h, k, l)$ is the geometric structure factor, $M(h, k, l)$ is the multiplicity of the $(h\ k\ l)$ plane, and $DW(h, k, l)$ is the Debye-Waller factor.[43]

The polarization factor describes the polarization of the x-rays at each angle, and is given by

$$P(2\theta) = \frac{1 + \cos^2 2\theta \cos^2 2\theta_m}{2} \ ,$$

(2.11)

where θ_m is the monochromator angle, assuming the slits, sample, and monochromator occupy the same plane (as shown in Figure 2.6). The Lorentz correction considers the effect of the 3-dimensional Debye-Sherrer cones (Figure 2.7) and the detector's ability to capture a fraction of the signal at lower and higher angles. This correction is proportional to $\sin^{-1} 2\theta$.

The geometric structure factor, F, of a structure is a summation of the individual scattering signals of each atom in a particular $(h\,k\,l)$ plane, given by

$$F = \sum_m f_m e^{iq \cdot r_m} \, ,$$

(2.12)

where r_m is each atom's position in the unit cell, and f_m is the atomic scattering factor of atom m, which can be found for each element in reference databases for use in data analysis.[38,39,44] Equation (2.11) can be reduced in terms of $n_1, n_2, n_3, h, k,$ and l for m atoms in identical $(h\,k\,l)$ planes

$$F(hkl) = \sum_m f_m e^{2\pi i\,(hn_{1m} + kn_{2m} + ln_{3m})} \, ,$$

(2.12)

where n_{1m}, n_{2m}, n_{3m} are now fractional atomic coordinates of atom m. The multiplicity factor is an integer representing the multiplicity of a specific $(h\,k\,l)$ set of planes that result in a specific peak. The Debye-Waller factor describes the thermal vibrational effects of atoms which attenuates scattering. This is given by

$$DW(h, k, l) = e^{-2B \left| \frac{\sin \theta}{\lambda} \right|^2} \, ,$$

(2.13)

where $B = 8\pi^2 u^2$ and u is the root mean square displacement of an atom perpendicular to the $(h\ k\ l)$ plane.[45] Typical Debye-Waller values may be found in literature.[46]

2.5.4 Fitting of X-Ray Diffraction Patterns

In this work, refinement was done using the software Rietica, and followed a systematic procedure.[47] Initially each pattern was fitted using the R$\bar{3}$m space group with Li and TM atoms distributed equally between sites to simulate a disordered rocksalt Fm$\bar{3}$m configuration. Initial lattice parameters and atomic positions were found using examples from the Crystallography Open Database and Reference 46 respectively and were set to populate layers according to ICP-OES results in section 2.3.[48,49] The correct wavelength (Cu-Kα for D-5000 or 0.688 Å for CMCF experiments) was used. Lattice parameters and intensity were refined before other parameters. Cation and lithium mixing was then allowed. Fe and Ti were constrained to mix between layers proportional to populations determined by ICP-OES results. Next, sample displacement, peak shape, and the oxygen site position were refined. Samples in which no R$\bar{3}$m (003) peak was visible were also fitted using the Fm$\bar{3}$m space group, assuming 100% disorder, so no mixing was allowed and Li, Ti, Fe occupied the same site according to ICP results. In all cases samples without a (003) peak converged using less refinement steps and in most cases yielded a lower Bragg R-factor using the Fm$\bar{3}$m space group. The Fm$\bar{3}$m fitted results were used in the reported fitting parameters.

The amount of cation disorder was determined by the amount of TM population in the lithium layer compared to that of the TM layer. The lithium layer was labelled as the layer with the higher lithium population after mixing. Another method of comparing the amount

of disorder may be found using the lattice parameters. A perfectly cubic close-packed (ccp) structure can also be defined by a $R\bar{3}m$ space group with a hexagonal unit cell, in which the c-lattice and a-lattice parameters follow the constraint

$$\frac{c}{3a} = 1.6333$$

(2.14)

The structure of materials like $Li_{(1+x)}Ti_{2x}Fe_{(1-3x)}O_2$ can be described using different unit cells such as cubic, monoclinic, hexagonal or rhombohedral, shown in Figure 2.9. The amount of deviation of c/*3a* from 1.6333 can therefore be used as a qualitative measure of the amount of disorder.[50]
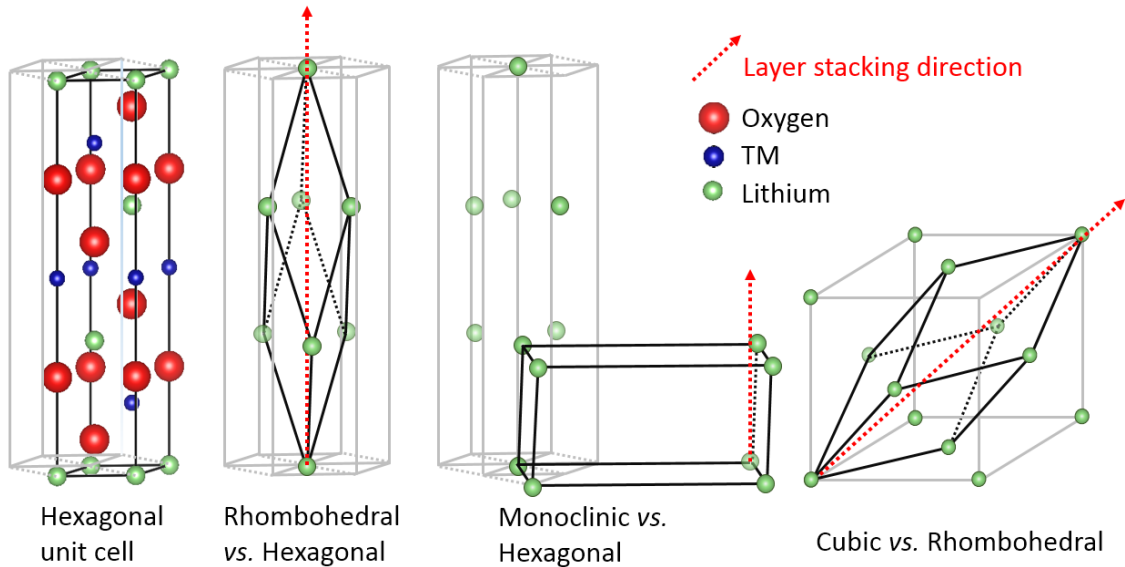
Figure 2.9: Comparisons of hexagonal, rhombohedral, monoclinic and cubic unit cell descriptions using the same set of atoms.

Another qualitative method of identifying ordering in samples is the presence of a hexagonal (003) peak. The structure of materials like $LiCoO_2$ is normally described in the hexagonal setting of the $R\bar{3}m$ space group. Certain peaks characteristic of an $R\bar{3}m$ space

group (*vs.* Fm3m) can be used to identify if ordering is taking place. The most prominent of these is the (003) peak. Considering the structure factor in Equation 2.12, Figure 2.10b illustrates the (110) projection of a hexagonal setting R$\overline{3}$m space group (Figure 2.10a demonstrates a (110) projection in the unit cell). Considering the TM atoms (blue) and Li atoms (green) in the (003) planes for an ordered structure (Figure 2.10b, left), the structure factor can be calculated using the c-axis coordinates:

$$F_{TM}(003) = \sum_m f_{TM} e^{2\pi i \,(0+0+3n_{3m})} = f_{TM}\left((-1)^{6(0)} + (-1)^{6\left(\frac{1}{3}\right)} + (-1)^{6\left(\frac{2}{3}\right)}\right) = 3f_{TM} \,,$$

$$F_{Li}(003) = \sum_m f_{Li} e^{2\pi i \,(0+0+3n_{3m})} = f_{Li}\left((-1)^{6(1/6)} + (-1)^{6(1/2)} + (-1)^{6(5/6)}\right) = -3f_{Li} \,.$$

$$(2.14)$$

When the structure fully disorders (Figure 2.10b, right), half of the TM atoms are in the original (003) planes (solid lines) and half in the Li (003) planes (dotted lines). The structure factors for the (003) peaks are then

$$F_{TM}(003) = f_{TM}\left(\left((-1)^{6\left(\frac{1}{6}\right)} + (-1)^{6\left(\frac{1}{2}\right)}\right) + \left((-1)^{6\left(\frac{2}{3}\right)} + (-1)^{6\left(\frac{1}{6}\right)}\right)\right) = f_{Li}(-2+2) = 0 \,,$$

$$F_{Li}(003) = f_{Li}\left(\left((-1)^{6(0)} + (-1)^{6\left(\frac{1}{3}\right)}\right) + \left((-1)^{6\left(\frac{1}{2}\right)} + (-1)^{6\left(\frac{5}{6}\right)}\right)\right) = f_{Li}(2-2) = 0 \,.$$

$$(2.15)$$

Therefore as the structure disorders, the mixing between the two d_{003} spacings causes structure factors to decrease, meaning the peak intensity scales inversely with the degree of disorder. To illustrate this relationship's effect on a diffraction pattern, calculations of LiFeO$_2$ were made in an R$\overline{3}$m space group using 0, 20, 40, 60, 80 and 100% cation disordering and are shown in Figure 2.11. When preferential ordering of lithium in the transition metal layer occurs such as in the C2/m space group, the relative magnitude of

the (003) peak will be slightly smaller than that of an R$\bar{3}$m space group due to the cancellations between d_{003} spacings shown above. Thus the only quantitative way to characterize disorder is to refine the TM population in each layer and the ratio defines the degree of disorder. This is also why disorder and cation mixing have been used interchangeably in the literature.
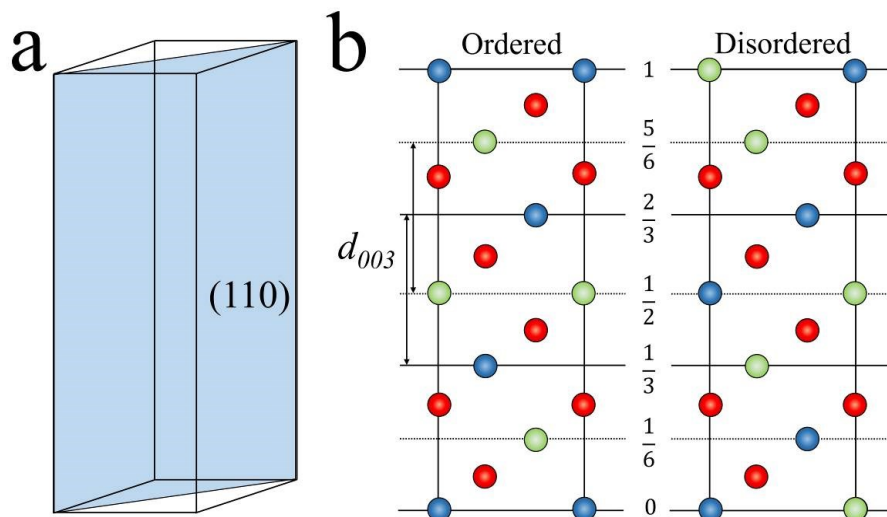
Figure 2.10: A (110) projection (a) of an ordered (left b) and disordered (right b) R$\bar{3}$m space group. Fractional c-axis coordinates are used in the structure factor calculation for the (003) planes (horizontal lines) with spacing d_{003}. TM atoms are blue, Li green, and oxygen red.
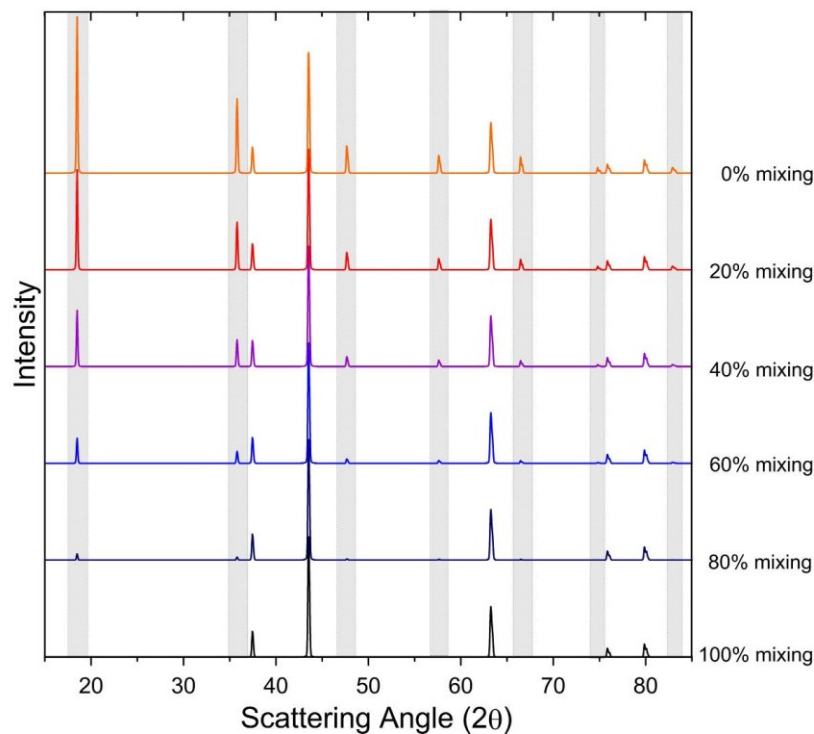
Figure 2.11: Example powder XRD calculations of $LiFeO_2$ with different degrees of disorder illustrating the dependence of peak height on disorder for planes with a c-axis component (highlighted peaks).

2. 6 X-Ray Absorption Spectroscopy (XAS)

X-rays may also be absorbed by core level electrons in atoms. The spectra obtained by varying energy around these defined energy levels yields information on electronic structure, atomic coordination, and local atomic structure. In this work, X-ray absorption near edge structure (XANES) and extended X-ray absorption fine structure (EXAFS) were used in order to qualitatively characterize valence states of TMs and oxygen, as well as to discuss structural and electrochemical mechanisms occurring during charging of the $x = 0.19$ material ($Li_{0.19}Ti_{0.41}Fe_{0.40}O_2$).

When tuned to energies close to a core electron binding energy, X-ray radiation can be absorbed by the electron. Each element has a unique energy, E_0 which defines the elemental absorption edge position. The relative position and shape of the absorption "edge" around E_0 can be compared to theoretical calculations, standard reference spectra or other published works. The intensity of transmitted X-rays through a material is given by the Beer-Lambert law

$$I_T = I_0 e^{-\mu(E)t} \; ,$$

(2.16)

where I_0 is the incident intensity of the X-ray beam, t is the thickness of the sample, and $\mu(E)$ is the absorption coefficient.[51] In a XAS experiment, $\mu(E)$ is found by measuring I_0 and I_T before and after the sample, respectively over a broad range of energies, typically - 100 eV below E_0 of the element to $300 - 400$ eV above. Assuming a uniform thickness, the absorption coefficient can be normalized and used for electronic and structural modelling.

The XANES region, from ~10 eV below E_0 to ~30 eV above contains information on the valence state of the element (higher valence corresponds to a higher edge energy) and can give insight to site structure, bond lengths and strengths around the atom, *etc.* Every element has multiple absorption edges due to different binding energies of core electrons, and each absorption edge contains characteristic features from specific core electron excitation levels which can be used to characterize local environments. An example Fe K-edge spectra is shown in Figure 2.11 with the XANES region labelled and expanded.

The EXAFS region, 30 eV above E_0 occurs due to excited core electrons excited significantly above their binding energy becoming quasi-free photo-electrons in the

sample. The difference in energy from the binding energy becomes kinetic energy and the photo-electron scatters off neighbouring atoms. The constructive and destructive interference of these photo-electrons is dependent on local atomic structure: the frequency depends on proximity to other atoms and the intensity depends on the number and type of atom scattering occurs off of. The EXAFS equation is described by the sum of all scattering paths in the sample and is written $\chi(k)$, the difference between the signal and the background absorption, given by

$$\chi(k) = \sum_i \left(\frac{N_i {S_0}^2 F_i(k)}{k {R_i}^2}\right) \sin\big(2kR_i + \varphi_i(k)\big)\big(e^{-2{\sigma_i}^2 k^2}\big)\left(e^{\frac{-2R_i}{\lambda(k)}}\right) \, ,$$

$$R_i = R_0 + \Delta R \, ,$$

and

$$k = \sqrt{\frac{2m_e(E - E_0)}{\hbar}} \, ,$$

(2.17)

where N_i is the degeneracy of the scattering path, S_0 is the passive electron reduction factor (scattering atom specific), $F_i(k)$ is the effective scattering amplitude, R_0 is the scattering path length, ΔR is the change in half-path length, $\varphi_i(k)$ is the phase shift, σ_i is the mean squared displacement (from structural or thermal disorder), $\lambda(k)$ is the mean free path and m_e is the electron mass.[52] $N_i, F_i, \varphi_i, \lambda,$ and R_0 can be calculated from the crystal model, and $S_0, E_0, \Delta R$ and σ_i can be refined in calculated models. The phase shift typically creates difficulty in fitting and characterizing path length, as it has significant magnitude, often creating a shift in R on the order of 0.5 Å.

Data processing was done using the Athena software package.[53] Using the software, the obtained spectrum was normalized to the experimental background before and after the edge feature. The K-edge was determined by comparison to a metal standard. The standard K-edge was determined by the local maxima of $\frac{d\mu}{dE}$ around the K-edge feature and an energy shift to the theoretical edge position was applied. The powder sample spectra were shifted by the same energy and the K-edge found using the same $\frac{d\mu}{dE}$ method. Oscillations in the EXAFS region were be translated into "k-space" by selecting a range of k values which a "Hanning" amplification window (square cosine function) was applied to, typically $k = 1$ to $k = 8$, using the expression for k in equation 2.17.[54] Once in k-space, a k-weighting of 2 was used and the software performed a Fourier transform on the weighted k-space spectra (shown in Figure 2.12) with respect to R_i, yielding details about local atomic structure (typically two to four atomic "shells" away from the target element sites can be probed).[54] The EXAFS region and R-space transform of an Fe-K edge are shown in Figure 2.11.
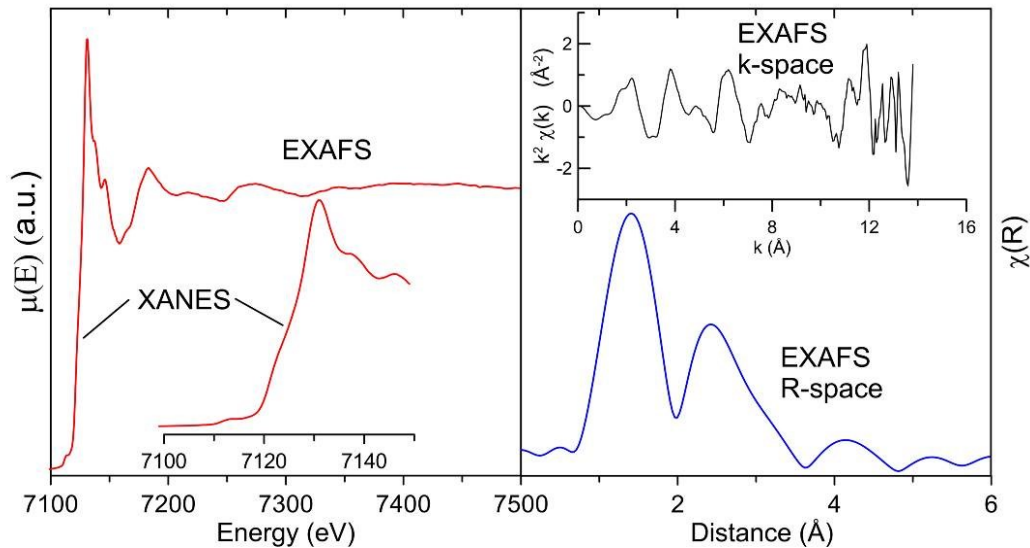
Figure 2.12: Fe K-edge XAS with XANES and EXAFS regions (left), weighted *k*-space (upper right) and a Fourier transform of normalized EXAFS data representing the local atomic structure around Fe sites (right).

Due to the complexity of XAS calculations, a large portion of literature using XANES uses qualitative approaches, comparing obtained data to well-known standards, similar structures and comparing trends to theoretical predictions. Modelling of XANES and EXAFS using calculations and refinement was not completed in this work, however significant trends and conclusions were made from comparisons of literature and theory to the experimental data.

Pristine powder Fe and Ti K-edges were measured at the Canadian Light Source at the SXRMB beam line. $x = 0.00$, $x = 0.09$, $x = 0.19$ and $x = 0.28$ 800°C samples were pressed onto carbon tape and mounted in a vacuum chamber. Fluorescence yield (FY) detection was used, in which a detector measures the number of fluorescence X-rays from electrons dropping to fill core holes caused by absorption excitations.[51]

Ex-situ O K-edge and Fe and Ti L-edge studies were also done at the REIXS beamline. The 800°C $x = 0.19$ material was used in the construction of coin cells similar to the process described in Section 2.7.2. These cells were charged for 10, 20, 30, 40, 50 and 60 hours. Cells were then disassembled in an argon glovebox and electrodes were rinsed in DEC and left to dry. Electrodes were then transferred onto carbon tape and transferred to the vacuum chamber on the beamline with minimal air exposure. Measurements, coin cell disassembly and sample mounting were performed by CLS staff scientists. Two cells were noticeably shorted during disassembly and were not able to be measured. Measurements were then taken in FY and total electron yield (TEY) mode, where the current flow to ground required to neutralize the sample due to all ejected photoelectrons (predominantly Auger electrons) was measured.[55] FY and TEY spectra data were then used to characterize electrochemical processes during charge in the bulk and at the surface, respectively.

2.7 Electrochemical Testing

2.7.1 Electrode preparation

Electrochemical testing of positive electrode materials in this work was performed on 2325-type coin cells, which have a 23 mm diameter and 2.5 mm height. The $Li_{(1+x)}Ti_{2x}Fe_{(1-3x)}O_2$ active electrode materials were fabricated as described in section 2.1. Marks *et al.* outlined electrode fabrication parameters that optimize laboratory scale electrode preparation, and were used as a guideline, however some parameters were refined, such as the carbon and binder to active material ratios based on electrode performance.[56] It was found that ratios of (active material):(carbon black):(binder) of 80:10:10 and 85:10:5 provided acceptable performance after repeated experiments, which was consistent with

other studies done on similar materials.[25] Though a higher ratio of carbon and binder to active material has been shown to lower coulombic efficiency (CE), this work was of primarily academic interest and focussed on maximizing first charge capacity in order to characterize the capacity in disordered materials, and not long term performance.[56]

Each material was hand ground with a mortar and pestle until the powder reached a smooth, even consistency. A measured amount of $Li_{(1+x)}Ti_{2x}Fe_{(1-3x)}O_2$ active material was used for each sample. Super-S carbon black (Timcal) and polyvinylidene fluoride (PVDF) (Kynar 301F-Elf-Atochem) as a binder were added to the active material in predetermined mass ratios. The temperature series was mixed using an 80:10:10 ratio. After trials of various ratios the 700°C and 800°C series were mixed with a ratio of 85:10:5. The total mass of each mixture was 2 g. ~1.8 g of 1-methyl-2-pyrrolidone (NMP) (Sigma-Aldrich, 99.5% anhydrous) was then added to each sample in a polycarbonate container with two alumina milling beads. The "slurry" was then mixed in a dual-motion planetary mixer (KK-250 S Mazerustar, Kurabo) for 300 s. If the desired consistency was not achieved, excess NMP was added and the sample was mixed for an additional 100 s. Due to the gradual difference in morphology and surface area, the amount of NMP varied significantly between samples.

The slurries were then each distributed on two approximately 5 cm wide by 15 cm long strips of 21 μm aluminum foil near the top of the strip. A 0.006 in (152 μm) notch bar was then used to spread the slurry evenly down the aluminum strip. The slurries were immediately transferred to an oven to evaporate NMP at 120°C overnight. A rolling press was then used to smooth and compress the electrodes at approximately 1000 atm.

2.7.2 Coin cell Fabrication

Electrodes prepared by methods outlined above were punched into 1.27 cm^2 discs and weighed using a microbalance. Accounting for the mass of aluminum foil and the ratio of additives in the slurries, the active material masses were typically 15-20 mg per disc. Using both the 0-TM accessible lithium predicted by Lee *et al.* and the theoretical redox capacity of each composition, the theoretical capacity for each electrode was calculated. The predicted masses and capacities (in mA/g) were then used to determine the current at which the cells would be cycle in order to ensure approximately consistent gravimetric specific currents were used.

2325-type coin cells were then assembled using the prepared electrodes in an argon filled glovebox (Innovative Technologies). Figure 2.11 demonstrates the cell components and order of cell construction. The positive electrode disc was placed in the stainless steel "can" and wetted with 2-3 ~20 µL drops of an electrolyte mixture of 1 M LiPF$_6$ (BASF, 99.9%) in 1:2 EC:DEC (BASF, 99.99%, < 20 ppm water). A polypropylene blown microfiber (BMF) separator (3M) was placed on the electrode and wetted with approximately 10 drops of electrolyte. A Celgard 2320 thin film polypropylene separator (Celgard LLC) was placed on the BMF followed by one drop of electrolyte. A 1.29 cm^2, 150 µm thick lithium metal foil (Chemetall, >99.99%) was used as the negative electrode. A stainless steel spacer and spring were then carefully centered as not to make contact with the can and short the cell. The cell was then pneumatically pressed and the can edges crimped into a polypropylene gasket placed around the cap, creating an airtight seal without causing a short. Thin stainless steel tabs were then cut and spot welded on both terminals for electrical connections used in charge discharge cycling.
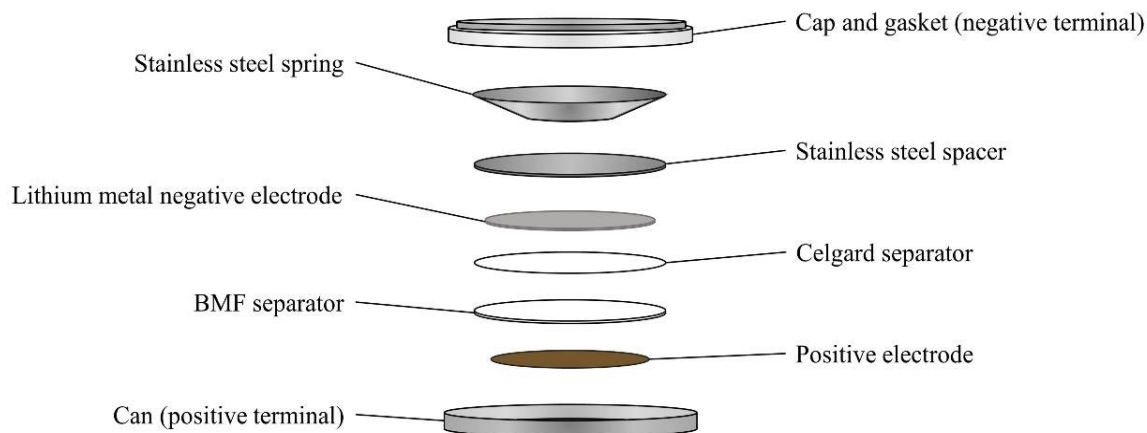
Figure 2.13: Components of a 2325-type coin cell used in electrochemical testing

2.7.3 Electrochemical Measurements

Electrochemical measurements were used to test multiple performance factors and characterize reactions at different SOCs. Cells were charge/discharge cycled using an in-house charging system (E-One Moli Energy Limited Canada) in temperature controlled boxes, typically at $40 \pm 0.1°C$, unless otherwise stated. Cells were cycled at a constant current equal to the full theoretical capacity of the cell over *n* hours, denoted as C/*n*, between an upper and lower potential limit. This type of cycling is known as galvanostatic charge-discharge cycling. Most cells were cycled between 2.2 - 4.5 V at a rate of C/60, unless otherwise stated.

Voltage (V) was recorded by the charging system at regular intervals. This data was used to determine the capacity (q) by multiplying the charge and discharge times by the current used and compare with the predicted model. Data was also used to analyze performance over many charges and characterize electrochemical processes at different voltages and SOCs. Voltage curves (V *vs*. q) and differential capacity plots (dV/dq *vs*. q)

gave insight to electrochemical reactions and as performance indicators, depending on the

reversibility and long term stability of certain reactions.

Chapter 3: Structural Analysis

For the purpose of consistency, this work will refer to peaks and lattice parameters by the equivalent in the R$\bar{3}$m space group. Calculated lattice parameters fitted using the cubic Fm$\bar{3}$m space group were converted so they could be compared with ordered samples.

3.1 Temperature Effect on Disorder

During synthesis trials it was observed that samples heated at lower temperatures yielded various degrees of ordering, with the appearance of a (003) peak at approximately $2\theta = 18°$ as well as other smaller R$\bar{3}$m peaks. Figure 3.2 shows the XRD patterns for the full temperature series. The target composition of Li$_{1.15}$Ti$_{0.30}$Fe$_{0.55}$O$_2$ was synthesized as outlined in Section 2.2 and obtained compositions were determined by ICP-OES in Section 2.3. Lithium loss during heating was observed to increase with temperature, yielding values of $x = 0.15$ at 600°C, $x = 0.13$ at 700°C, 750°C, and 800°C and $x = 0.12$ at 900°C and 1000°C.

The 600°C sample was clearly multi-phase, while all other samples appeared to be single phase. Figure 3.1 identifies multiple phases found in the 600°C sample. Phase identification was performed using the program Match! and the PDF-2 database.[57,58] Due to peak overlap of the R$\bar{3}$m and cubic TiO$_2$ phases it was difficult to determine the approximate ratios of precursor left, however due to the visible amount of Li$_2$CO$_3$ remaining it was assumed some amount of TiO$_2$ was present. This sample was not considered for use in further studies.

The two lower temperature (700°C and 750°C) samples contained R$\bar{3}$m (003) peaks at approximately 18.5°, indicating some degree of ordering, as discussed using the geometric

structure factor in Section 2.5.4. As temperature was increased further, the remaining samples appeared 100% disordered as the (003) peak was no longer visible.
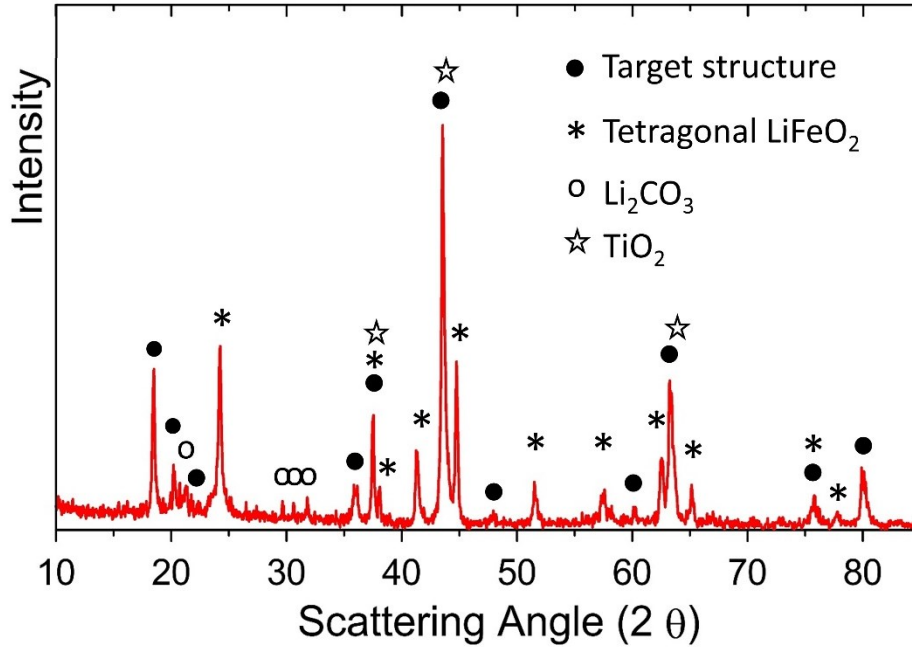
Figure 3.1: Multiple phase identification of the x = 0.15 600°C sample. The "target structure" was Fm$\bar{3}$m or R$\bar{3}$m, however super-lattice ordering in TM layers was also observed during ordering, so C2/m super-lattice peaks were included. Other phases included tetragonal LiFeO$_2$, TiO$_2$ and residual Li$_2$CO$_3$ indicating incomplete synthesis.

Fitting of each pattern was then performed using the method outlined in Section 2.5.3. Each pattern was first fitted using an R$\bar{3}$m space group with mixing allowed between layers. The samples with no (003) peak were then fitted with a cubic rocksalt Fm$\bar{3}$m structure for comparison. The results of these fittings are shown in Table 3.1. Fitting parameters were plotted and are shown in Figure 3.3 for a visual comparison. The samples that appeared completely disordered (800, 900, 1000) did not converge well using the R$\bar{3}$m space group, due to attempting to fit zero intensity peaks with many varying parameters. Obtained R$\bar{3}$m fits for these samples (red dots in Figure 3.3) did not follow expected downwards trends for the a and c lattice, and followed a scattered trend in $c/3a$. When

56

these samples were fitted using cubic $Fm\bar{3}m$, the trends in a and c were more acceptable and were clearly distinguishable from the more ordered, lower temperature samples. Due to the geometry in a cubic space group, $c/3a$ and amount of cation disorder was constrained at 1.6333 and 1.00, respectively. Additionally, the Bragg R-factor, a measure of goodness of calculated to experimental peak fitting, was lower for two of the three $Fm\bar{3}m$ fits. The high degree of disorder in the $R\bar{3}m$ fits correlated well with the assumption of complete disorder, so it was assumed the 800, 900 and 1000°C samples were, in fact, cubic and 100% disordered, while the 700 and 750°C samples had 51% and 55% disorder, respectively.
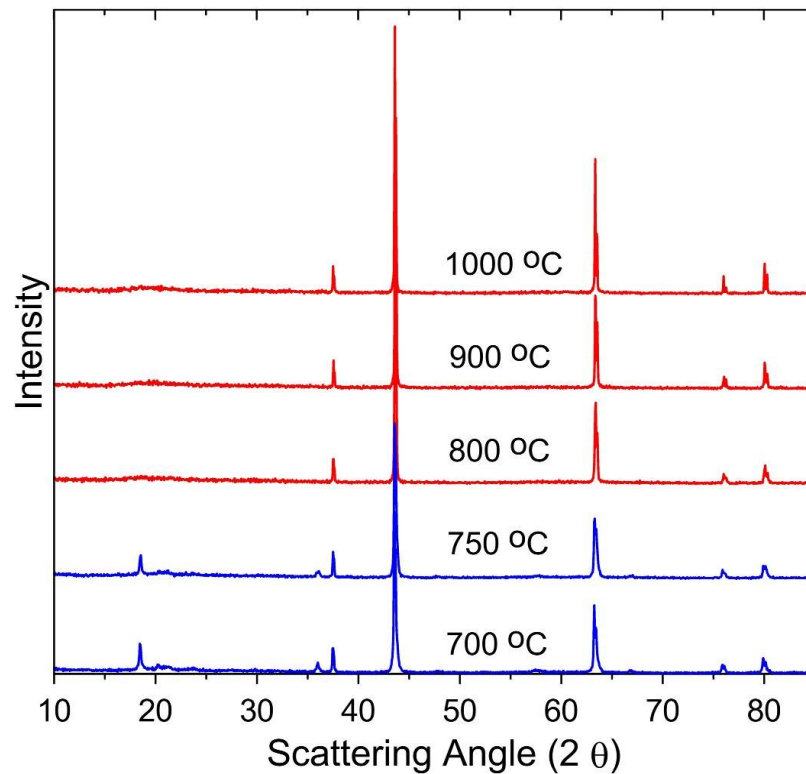
Figure 3.2: Diffraction patterns of single phase samples with some degree of visible ordering (blue) and disordered high temperature samples (red).

Figure 3.4 shows the experimental and calculated patterns for the two R$\overline{3}$m and three Fm$\overline{3}$m fits. Peak splitting in Figure 3.4 was due to Cu-Kα_1 and Cu-Kα_2 radiation. The ratio used in calculations was fixed at 2:1 Kα_2: Kα_1.

The findings of this section demonstrate how synthesis temperature may be used to vary the amount of disorder. However, due to lithium loss at higher temperatures, either excess Li$_2$CO$_3$ is needed or shorter synthesis times are required. The effect of lithium loss was apparent in electrochemical testing. The electrochemical performance of these materials is summarized in Chapter 4 and was used to determine the synthesis temperature of the 700°C and 800°C series. Since 700°C yielded some degree of disorder and complete disorder was obtained at 800°C with little lithium loss, these temperatures were chosen in order to compare the effect of the two temperatures across the solid solution as well the effect on electrochemical performance.

Table 3.1: XRD fitting parameters for different synthesis temperatures using R$\overline{3}$m and Fm$\overline{3}$m space groups.

Temperature (°C)	a (Å) ±0.001 Å	c (Å) ±0.001 Å	Disorder (±1 %)	$c/3a$ ±0.0001	Bragg R factor
		R$\overline{3}$m Fitting			
700	2.9384	14.4075	0.51	1.6344	4.96
750	2.9337	14.3914	0.55	1.6352	4.22
800	2.9325	14.3849	0.96	1.6351	4.89
900	2.9352	14.3696	0.89	1.6319	5.74
1000	2.9335	14.3796	0.85	1.6340	3.69
		Fm$\overline{3}$m Fitting			
800	2.9334	14.3735	1.00	1.6333	3.59
900	2.9346	14.3791	1.00	1.6333	4.80
1000	2.9323	14.3680	1.00	1.6333	4.20
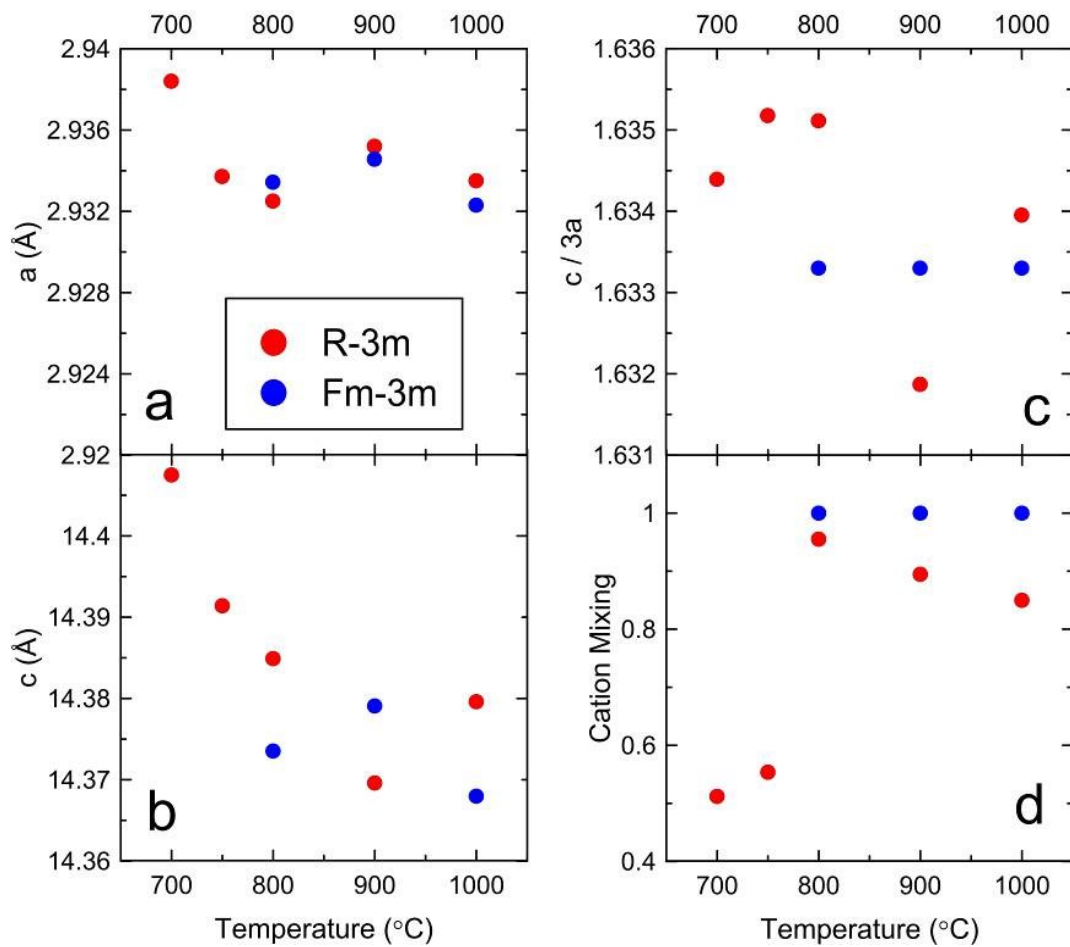
Figure 3.3: Fitting parameters for samples synthesized at various temperatures. Red circles indicate samples fitted with R$\bar{3}$m and red circles indicate samples fitted assuming a cubic Fm$\bar{3}$m space group with 100% disorder.
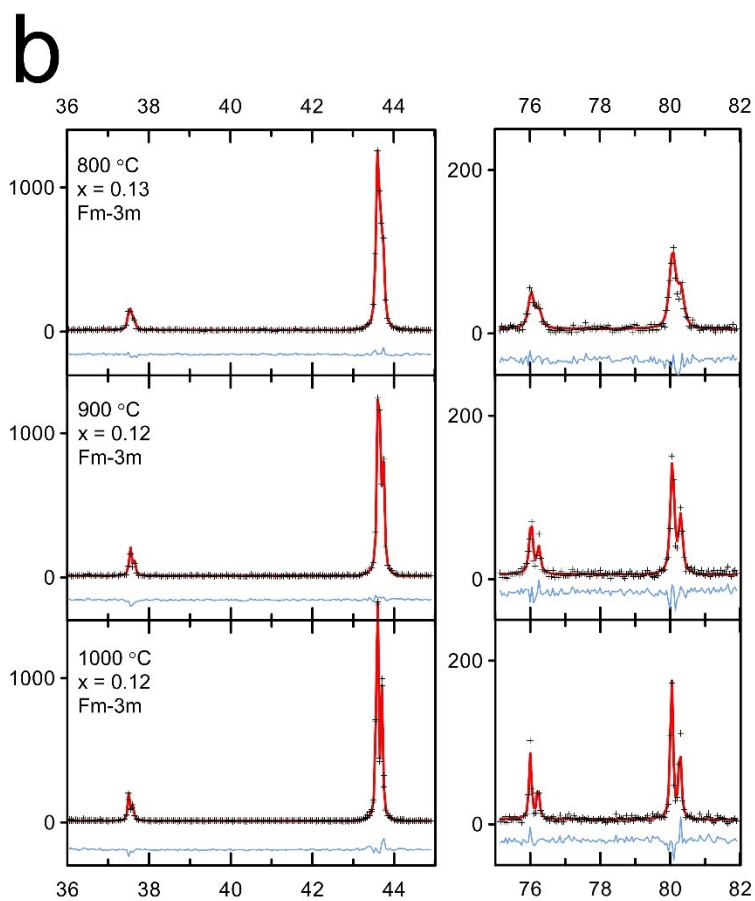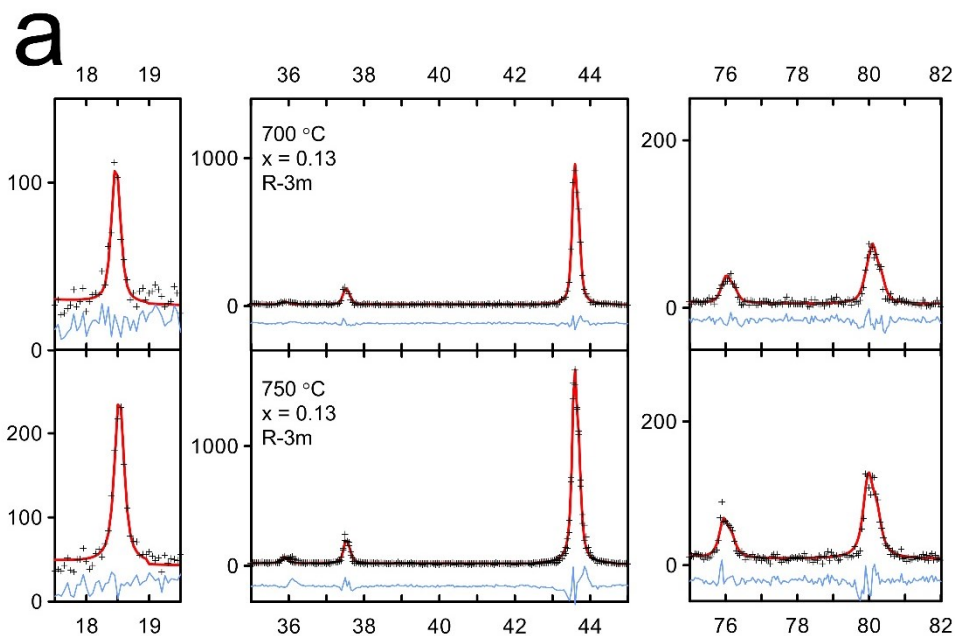
Figure 3.4: XRD fitting of a) samples synthesized at 700 and 750°C using the R$\bar{3}$m space group allowing ordering between layers and b) samples synthesized at 800, 900 and 1000°C using the Fm$\bar{3}$m space group. Experimental data is represented by black crosses, the calculation by red lines, and the difference by blue lines

3.2 700°C and 800°C Structural Analysis

3.2.1 Full Series Analysis

Samples synthesized as described in Section 2.2 at 700°C and 800°C were characterized on the Seimens D-5000 at in the Dahn Lab at Dalhousie, while four samples were characterized at the Canadian Light Source in order to obtain high resolution patterns. As observed in Section 3.1, fitting using the $R\bar{3}m$ space group on ordered samples was difficult due to the high noise-to-signal ratio. The (003) peak can be very small due to the cancellation of d_{003} spacings shown in Section 2.5.3, and difficult to fit with a lab source XRD. Other $R\bar{3}m$ peaks are much smaller in magnitude than (003) and are difficult to refine at high degrees of disorder.

The results of the 700°C and 800°C series are summarized in Figure 3.5. As expected from the temperature study results the 700°C series exhibited ordering at lower x than the 800°C series. However, slight ordering in the 800°C series appeared in the $x = 0.13$ sample, where in the temperature study the 800°C $x = 0.13$ sample was found to be disordered. The 700°C $x = 0.13$ sample appeared very similar to the sample synthesized in the temperature study. Due to the slight variation in the two $x = 0.13$, 800°C samples, a "critical temperature" which allowed disorder at this composition may exist around 800°C. As Li and Ti replaced Fe with increasing x, the (003) peak became more visible indicating an increase in ordering. Disorder in the solid solution was therefore dependent on composition as well as temperature.
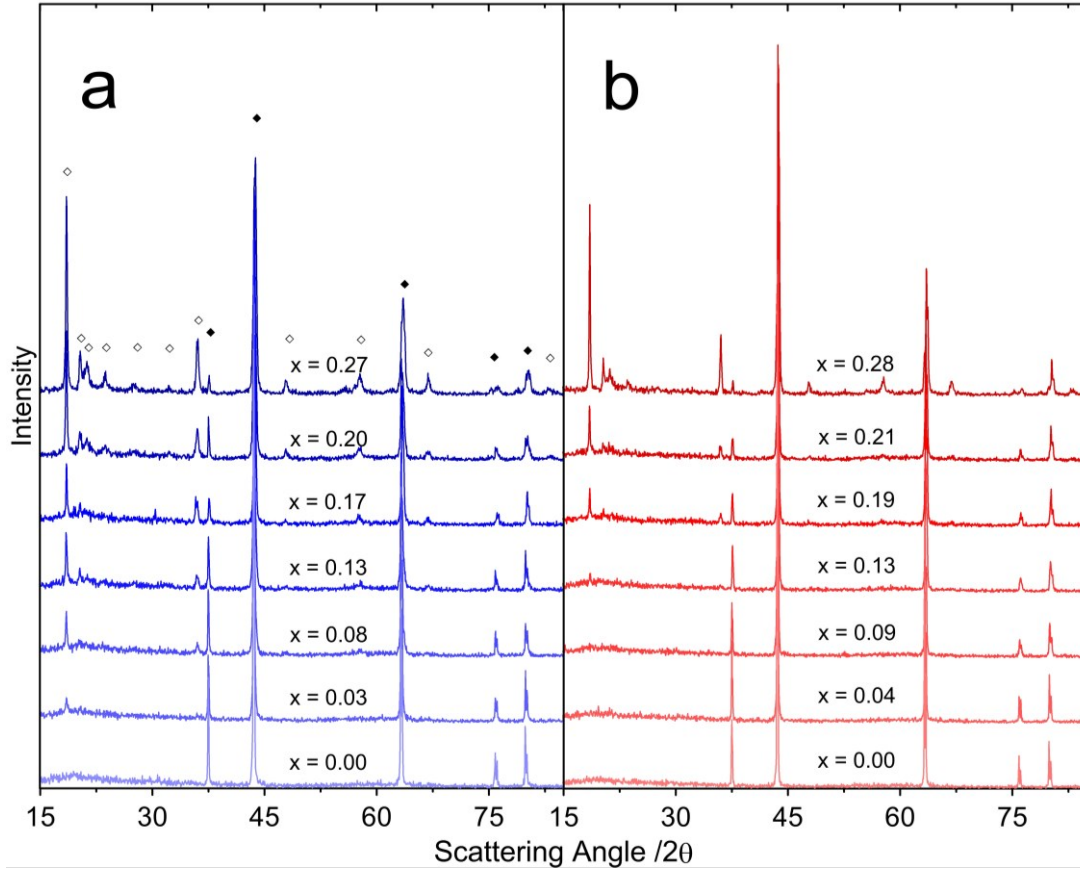
Figure 3.5: D-5000 diffraction patterns for the a) 700°C and b) 800°C series. Peaks corresponding to C2/m space group are indexed with hollow diamonds, and peaks corresponding to both C2/m and Fm$\overline{3}$m are shown with solid diamonds.

In addition to the appearance of the (003) and other R$\overline{3}$m peaks with ordering, peaks at $2\theta = 20°$ to $23°$ appeared, indicating super-lattice ordering in the TM layer. These peaks can be indexed using the monoclinic C2/m space group, briefly discussed in Section 1.2.2, where lithium atoms in the TM layer preferentially populate sites in the middle of TM octahedral sites in a hexagonal arrangement. Refinement was attempted using a C/2m space group, however would not converge for many samples. By excluding angles containing super-lattice peaks, refinement using the R$\overline{3}$m space group was performed. The transition from disordered Fm$\overline{3}$m (α-LiFeO$_2$) to ordered C2/m (Li$_2$TiO$_3$) was expected with increasing Li content as each end of the solid solution line occupies the respective structure.

62

Fitting was again performed following the routine outlined in Section 2.5.4. Again, samples with no visible R$\bar{3}$m peaks converged in fewer steps and generally yielded lower Bragg R-factors when fitted with Fm$\bar{3}$m. Therefore both $x = 0$ samples as well as $x = 0.04$ and $x = 0.09$ at 800°C were determined to be 100% disordered. Results of for all samples fitted with both space groups are shown in Table 3.2. The final fitted R$\bar{3}$m (hexagonal setting) patterns for the 800°C series are shown in Figure 3.6, and Fm$\bar{3}$m in Figure 3.7. Figure 3.8 provides a visual comparison of fitted lattice and disorder parameters fitted with R$\bar{3}$m (dark symbols) and Fm$\bar{3}$m (light symbols) listed in Table 3.2.

Table 3.2: Refinement parameters for the 700°C and 800°C composition series

Temp	Space Group	x	a (Å) ±0.001 Å	c (Å) ±0.001 Å	c/3a ±0.0001	Disorder	Bragg R-factor
800°C		0.00	2.939	14.400	1.6333	1	2.95
	Fm$\bar{3}$m	0.04	2.938	14.396	1.6333	1	4.31
		0.09	2.936	14.385	1.6333	1	4.65
		0.00	2.937	14.398	1.6341	0.85 (1)	5.74
		0.04	2.937	14.400	1.6341	0.85(1)	5.51
		0.09	2.935	14.391	1.6345	0.849(9)	4.76
	R$\bar{3}$m	0.13	2.933	14.383	1.6345	0.762(9)	4.20
		0.19	2.930	14.373	1.6351	0.605(7)	4.09
		0.21	2.929	14.366	1.6346	0.550(6)	6.02
		0.28	2.923	14.367	1.6386	0.234(3)	7.04
700°C	Fm$\bar{3}$m	0.00	2.940	14.405	1.6333	1	4.59
		0.00	2.940	14.406	1.6331	0.833(9)	3.68
		0.03	2.939	14.408	1.6342	0.748(8)	6.41
		0.08	2.939	14.404	1.6336	0.682(8)	5.08
	R$\bar{3}$m	0.13	2.938	14.406	1.6343	0.538(7)	4.66
		0.17	2.932	14.379	1.6349	0.437(5)	5.94
		0.21	2.932	14.397	1.6371	0.315(4)	4.54
		0.26	2.926	14.403	1.6407	0.296(4)	4.25
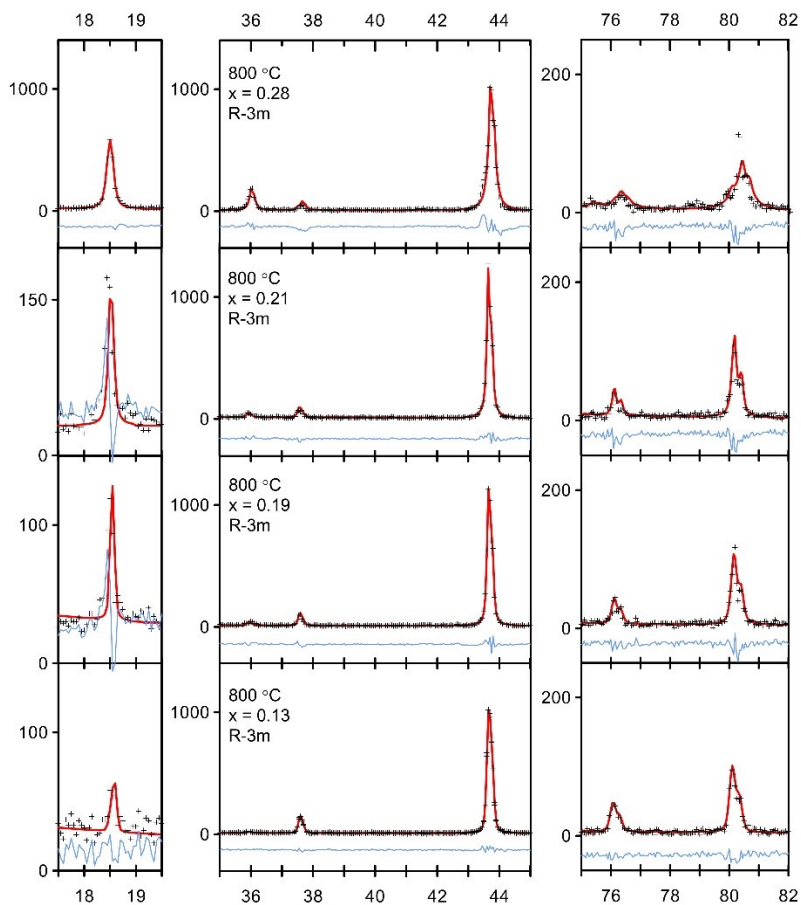
Figure 3.6: Diffraction pattern fitting for 800°C R$\bar{3}$m samples. Difficulty fitting the (003) peak arose due to low signal to noise ratios. Data is shown in black crosses, fitting in red and the difference in blue.
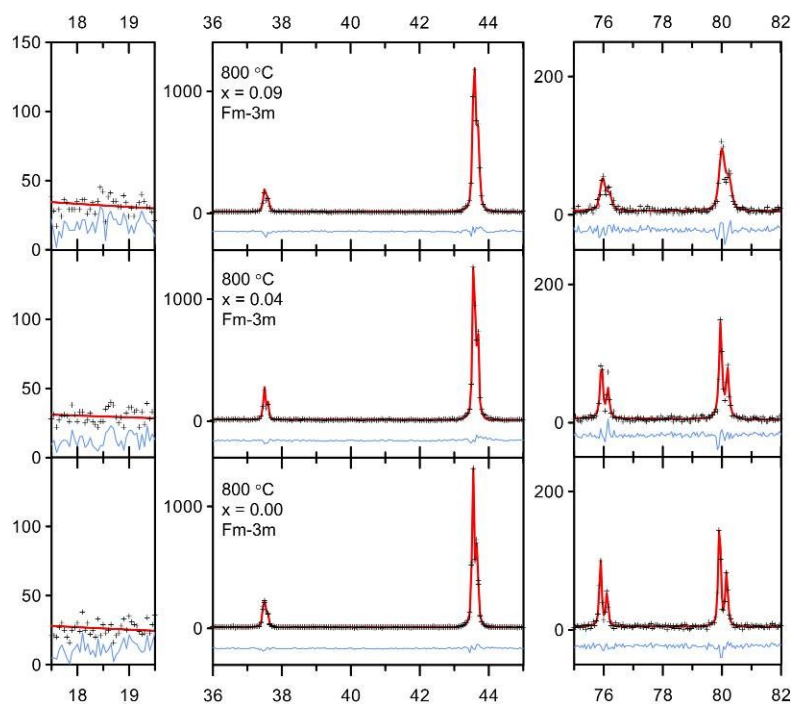
Figure 3.7: Diffraction pattern fitting for disordered 800°C Fm$\bar{3}$m samples. Data is shown in black crosses, fitting in red and the difference in blue.

64
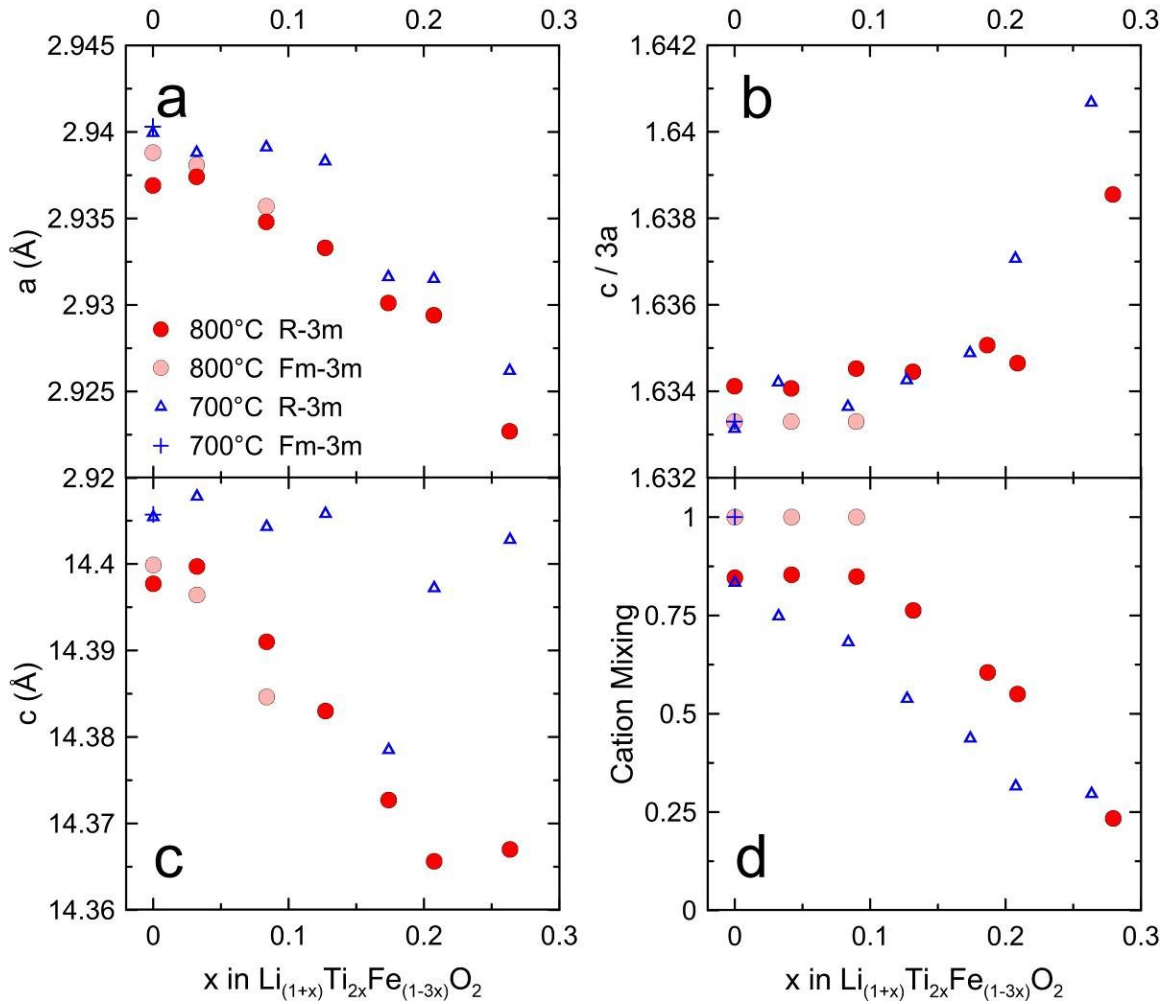
Figure 3.8: Visual representation of refinement parameters a) a lattice, b) $c/3a$, c) c lattice, and d) disorder (TM_{Li}/TM_{TM}) shown in Table 3.2 for the 800°C (red) and 700°C (blue) series. The full series fitted with $R\bar{3}m$ is shown in dark symbols and disordered samples also fitted with $Fm\bar{3}m$ are shown in light colours.

Table 3.2 shows $Fm\bar{3}m$ fitting yielded much better fits $x = 0.00$, $x = 0.04$ and $x = 0.09$ 800°C samples, however the $x = 0.00$ 700°C sample had a higher R-factor. The observed fitting parameters trends in Figure 3.8 were more acceptable when the $Fm\bar{3}m$ fits (light symbols) were used, though the 700°C sample did not experience a significant change in a or c between the different fitting methods. The $Fm\bar{3}m$ fits were accepted over $R\bar{3}m$ for these samples and are considered in the following discussion.

The series synthesized at 800°C showed a steadily decreasing trend in *a* and *c* in Figure 3.8a and 3.8c, as well as degree of disorder (when $x > 0.09$), indicating smaller tetrahedral site size with higher Li and Ti content and lower Fe content. As the Li content increased, the structure started to deviate from near cubic (small increase in $c/3a$ in Figure 3.8b) with the observed increase in ordering, as expected of an ordered-layered structure. The 700°C series had less of a change in the *c* lattice except for one outlier at $x = 0.18$. This outlier was the sample in Section 2.3.2 which did not fit the trend in colour (off-yellow instead of brown). A similar trend in the *a* lattice and also followed a similar but more pronounced increasing trend in $c/3a$ which correlated with the higher degree of order. Lattice parameters should increase with ordering as seen in the previous temperature study, however as *x* increased in the series, ordering increased and lattice parameters decreased. This trend is instead due to the smaller layer spacing in Li_2TiO_3 compared to that of $LiFeO_2$ affecting lattice parameters to a larger degree than the effect from ordering. A near linear decreasing trend in the degree of disorder was observed once cation ordering started at $x = 0.03$, compared to $x = 0.13$ at 800 °C, in which the structure maintained disorder at higher values of x. The *a* and *c* lattice parameters were larger for all values of *x* at 700°C, consistent with the higher degree of ordering. The trends between the two temperature results support those in the previous temperature study, indicating temperature may be used as a tool for controlling the amount of disorder between layers.

3.2.2 Synchrotron XRD

As seen in Figures 3.6 and 3.7, the (003) peak, which is the most prominent R$\bar{3}$m peak, is difficult to fit until $x = 0.28$ due to its magnitude compared to that of the background. In

order to reduce the signal to noise ratio of small $R\bar{3}m$ peaks, synchrotron XRD

measurements were taken on samples $x = 0.00$, $x = 0.09$, $x = 0.19$, and $x = 0.28$. An example

of the obtained Debye-Sherrer ring patterns for $x = 0.00$ is shown in Figure 3.9a. Once

integrated and the kapton background was removed, further difficulty arose from

background fitting. Short range, amorphous-like behaviour contributed to very broad

(003), (006), (009) and (00 12) peaks in the background, as shown in Figure 3.9b. The

broad (003) peak was slightly observed in the D-5000 patterns but was easily fitted with a

polynomial background since the magnitudes of noise and broad peaks were on the same

order of magnitude. The synchrotron XRD background was therefore manually fitted for

ease of analysis. Another feature that was not visible in D-5000 data was slight residual

Li_2CO_3, as seen in Figure 3.9b. The magnitude of these peaks was negligible compared to

the sample signal and only visible when viewed on a logarithmic scale or zoomed in to

view only the background. Fitting of these four patterns is shown in Figure 3.10 and fitting

parameters shown in Table 3.3.

Table 3.3: Fitting parameters of synchrotron XRD patterns

x	a (Å) ±0.001 Å	c (Å) ±0.001 Å	c/3a ±0.0001	Mixing	R-Factor
0.00	2.93725	14.39224	1.6333	1	3.56
0.09	2.93987	14.40506	1.6333	1	4.17
0.19	2.93490	14.38660	1.6340	0.614(7)	7.04
0.28	2.92980	14.41100	1.6400	0.128(1)	3.89
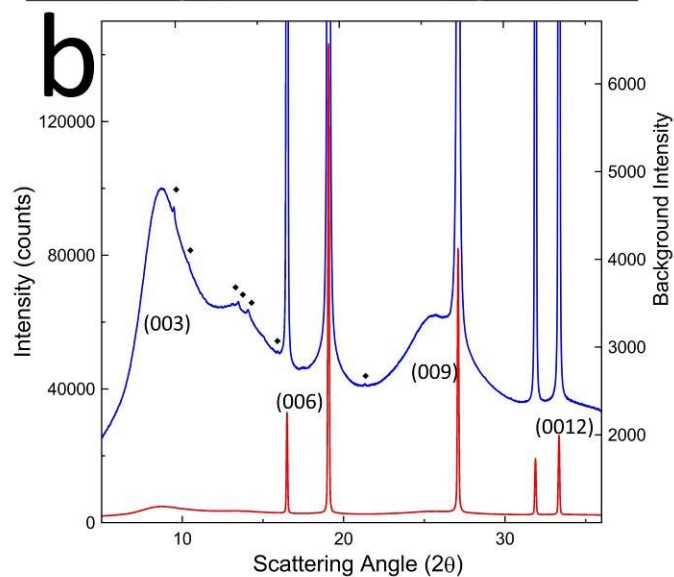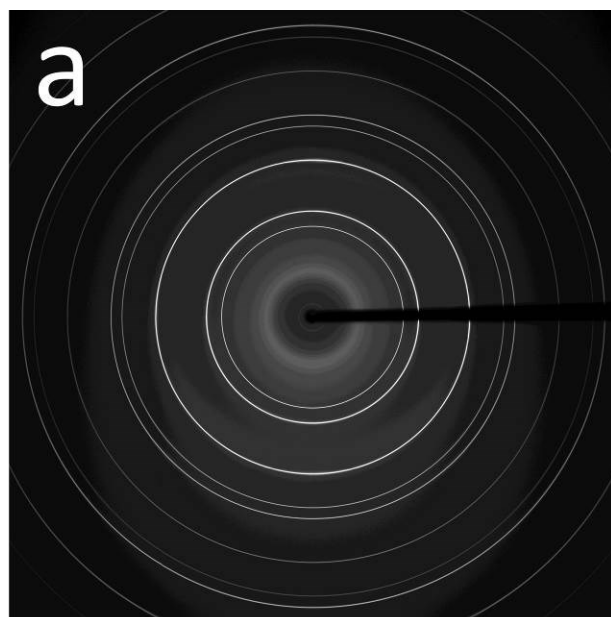
Figure 3.9: a) Example of a Debye-Sherrer ring image obtained for $x = 0.00$. The image contrast and brightness were modified to enhance background features. b) Integrated XRD pattern with kapton background removed (red) and a blow up of the broad background peaks (blue) with small Li_2CO_3 peaks (black diamonds) demonstrating the resolution of this technique. The peak clipping in the blue pattern was set to less than 5000 counts.
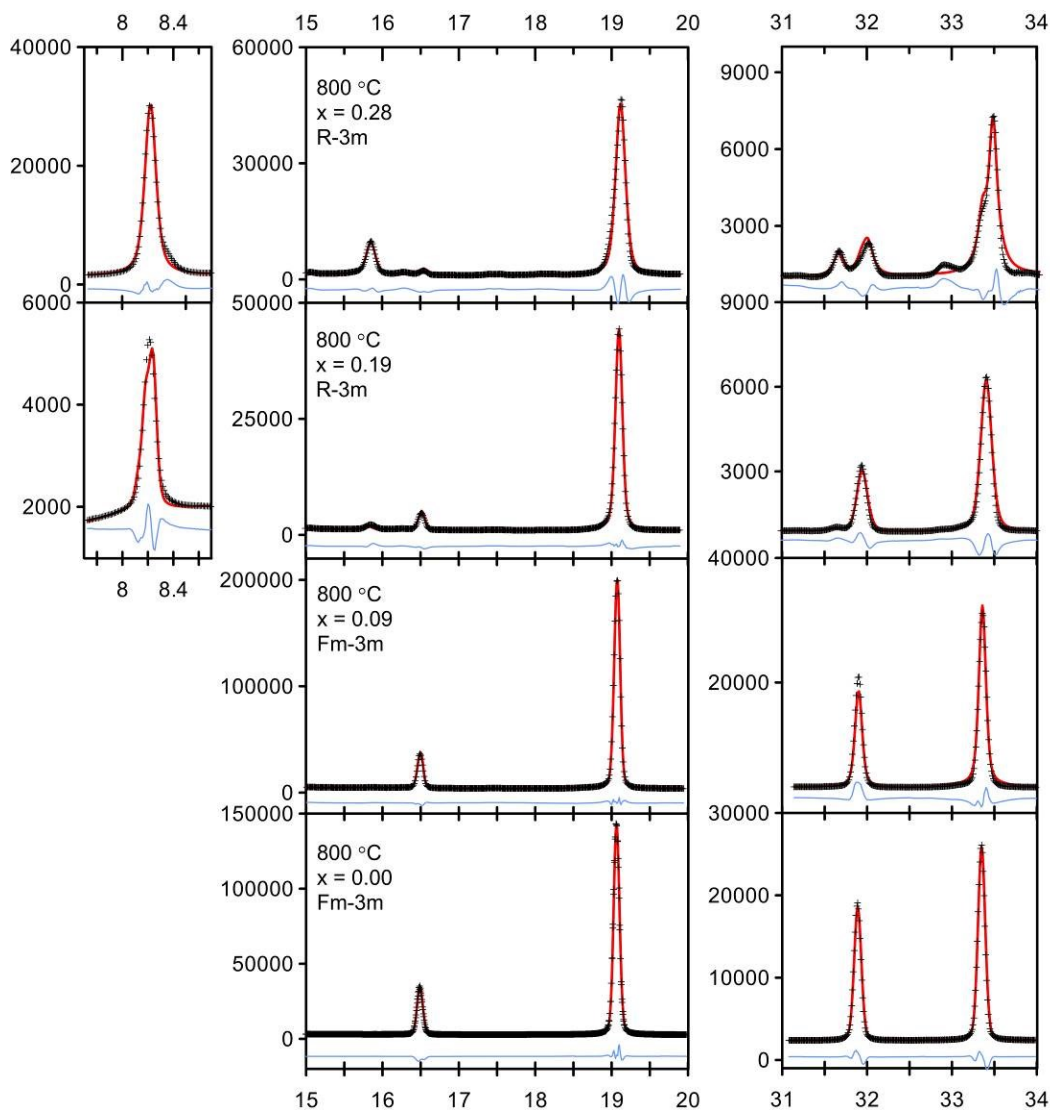
Figure 3.10: Synchrotron XRD fitting of 800°C *x* = 0.00, 0.09, 0.21, 0.28 samples. Peak fitting was more successful in disordered samples, however manual background fitting may have caused biased or unreliable fits. Note differences in vertical scaling for ease of comparison.

The fitting results in Table 3.3 and Figure 3.11 show that synchrotron data refinement did not have a profound effect on the amount of *c*/3*a* or the degree of disorder compared to the D-5000 data, however the *c* lattice parameter did not follow the same trends. All but the *x* = 0.00 sample followed a decreasing trend in the *a* lattice. The *c* lattice did not follow any trend and did not agree with D-5000 parameters. One possible reason for the

69

disagreement between detection methods include manual background correction. If the background around fitted peaks was adjusted, parameters changed significantly. A better understanding of the sample background could be used to simulate a background function based on the broad c-axis ordering peaks. Other possibilities for lattice parameter disagreement could involve issues with calibration and background correction. The beamline was experiencing beam drift during the duration of these experiments. This caused an asymmetry (which can be seen slightly in Figure 3.9a) which varied between samples, as well as inconsistency in detection time, creating difficulty in the kapton capillary background correction. The inconsistent collection time was the reason for large variance in the scale of patterns in Figure 3.6 and 3.7.
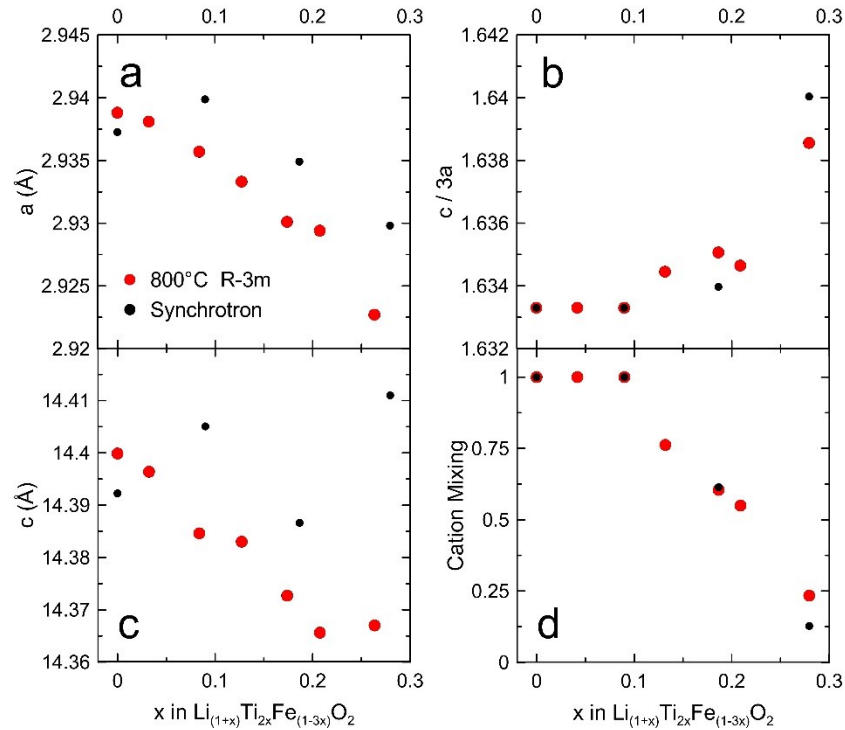
Figure 3.11: Accepted fitting parameters from the D-5000 *vs.* fitted synchrotron data. Trends in *c* and *a* were not consistent with D-5000 data, however consistent trends were observed *c*/3*a* and the amount of disorder.

Though the results for synchrotron-measured lattice parameters were not in agreement with D-5000, results for the degree of disorder and lattice parameter ratios followed very similar trends, verifying the degree of disorder in the samples. Any future work should include structure-related background corrections if synchrotron XRD is to be of use for accurate characterization. Some recent works observing similar amorphous background behaviour did not report XRD fitting due to issues with characterizing the background, and instead only included calculated reference patterns.[59,60] Other works do not fit low angle regions due to the absence of the (003) peak or do not require accurate background fitting due to lab sourced detection methods. With the recent interest in disordered materials, a method of characterizing this background would be of use in order to accurately model and refine materials with some degree of order present, as in this case. Any future work involving very fine refinement such as *in-situ* XRD experiments will require these methods in order to characterize behaviour of small (003) peaks such as in $x = 0.13$ which, as shown in Figure 1.9, should yield the highest capacity based on Monte Carlo simulations and available redox.[27]

XRD measurement and refinement was a useful tool in structural analysis and successfully characterized the degree of disorder in all samples as well as provided information on the trends of lattice parameters at different compositions and degrees of disorder. The previous results and structural characterization will be used to aid in the discussion of the electrochemical performance and mechanisms in Chapters 4 and 5.

Chapter 4: Electrochemical Performance

Due to the many comparisons made in this work to other systems, the lack of work in disordered materials and multiple proposed mechanisms between previous works on both this system and related systems, the electrochemical analysis discussed in this chapter is primarily speculation and requires future work to confirm the proposed mechanisms.

4.1 Temperature Series

4.1.1 First Cycle Capacity

Coin cells in the temperature series (target composition of $Li_{1.15}Ti_{0.30}Fe_{0.55}O_2$) were cycled at a rate of C/40 at 40°C. The expected capacity for the ICP-determined compositions was approximately 171 mAh/g (assuming $x = 0.13$). The capacity at this composition is at the intersection of the available 0-TM and redox capacities, so all 0-TM lithium may de-intercalate *via* $Fe^{3+/4+}$ oxidation. Two coin cells were cycled at each temperature to verify reproducibility. Though this study was primarily focussed on determining the first charge capacity of these materials, the cells were cycled continuously for many cycles in order to characterize reversible trends and electrochemical mechanisms, as well as to compare with similar studies for consistency. The temperature study cells were intended as trials for designing the solid solution series, so the upper and lower voltage cut offs were set to 4.8 V and 1.5 V respectively in order to determine voltage ranges for future studies. The first charge-discharge for each synthesis temperature made with an 80:10:10 active material to carbon and PVDF ratio electrode is shown in Figure 4.1a. The 700°C cells were able to reach almost 156 mAh/g. In an attempt to increase capacity in the 4.2 V plateau, 85:10:5 and 92:4:4 ratios were also tested and are shown in Figure 4.1b.

The initial results showed dramatically decreasing capacity with an increase in synthesis temperature. The degree of lithium loss was not much greater at high temperature (x = 0.12 at 900°, 1000°C and x = 0.13 at 700°C, 800°C), however the lattice parameters did also decrease at higher temperatures. A combination of lithium loss, lattice shrinkage, as well as a non-optimal carbon and binder mixture may explain the difference in performance between the different synthesis temperatures. Figure 4.1 also demonstrates that these materials are not of interest for commercial applications due to large hysteresis and poor reversible capacity. However, the first charge capacity may still be compared with the expected theoretical capacity to verify Lee's theory.[27]
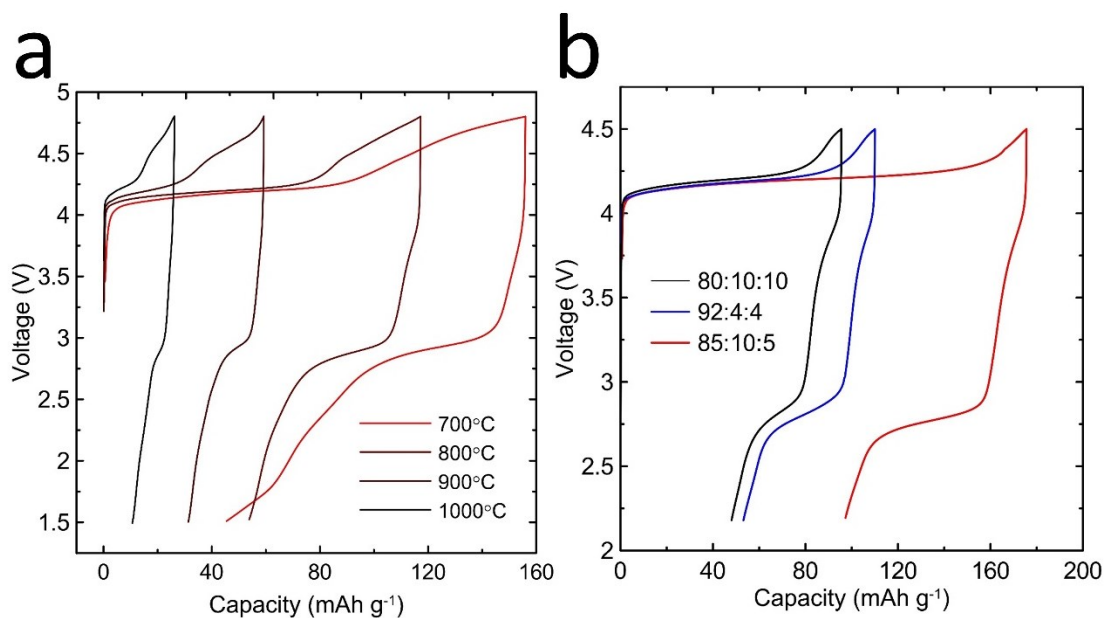
Figure 4.1: Temperature series voltage curves a) for each synthesis temperature tested between 1.5 – 4.8 V and b) different active material to carbon and PVDF binder ratios for 800°C x = 0.13 materials.

A large hysteresis in excess of 1 V, and two smaller plateaus were observed during discharge. This behaviour has been noted before in the literature in Fe-containing materials, and is consistent with other studies in the $Li_{(1+x)}Ti_{2x}Fe_{(1-3x)}O_2$ solid solution as well as other layered, Fe containing chemistries.[24,25,61,62] A large plateau between 4.05 V

to 4.3 V was consistent with past studies on similar Li_2TiO_3 - $LiFeO_2$ solid solution materials, characterized as $Fe^{3+/4+}$ oxidation.[24,25] Above 4.5 V another plateau appears and could be due to electrolyte decomposition or oxygen release (coupled with Fe reduction) from the electrode material, which has been characterized by McCalla *et al.* at these voltages in Li_4SbFeO_4 layered materials with very similar electrochemical behaviour.[63] McCalla *et al.* also proposed that a $O^{2-/1-}$ charge compensation mechanism also occurs in the 4.2 V plateau and the small discharge feature at approximately 4.0 V to 3.7 V corresponds to the reduction of oxygen species as well as Fe^{4+}.[63,64] These processes were later explored in Section 4.3 using similar cycling protocols to McCalla *et al.* and discussed further and in Chapter 5, where XAS was used to characterize the electrochemical contribution of oxygen. The 2.8 V – 3.0 V plateau corresponds to $Fe^{4+/3+}$ reduction and has been proposed by McCalla *et al.* to also contain capacity due to oxygen reacting with lithium.[63] The small feature at 1.7 V has been shown to correspond to further reduction of $Fe^{3+/2+}$ which may cause irreversible structural changes to the material.[24,25] From these results it was determined that an optimal range for full composition series cycling would be 2.2 V – 4.5 V in order to avoid or minimize electrolyte decomposition, oxygen release, as well as low voltage reduction of Fe^{3+} causing changes to the disordered materials.

The 700°C cells demonstrated the highest capacity, able to reach almost 160 mAh/g, however only after the high voltage oxygen release plateau. In an attempt to increase capacity at the ~4 V plateau, $x = 0.15$ 800°C cells were cycled with different carbon and binder ratios. The results in Figure 4.1b show that the 80:10:10 and 92:4:4 ratios demonstrated poor performance, while the 85:10:5 cells reached 175.6 mAh/g, slightly

above the expected capacity of 170 mAh/g. This ratio with a large amount of carbon was consistent with that used in other studies on similar Fe and Ti containing materials.[24,25,63,64]

4.1.2 Cycling Performance

Cells were continuously cycled for up to 25 cycles. The capacity *vs*. number of cycles is shown in Figure 4.2. Dark symbols show charge capacity and light symbols indicate discharge capacity. In all cases during the first charge significant irreversible capacity of approximately 40%-50% was observed. After the first charge, discharge capacity was observed to be higher than charge capacity. After the first 5.5 cycles the 800°C cell was changed to cycle at a faster rate of C/30 and the 900°C and 1000°C cells had the upper voltage cut off increased to 5 V. The higher current lowered the ratio of discharge to charge capacity without affecting the charge capacity. The higher voltage increased capacity but did not significantly change the discharge to charge capacity ratio. The 800°C and 900°C voltage curve for all cycles are shown in Figure 4.3a and 4.3b, respectively. The first cycle, first cycle at the higher current/cut off, and last cycle are highlighted.
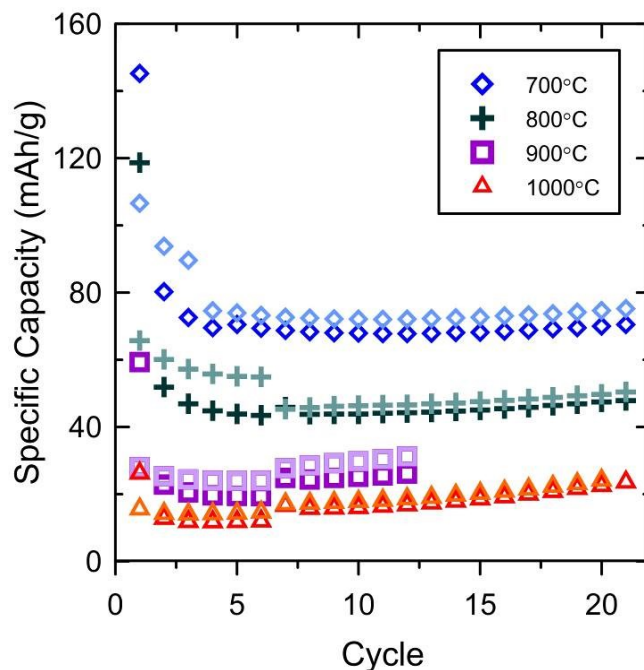
Figure 4.2: Cycle capacities for temperature series cells. Dark and light symbols correspond to charge and discharge capacities, respectively. The changes at cycle 6.5 were due to a C/40 to C/30 rate change in the 700°C and 800°C cells and an upper cut off increase to 5 V in the 900°C and 1000°C cells.

The initial irreversible capacity was likely due to irreversible TM migration in the disordered structure once lithium de-intercalates. Since lithium migration only occurs between 0-TM sites, large portions of the structure are left with "empty" regions once the 0-TM sites empty of lithium. Either structural changes or some TM migration into these sites must then occur. If these changes are not reversible, many 0-TM networks may be blocked when lithium re-intercalates. This mechanism will be explored in later discussions.
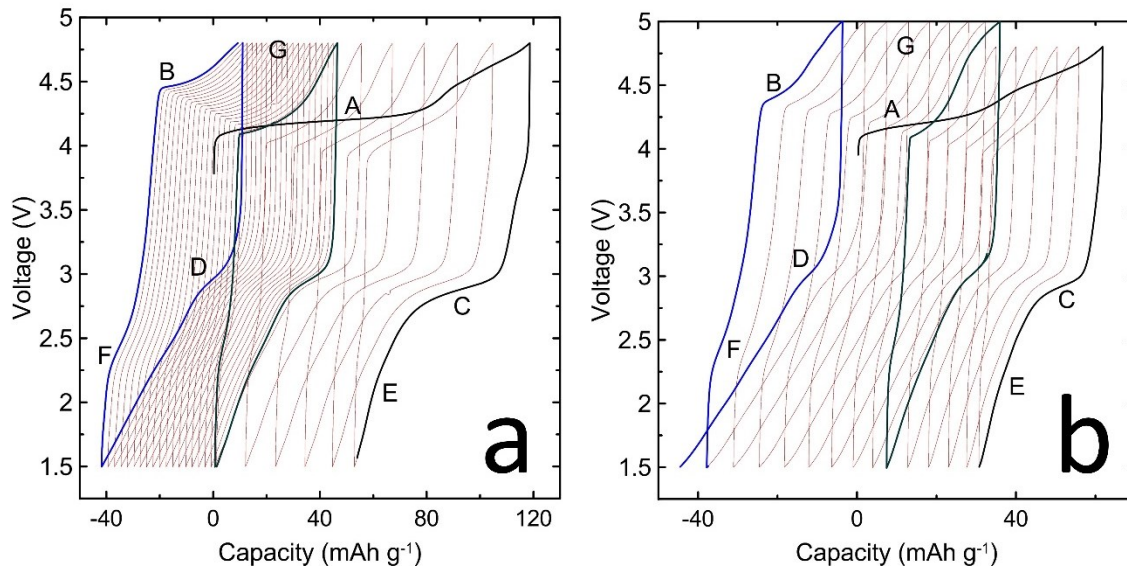
Figure 4.3: a) 800°C cell cycled to 4.8 V at C/40 and C/30 b) 900°C cell cycled to 4.8 V and 5 V. Points A to B and C to D demonstrate the decreasing $Fe^{3+/4+}$ redox plateaus, while the $Fe^{2+/3+}$ region increased from E to F. The high voltage range around G did not experience a significant capacity change.

Though capacity remained relatively constant while cycling, the 800°C cell experienced electrochemical differences between cycles, shown in Figure 4.3a. As cycle number increased, the amount of $Fe^{3+/4+}$ redox decreased while $Fe^{2+/3+}$ increased. The $Fe^{3+/4+}$ plateau also shifted to a higher voltage. The difference in discharge capacity due to the current change can be seen in the middle black highlighted region at the $Fe^{4+/3+}$ plateau. At the higher current, during discharge, less $Fe^{4+/3+}$ occurs. This may be due to the complex 0-TM lithium pathways present in disordered materials and structural changes mentioned above. At high rates lithium may not be able to reversibly intercalate "deep" into the 0-TM networks, or TM migration cannot occur at a fast enough rate, causing changes closer to the surface allowing for $Fe^{3+/2+}$ in these regions.

The upper cut off in the 900°C cell shown in Figure 4.3b did not immediately effect the $Fe^{4+/3+}$ reduction plateau, further supporting the effect of current on 0-TM lithium

intercalation. However, the $Fe^{3+/4+}$ redox plateaus between A – B and C – D decreased over few cycles. Therefore in order to characterize electrochemical performance of these disordered materials, by maximizing capacity due to $Fe^{3+/4+}$ without causing negative effects, low currents and carefully selected voltage ranges were chosen for the solid solution composition series.

Another factor that was not explored was raising the ambient cycling temperature. By raising the temperature of the cell TM mobility could be increased and percolation energy barriers would be slightly lowered. Higher cycling temperatures would therefore increase the rate capability and likely the reversible capacity of disordered materials. Future studies should include reversible capacity and rate dependence on cycling temperature.

4.2 700°C and 800°C Series

Cells in the 700°C and 800°C composition series were cycled at 40°C at a rate of C/60 between 2.2 V and 4.5 V in order to reduce oxygen release and $Fe^{3+/2+}$ reduction as well as allow 0-TM intercalation, as discussed in Section 4.1.2. The first charge-discharge of each cell is shown in Figure 4.4. Though Figure 4.1b showed an 85:10:5 electrode mixture demonstrated the best performance for the $x = 0.13$ 800°C sample, the 700°C samples did not perform as expected, each cell demonstrating lower capacities than the respective compositions in the 800°C series. However, the 800°C series was of primary interest due to the higher degree of disorder in each material.

The extremely low capacities of the $x = 0.00$ samples was accurately predicted by Lee *et al.*'s percolation theory work, due to the low probability of 0-TM channels being able to form a percolating network.[27] The observed trend of increasing capacity, until some limit

is reached, then decreasing capacity was also predicted when Lee's model was combined

with the available Fe redox available. However, the intersection of the two models should

limit capacity at $x = 0.13$. Figure 4.5 shows the 800°C series plotted with the theoretical

capacity curves due to 0-TM lithium and $Fe^{3+/4+}$ redox, respectively.
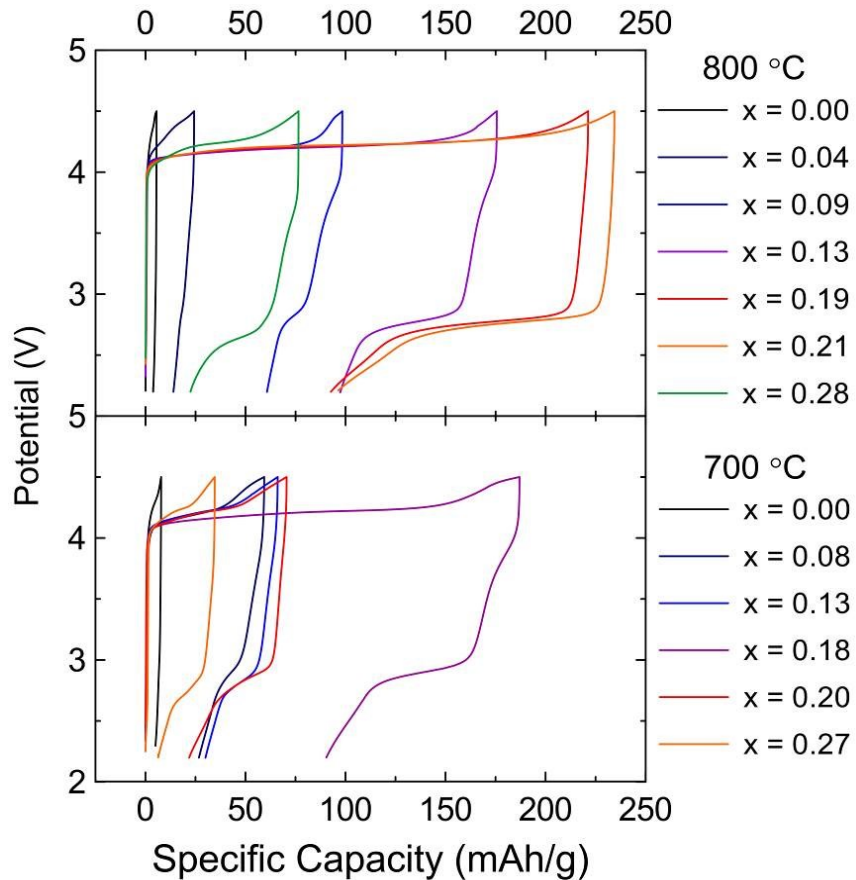
Figure 4.4: First charge performance of the 800°C (upper) and 700°C (lower) composition series. The $x = 0.04$ cells in the 700°C series both failed for unknown reasons and were not reported in results.
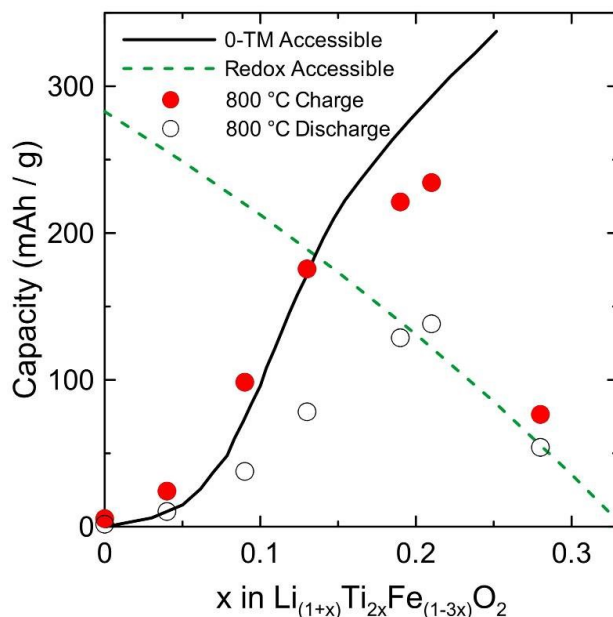
Figure 4.5: First charge (solid red circles) and discharge (hollow circles) capacities of the 800°C series compared to the 0-TM available Li model by Lee *et al.* (black line) and $Fe^{3+/4+}$ theoretical capacity (green dashed line).[27]

In the lithium-limited region from $x = 0.00$ to $x = 0.13$ the series performed very closely to the predicted model. Above $x = 0.13$, the $x = 0.19$ and $x = 0.21$ cells performed much above the theoretical redox capacity, seeming to follow a trend weighted between the two models. The $x = 0.28$ cell performed slightly above the expected capacity. The three redox-limited cells exhibited 37%, 48% and 27% higher capacity than expected, respectively. An oxygen redox charge compensation mechanism was predicted to be the cause of the excess capacity, though as shown in work by McCalla *et al.* on layered Li_2FeSbO_4 materials, oxygen redox is presumed to take place during the 4.1 V plateau also associated with $Fe^{3+/4+}$ oxidation.[63] This creates difficulty in characterizing $O^{2-/1-}$ charge compensation from the electrochemistry during charge. Interestingly in Figure 4.4 the 3.8 V plateau corresponding to oxygen reduction in McCalla's work is present in two lithium limited cells and the $x = 0.28$ cell but not the two high capacity cells, meaning any oxygen charge compensation

may not have been reversible in these compositions. Excess capacity may have also been caused by irreversible electrolyte decomposition reactions at high voltage during the first charge, however the observed discharge capacities were slightly below and above the theoretical capacity in the $x = 0.19$ and $x = 0.21$ materials, respectively. Additionally, no compositions in the 0-TM lithium limited region exhibited significant excess capacity, so electrolyte decomposition was not assumed to have a significant impact on the excess capacity. Considering the impact of irreversible structural mechanisms and good agreement with theoretical capacity in the 0-TM limited region, the participation of oxygen in the observed capacity was likely, however further testing using XAS was needed and discussed in Chapter 5.2. The 700°C $x = 0.18$ cell yielded a slightly higher capacity than expected, though only 27% over the expected capacity. These results may show that a large degree of $O^{2-/1-}$ charge compensation may be detrimental to the subsequent reduction of oxygen. A plot of dq/dV $vs.$ V is shown in Figure 4.6 for the first and second charge-discharge of the redox limited $x = 0.19$, the theoretical maximum $x = 0.13$, and 0-TM limited $x = 0.09$ samples. Figure 4.6 also demonstrates the large irreversible capacity between the first and second cycles in the 4.2 V plateau. The 3.8 V peak associated with $O^{1-/2-}$ reduction plateau is seen in the $x = 0.09$ and $x = 0.13$ dq/dV cells, however the $x = 0.19$ cell did not seem to undergo oxygen reduction, meaning if oxygen compensation exists during charge, it was not reversible during discharge. In order to characterize the charge compensation mechanism, $ex\text{-}situ$ O K-edge XAS was needed. This process is described in detail in Chapter 5.
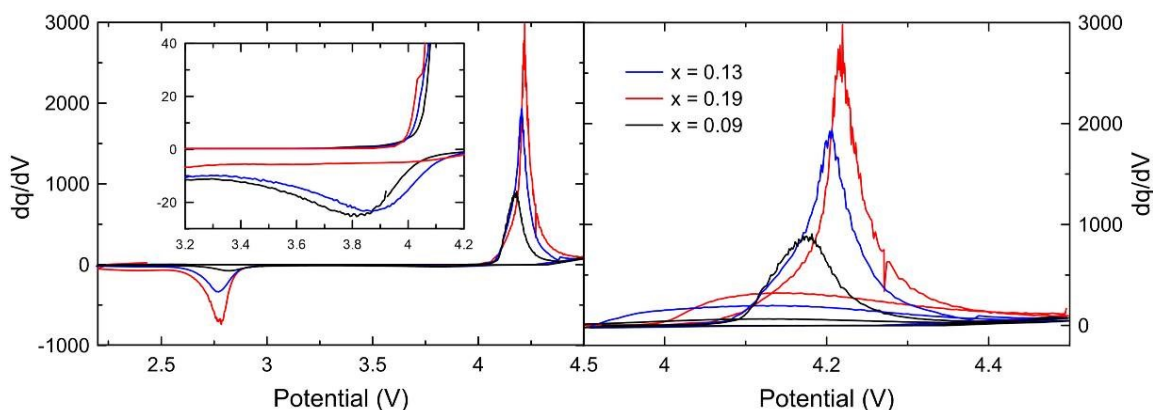
Figure 4.6: dq/dV plots for $x = 0.09$, $x = 0.13$ (blue) and $x = 0.19$ (red) first charge-discharge of the 800°C series. The inset in the left plot shows a blown up region around the proposed $O^{1-/2-}$ reduction plateau in the voltage curves. The right plot shows a blown up view of the result of the capacity difference in the $Fe^{3+/4+}$ charge region between the first and second cycles.

Cell performance over many cycles is shown in Figure 4.7. After 3 cycles the redox limited cells (above $x = 0.13$) were beginning to demonstrate a large discharge to charge capacity ratio and were losing capacity at a much faster rate. The rate was then changed to C/80, which slowed the capacity loss. The difference in the first charge-discharge voltage curve plateaus in Figure 4.5 as well as the dq/dV peaks in Figure 4.6 suggest the $Fe^{3+/4+}$ redox pair was responsible for the large irreversible capacity. Figures 4.8a and 4.8b show dq/dV *vs.* V of the first 10 cycles for $x = 0.13$ (exhibiting possible reversible O redox) and $x = 0.19$ (no observed $O^{1-/2-}$ reduction). The 3.8 V discharge peak in the inset in Figure 4.8a decreases during continuous cycling until it disappears after 10 cycles. After the first cycle the $Fe^{3+/4+}$ peak shifts to a lower potential. After the first cycle the charge and discharge $Fe^{3+/4+}$ redox peaks shift to higher potentials with increasing cycle number. The reduced capacity loss in the first few cycles of the $x = 0.13$ cell compared to the $x = 0.19$ cell seen in Figure 4.7 may have been caused by the reversible $O^{2-/1-}$ mechanism, however it was unclear why the charge compensation in redox limited cells was not reversible.
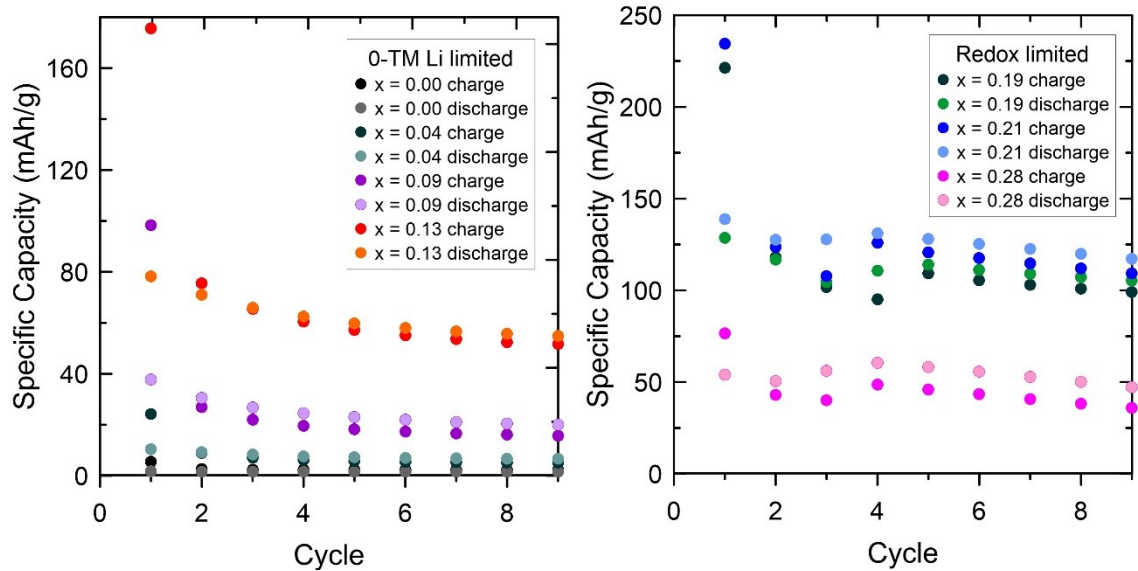
Figure 4.7: Cycling performance for the 800°C series. 0-TM lithium limited cells are shown on the left, and redox limited samples on the right. After 3 cycles the redox limited samples were slowed to a rate of C/80.

Another observed trend in the irreversible capacity during the first cycle is shown in Figure 4.9, and was independent of the presence of a 3.8 V plateau. As x increased, the fractional reversible capacity also increased almost linearly in both series. One likely explanation for this trend could have been due to the increase in 0-TM sites compared to higher n-TM sites. It was determined earlier that the cause of large irreversible capacity was likely due to TM migration into "empty" 0-TM regions once Li de-intercalates, blocking some channels for re-intercalation. Once the first charge-discharge rearrangement is completed, migration would likely be minimal. When lithium content is increased there is a higher fraction of 0-TM sites, leading to more structure spanning networks. Therefore when TM migration occurs in a material with more lithium, there is a lower probability of a network section being blocked.
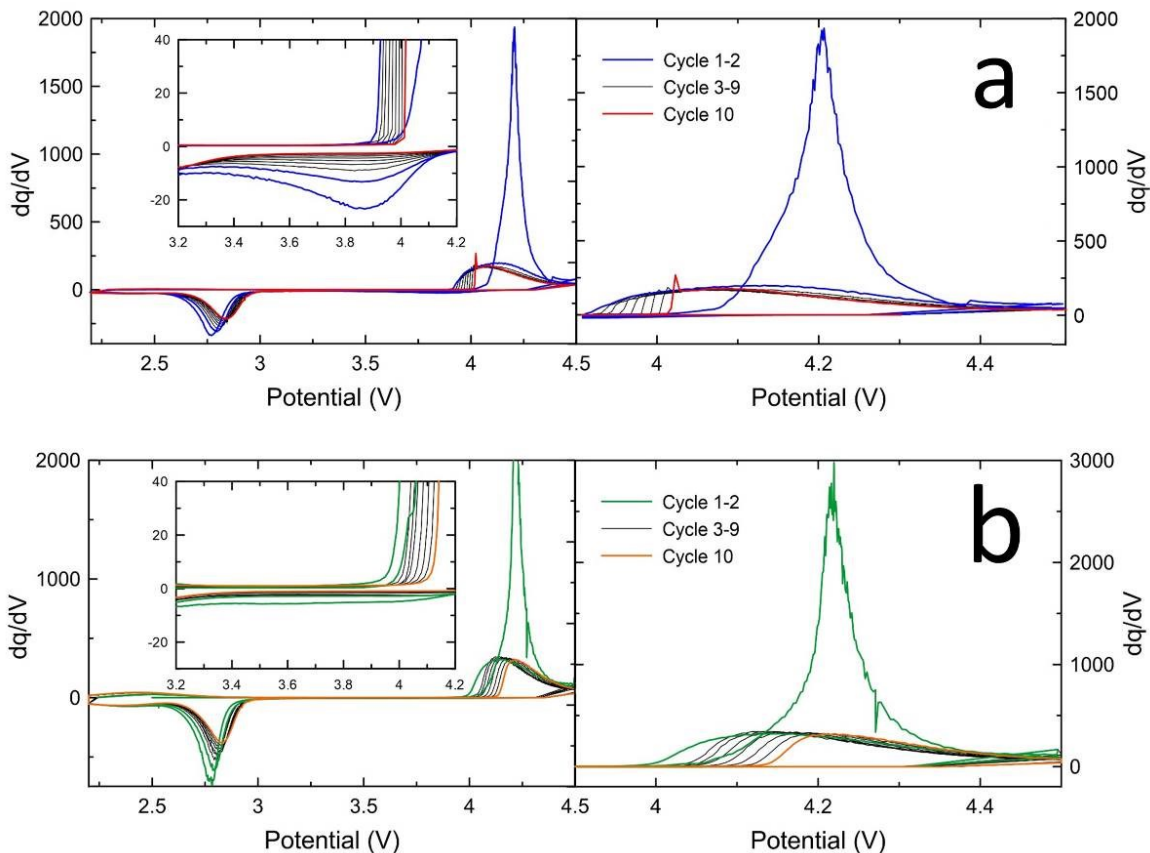
Figure 4.8: dq/dV for the first 10 cycles of a) $x = 0.13$ and b) $x = 0.19$. The first two cycles are shown in a) blue and b) green, while the 10th cycle is shown in a) red and b) orange. The inset is a blown up region around the 3.8 V discharge oxygen reduction peak, and the right plot shows the 4.2 V $Fe^{3+/4+}$ and $O^{2-/1-}$ charge region.

The electrochemical performance of $Li_{(1+x)}Ti_{2x}Fe_{(1-3x)}O_2$ within the 0-TM lithium limited region was successfully shown to approximately follow the model based on percolation theory by Lee *et al.*. Though some compositions in this region exhibited a plateau associated with oxygen redox charge compensation, the capacity due to 0-TM lithium de-intercalation matched the theoretical model very well. In order to understand the charge compensation mechanisms exhibited in the both lithium and redox limited regions, further studies were done using the $x = 0.13$ 800°C material due to the seemingly reversible oxygen redox.
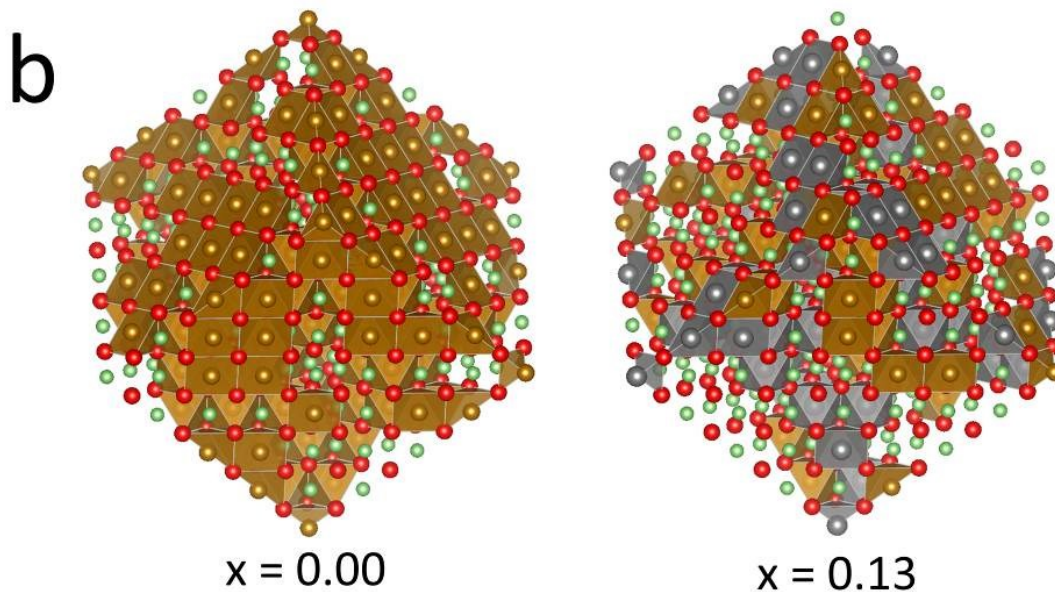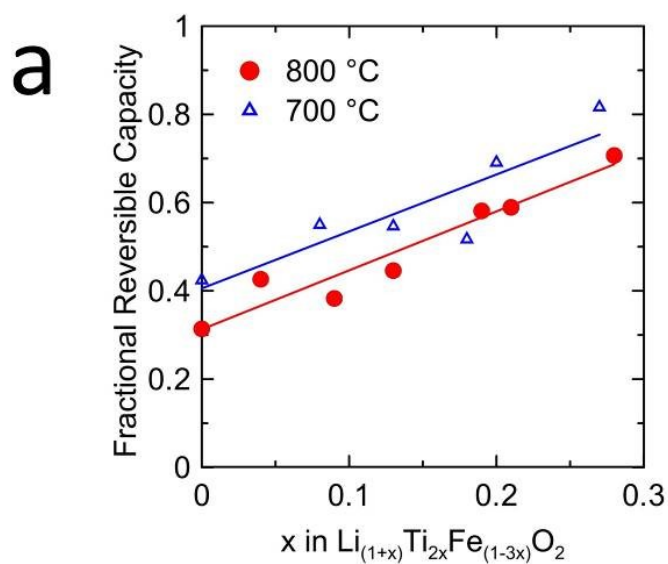
Figure 4.9: a) The observed reversible capacity trend. As the Li:TM ratio increased, more 0-TM networks were available. b) A useful visualization of the amount of networks in two compositions. More networks and less TM sites exist as *x* increases, mitigating the effect of blocked networks by TM migration. Atoms in b) are oxygen (red), lithium (red), iron, (brown) and titanium (Ti). Octahedral polyhedra surround TM sites aid in visualizing Li networks.

4.3 Understanding Charge Mechanisms

Understanding the contributions of the proposed electrochemical mechanisms is of importance due to the excess capacity which can be gained. The $x = 0.21$ material yielded a first charge capacity of 234 mAh/g. If the present structural and electrochemical mechanisms responsible for the poor reversible capacity of only 139 mAh/g and subsequent capacity loss over many cycles can be understood, designing similar disordered materials utilizing inexpensive and abundant elements may be feasible.

By following a protocol similar to McCalla *et al.*, $x = 0.13$ 800°C cells were cycled over different voltage ranges. Cells were cycled to 4.1 V, 4.2 V, 4.4 V and 4.6 V. The cell at 4.2 V was then cycled to 4.3 V after the first cycle. The results are shown in Figure 4.10 along with the proposed "charge mechanism regions", which are almost identical to McCalla's work.

The cell charged to 4.1 V had very little capacity, however exhibited a very small 3.8 V plateau, as well as a 2.7 V Fe reduction plateau. The 4.2 V cell had a very low reversible capacity. The voltage region up to 4.2 V therefore contained a large portion of the irreversible processes present. When the cell was then charged back to 4.2 V it exhibited higher capacity than the previous discharge from 4.2 V. When then charged to 4.3 V, almost all of the excess capacity between 4.2 – 4.3 V was reversible. This agrees with the theory previously proposed, in which after the first de-intercalation of 0-TM sites, TM atoms find a sort of "equilibrium" after migrating to fill emptied 0-TM regions and do not cause as significant irreversible changes to the networks. The 4.2 – 4.3 V region contained a significant amount of reversible $O^{2-/1-}$ due to the larger 3.8 V plateau during discharge as well as $Fe^{3+/4+}$. The 4.4 V cell did not yield any more oxygen reduction than the 4.3 V

charge, so reversible oxygen charge compensation is not likely above somewhere between 4.3 and 4.4 V. The 4.4 V cell also contained more reversible Fe redox. The 4.6 V cell had less reversible oxygen compensation and a higher reversible Fe redox than all other cells. The 4.6 V cell also contained a small $Fe^{3+/2+}$ plateau at 2.3 V, which seemed to occur only when charged above 4.4 V. This may have been due to an oxygen release process and slight reduction of Fe during the high voltage range of the charge. This was also observed in the 700°C and 800°C series in the high capacity cells, so it may have been a consequence of an excess of oxygen compensation.
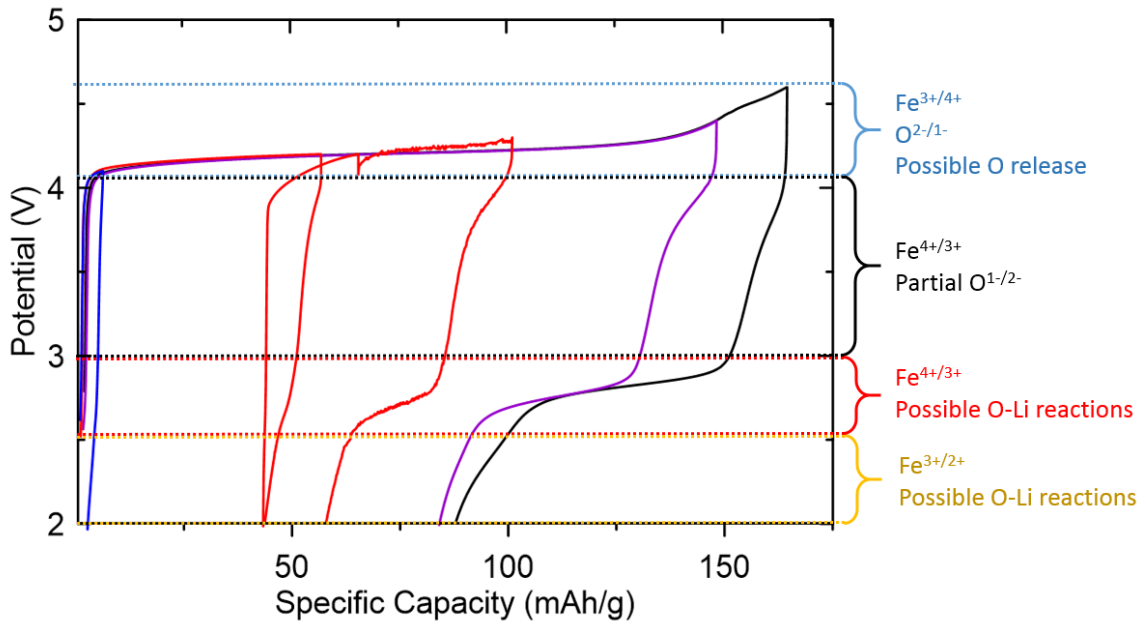
Figure 4.10: Speculated mechanisms in *x* = 0.13 cells cycled to different voltage cut-offs. The noise after the first charge of the red cell was due to a power trip causing a fault in one of the charger controllers.

These results suggest that in the first portion of the charge up to 4.2 V there was very little capacity due to reversible electrochemical processes. After 4.2 V a large portion of the capacity is reversible. Partial reversible oxygen redox was most likely present from 4.1 to 4.3 V, however irreversible oxygen compensation *via* redox or release may occur

above 4.3 V as well. Reversible $Fe^{3+/4+}$ was also observed at higher potentials above 4.2 V. Unfortunately this means lowering the voltage cut-offs would increase the irreversible capacity for this material and cycling above 4.5 V is necessary to increase $Fe^{3+/4+}$ capacity, yet causes oxygen release along with other detrimental changes. In the following chapter the TM contributions to capacity and the oxygen charge compensation mechanism is shown using *ex-situ* and pristine material XAS. These features are discussed in order to support the previous discussions on electrochemical contributions at different states of charge.

Chapter 5: Pristine and Charge Mechanism X-ray Absorption Studies

5.1 Pristine Material XAS

Section 2.6 outlined the experimental procedure at the SXRMB beam line at the CLS synchrotron. The obtained K-edge data was normalized and processed for qualitative analysis using the Athena software package.[53] Fluorescence detection is typically able to measure absorption on the order of $1 - 2$ μm from the surface of a particle in the hard X-ray region and $100 - 200$ nm in the soft X-ray region.[51,65] Figure 5.1 shows SEM images of $x = 0.00$, $x = 0.09$ and 0.28 samples. The particle size in each sample ranges between ~300 nm to several μm at higher x. Fluorescence detection was therefore sufficient to characterize into the bulk sample, not just the surface.
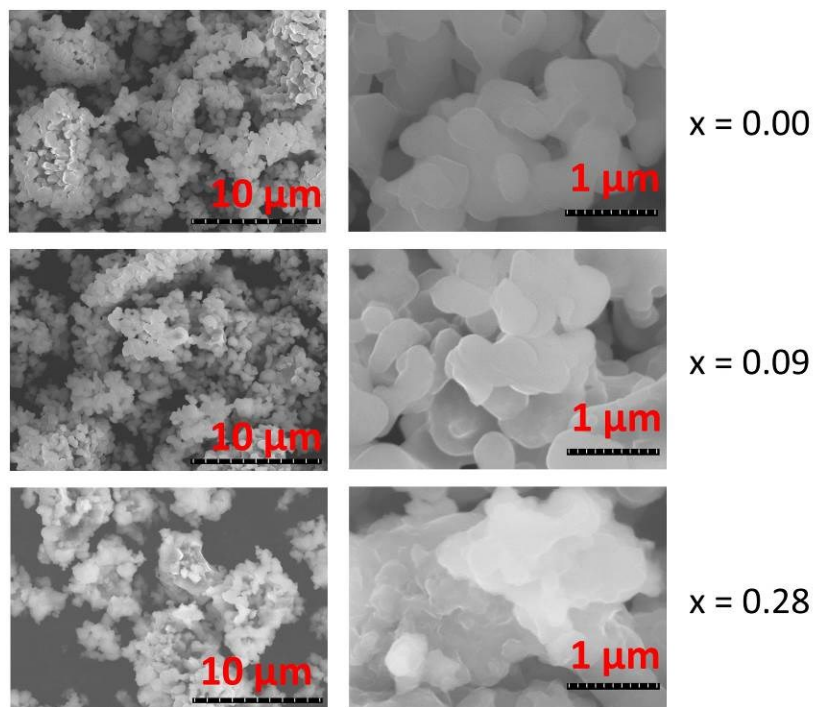

Figure 5.1: SEM images of pristine samples using the Hitachi S-4700 SEM.

The XANES regions of the Fe and Ti K-edges are shown in the left panels of Figures 5.1a and b respectively, and the R-space transformed EXAFS can be seen in the right panels. The K-edge positions and features in Fe and Ti were due to core 1s transitions to the unoccupied 4p states in the conduction band, near the Fermi energy, and are sensitive to oxidation state change.[51,66] The XANES region for both TMs showed no shift in edge energy with a change in composition, and were consistent with Fe^{3+} (7121 eV) and Ti^{4+} (4976 eV) reference positions found in literature.[67,68] As x increased there was a slight shift to higher energy in the edge peak, which is associated with 1s to continuum states above the ionization energy, suggesting stronger or shorter bond lengths with increasing x.[65,66] This correlated to XRD fitting discussed in Section 3.2, in which lattice parameters decreased with increasing x. The similarities in the Fe K-edges and pre-edges between samples indicated there was very little, if any local atomic and electronic structure differences between samples. Pre-edge features are due to formally forbidden 1s to unoccupied 3d state transitions through a quadrupole mechanism when 4p/3d mixing occurs, which is typical in high oxidation state transition metals.[69] In the Ti edge, the pre-edge peak labelled "1" in Figure 5.2b therefore could have increased with x due to octahedral distortion of Ti sites, as well as shorter metal to oxygen bonding.[51,66,70] The shoulder on the rising edge of the Ti edge was due to the "shakedown" process, in which a 1s-4p transition causes a relaxation to an excited state and a subsequent charge transfer through a TM-O bond.[66,71] As the lattice shrinks when x increased, this shoulder decreased in intensity, also consistent with shorter, stronger TM-O bonds.

EXAFS transformed into R-space can be interpreted as somewhat of a superposition of the radial distribution of atoms in a structure around a specific element site. Figure 5.3

demonstrates the R-space transformed EXAFS for the $x = 0.00$ Fe sample. The inset in

Figure 5.3 describes distances to certain atoms (in three dimensions) and indicates their

position in the R-space plot. Intensity is influenced by the atomic number, Z (higher Z =

more intensity), of the atoms in each radial "shell", the distance, and number of atoms in

the shell.[51] Typically in normal experimental conditions the first two to four shells can be

accurately modelled in EXAFS data. The first peak is due to the first TM-O shell around

the TM site. The second shell is due to metal-metal (M-M) distances (Fe, Ti and Li). After

these shells multiple scattering may occur, in which photoelectrons scatter off multiple

atoms. This changes the effect of the interference with other photoelectron waves and

causes difficulty fitting and characterizing data.[51,72]

In a disordered structure the M-M bond peaks at both TM edges should exhibit the

same behavior since the distribution of metals around both Ti and Fe should be random.

Therefore the local Li and TM distribution should be identical once averaged over every

site. In Figure 5.2 as x increased, the average Z in each shell decreased and each M-M

peak decreased proportionally in both Ti and Fe R-space. Peaks also shifted to lower R,

again corresponding to a shift to smaller lattice parameters with higher x. These findings

support the trends found in the D-5000 XRD data refinement.
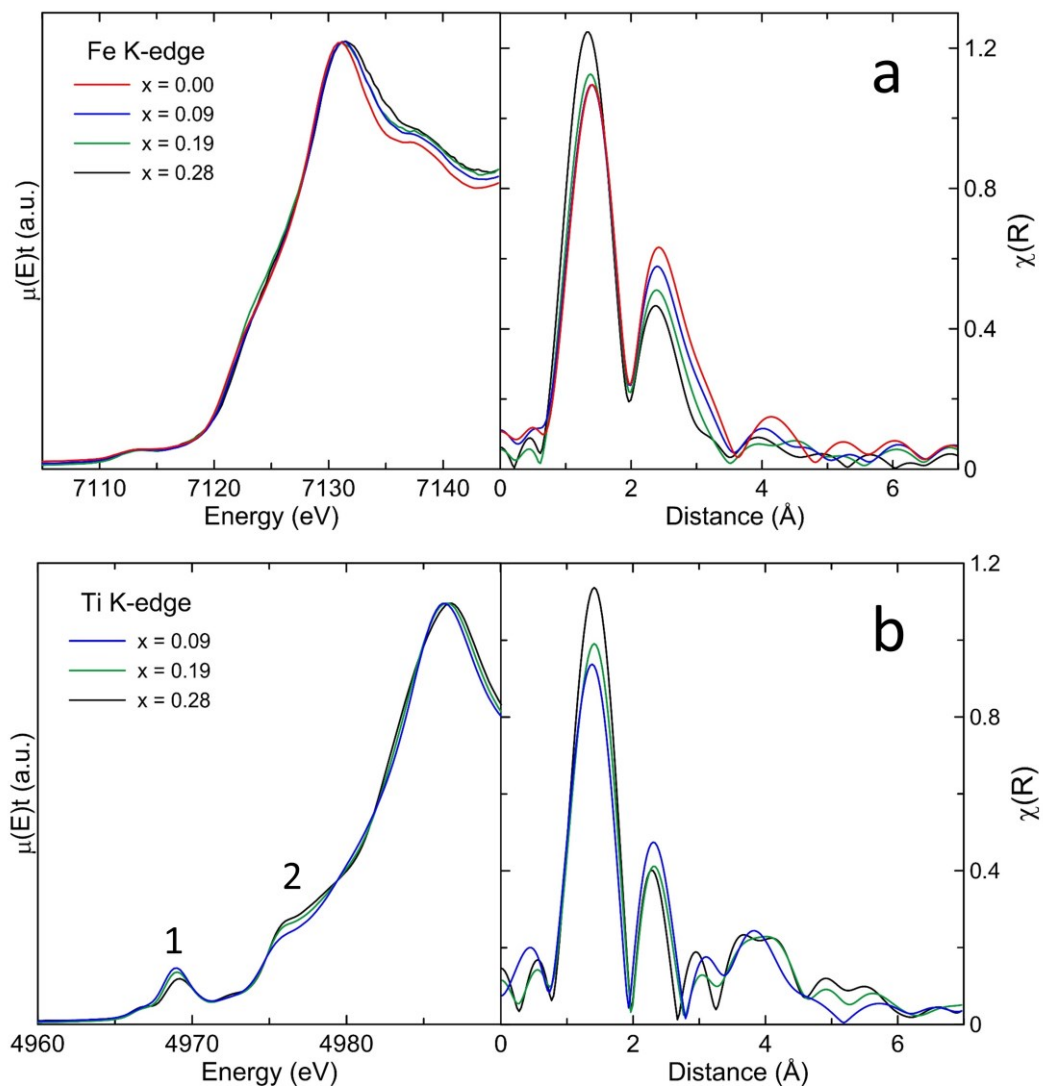
Figure 5.2: a) Fe and b) Ti K-edge XAS results. Left panels indicate XANES regions and right panels contain R-space data. Peak 1 in b) shows the drift in the Ti pre-edge and the shake-down shoulder is labelled at 2.
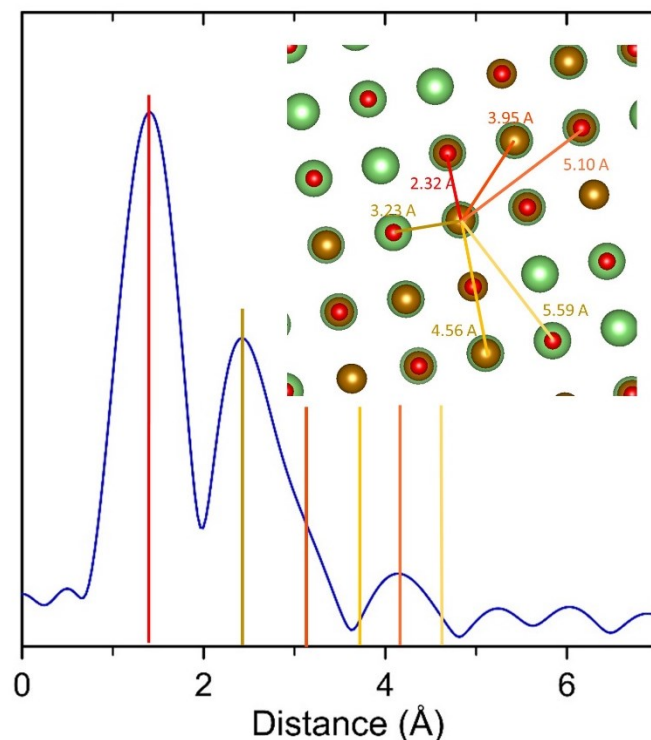
Figure 5.3: Example R-space EXAFS data demonstrating different distances (to multiple shells in three dimensions). Distances do not correlate to actual bond distance due to element specific phase shift. Oxygen bonds are shown in red/orange and M-M bonds in yellow/gold. Metal bond data after the third shell was affected by poor Fe signal.

The pristine K-edge data can be used in future work in order to understand EXAFS modelling of disordered structures. Calculations and refinement of EXAFS should be done in order to determine electronic and local structural mechanisms. Due to potential structural changes during cycling, a well understood pristine model must be developed before SOC studies can be understood. This modelling may be used to monitor local atomic behaviour during cycling in *in-situ* or *ex-situ* (SOC) studies in order to understand reversible and irreversible changes during the first charge-discharge as well as over long term cycling.

93

5.2 *Ex-situ* XANES Analysis

5.2.1 Charge States

Voltage curves for cells studied in this experiment are shown in Figure 4.3. Due to lower cycling temperatures (~19°C *vs.* 40°C) capacities were not as high as cells cycled on Moli systems at Dalhousie. Voltage curves between cells cycled at the CLS were consistent. Jagged steps in the voltage curves in Figure 4.3 are due to the low precision current supply used in the CLS charger system (Neware). SOC was determined by the cell voltage curve instead of the capacity due to the difference in capacities between CLS and Dalhousie data. All SOC values were also approximated to ~5% due to the polarization between both data sets.

Two cells were destroyed during disassembly. Cell 5, labelled "5 V hold" was set to cycle for 60 hours at C/60 including a discharge due to the lower expected capacity, however only charged to 5 V and was held. The charging system had a maximum voltage reading of 5 V and reported a charging current of approximately C/80 for 3 hours after reaching 5 V, so the cell may have cycled well above 5 V. It was included in analysis to examine Fe and O behaviour at high voltages.

Metal L-edges were measured but were not useful in order to characterize electrochemical processes. Metal K-edges should be measured in future work in order to obtain meaningful results for *ex-situ* studies.
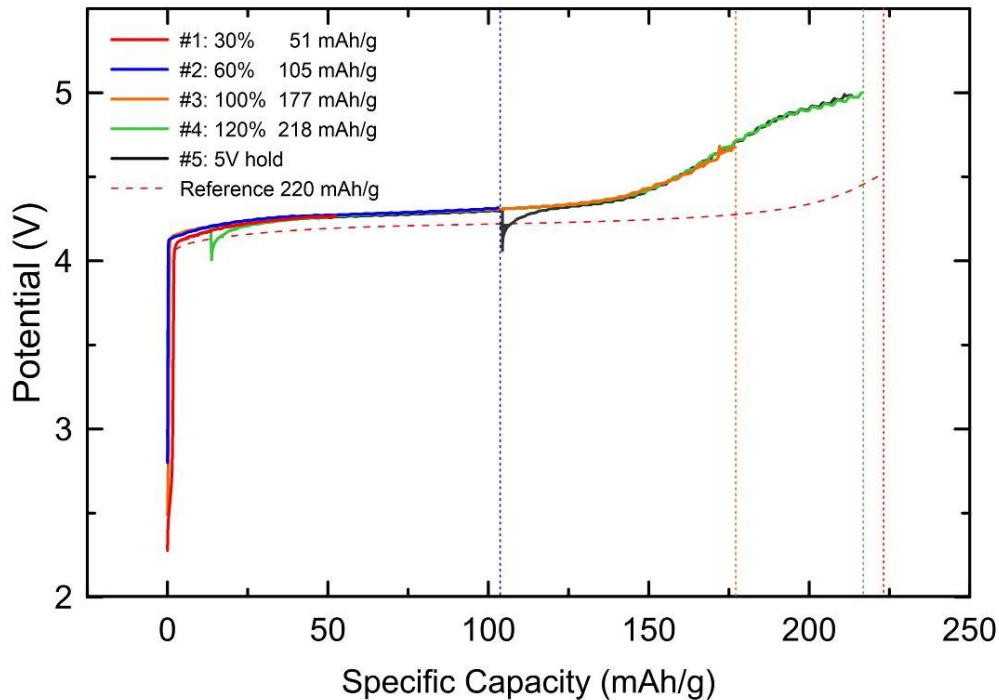
Figure 5.4: Voltage curves for cells cycled to various SOCs for *ex-situ* XAS studies. The dotted red line is the Moli charger data for the $x = 0.19$ material, also shown in Section 5.2.

5.2.2 Oxygen K-Edge

Oxygen K-edge data was obtained in attempt to observe and characterize oxygen charge mechanisms during charge. The oxygen K-edge contained many features, particularly in TEY data due to complex chemical reactions occurring at the surface of the electrode material. TEY in the oxygen K-edge region is capable of probing approximately 5 – 10 nm into the sample, therefore may not be used to characterize bulk electrochemical mechanisms but may give insights into surface reactions.[65] If electrodes were not rinsed well before measurement or were exposed to air in unstable states there may have been excess lithium salts, carbonates, oxides, *etc.* on the surface. These complex features would be most noticeable after the edge peak due to a large variation in bond types, strengths and orbital hybridizations.[73,74] Any significant change in the pre-edge or edge features however

could be attributed to an $O^{2-/1-}$ oxidation-like transition, and was most likely to be seen in in the bulk of the structure (FY spectra) due to the complex surface chemistry. It was hypothesized this process would result somewhere between 4.1 and 4.3 V due to the results discussed in Section 4.3. The O K-edge data is shown in Figure 5.7. Each edge was normalized to the pre-edge background only to compare relative magnitudes of features.

In the FY data shown in Figure 5. the two K-edge peaks labelled "1" and "2" increased and decreased with increasing SOC, respectively, consistent with being bonded to higher TM oxidation states.[75] After 60% SOC, a very pronounced edge feature was observed in the FY spectra, indicating a change in electronic structure. This feature however appeared at a lower energy than the K-edge, however a typical change to a higher oxidation state should correspond to a shift to higher energy, as observed in transition metals. Little O K-edge *ex-situ* oxygen compensation work on Li-ion batteries exhibiting similar features could be found in the literature, however this feature was believed to have been caused by a known, mechanism called a "negative charge transfer process", which induces a 2p hole in oxygen, effectively changing the oxidation state.[76] Work by Yoon *et al.* demonstrated a K-edge shift to slightly lower energy at high delithiation states of NMC 1:1:1, compensating for little electrochemical activity of Co in the material. TM atoms at high oxidation state, such as Fe^{4+} and Ti^{4+} "resist" having a higher valence state but may still allow for lithium to leave the system by interacting with oxygen. When charge compensation occurs, instead of having the former electron configuration of (for example) $d^n p^6$, the TM electron configuration still favours to maintain the lower oxidation state but may change electron configuration, such as $d^{n+1} p^5$ and as a consequence causes oxygen 2p holes to form.[76,77] This means during the O compensation mechanism oxygen is in a lower

energy state due to the 2p holes, rather than in metal oxidation in which the core levels shift to lower energy with increasing oxidation state causing a higher shift in edge energy. This process would account for the lower energy edge feature and has been seen in NiO and $Li_xNi_{(1-x)}O$ "hole doped" materials with very similar O K-edge feature at the same energy, the former shown in Figure 4.6.[76] This process is believed to have led to the observed charge compensation.

No edge feature was observed in TEY data, consistent with predictions. The 60% and 120% SOC cell had nearly identical behaviour, and the 100% SOC cell contained slightly less of an $O^{2-/1-}$ edge feature. The 5 V hold cell showed even less $O^{2-/1-}$, consistent with results in Section 4.3 in which very little reversible oxygen redox capacity was observed, due to the oxygen release process. The 30% SOC cell, which was assumed to have been shorted due to the low "1" peak in TEY data attributed to low TM oxidation states as well as a large Fe^{2+} peak in the Fe L-edge data, did not contain any visible $O^{2-/1-}$. It was not determined whether this was due to the shorting process or that O^{1-} does not occur until after 30% SOC. Most FY measurements were not greatly affected by the shorting of the cell, however this was not enough evidence to confidently claim $O^{2-/1-}$ did not occur in the first 30% of charge. This data would aid in understanding the large irreversible capacity found from 0% SOC to 4.3 V in Section 4.3. If no $O^{2-/1-}$ was present in the first 30% of charge, most or all irreversible capacity in this region would have originated from irreversible TM migration network blocking or structural changes. Future work should analyze the lower V region (4.0 – 4.3 V) using smaller voltage increments and duplicate cells in case of malfunction. The number of cells made in this experiment was limited by time and facilities at the CLS.
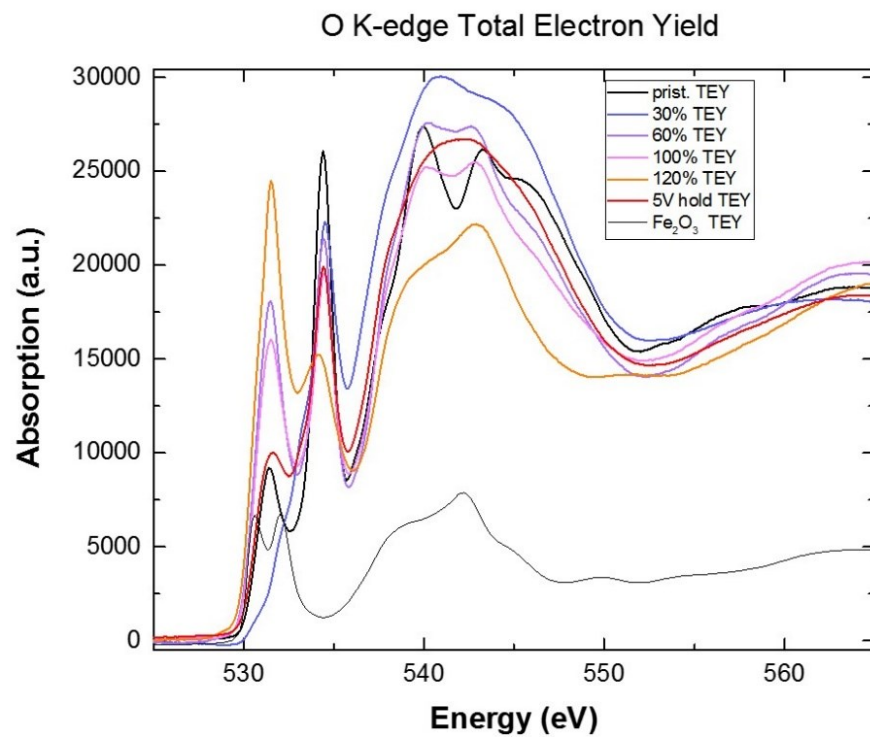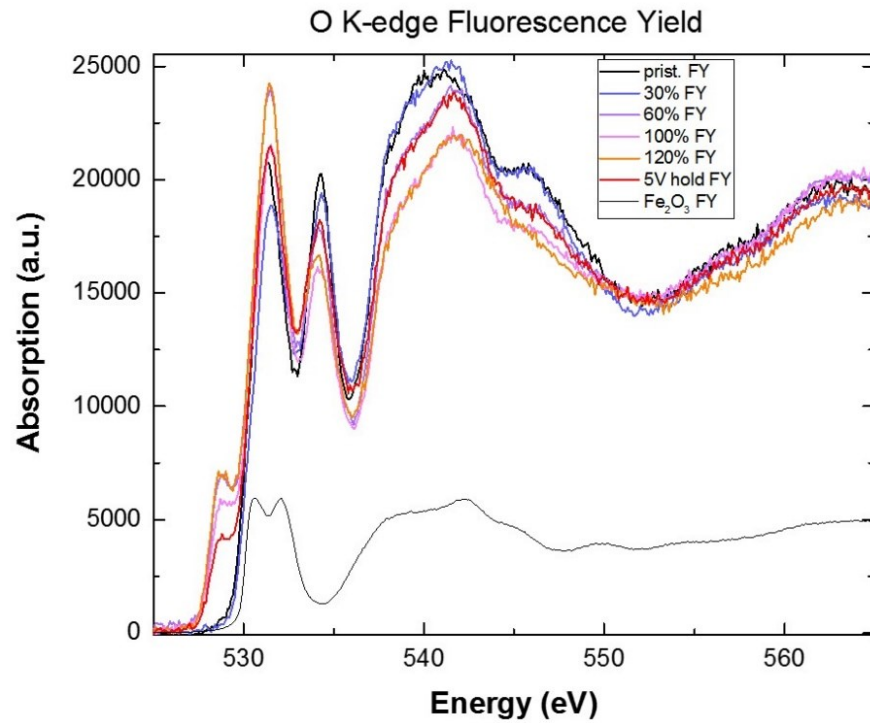
Figure 5.5: FY (top) and TEY (bottom) of Oxygen K-edge XANES. $O^{2-/1-}$ can be seen in the bulk (FY) but not near the surface.
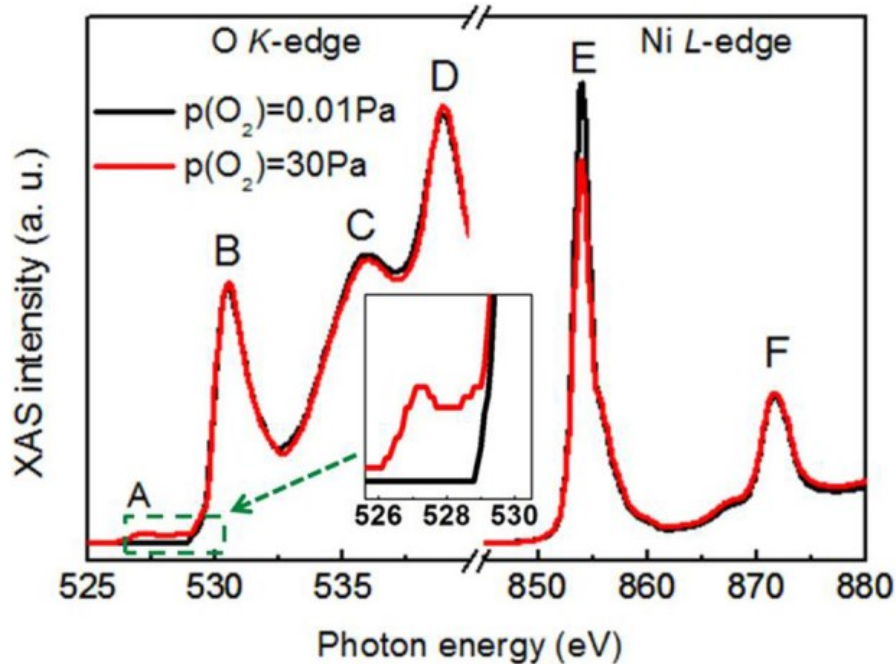
Figure 5.6: Oxygen K-edge of hole-doped NiO exhibiting O 2p holes creating an energy feature similar to that of the proposed charge compensation feature in the disordered *ex-situ* experiments. Reproduced with permission under the Creative Commons license from Peng H. Y. *et al. Sci. Rep.* (2012), **2**.

A charge compensation process due to possible $O^{2-/1-}$ redox was shown using *ex-situ* soft X-ray absorption techniques. This data as well as TM K-edges may be used to develop more in depth studies and further understand electrochemical processes. Due to $Fe^{3+/4+}$ and $O^{2-/1-}$ occupying the same voltage range during charge it is difficult to determine the contribution of each due to capacity, however XAS studies have provided a technique possibly capable of this.

Chapter 6: Conclusions and Future Work

6.1 Disordered Material Characterization and Performance

The $Li_{(1+x)}Ti_{2x}Fe_{(1-3x)}O_2$ ($0.00 \leq x \leq 0.28$) solid solution was synthesized at 700°C and 800°C. The x = 0.15 target composition was synthesized at 700°C, 750°C, 800°C, 900°C and 1000°C. Higher synthesis temperatures correlated with an increase in the degree of disorder between Li and TM layers (disorder). As x increased samples in the composition series contained lower disorder as well as smaller lattice parameters. Refinement of synchrotron XRD was used to confirm disorder levels but did not yield lattice parameters consistent with the D-5000 data obtained in-house.

Electrochemical performance of the 800°C composition series agreed with percolation theory models by Lee *et al.* for compositions with 0-TM lithium limited capacity, however demonstrated higher capacity than predicted due to $Fe^{3+/4+}$ oxidation.[27] Cells exhibited poor reversible capacity, likely due to TM migration during charge, causing irreversible changes to 0-TM networks. This was further supported by an increase in reversible capacity with increasing x. Pristine powder XANES data agreed with trends found in lattice parameters during XRD refinement of the D-5000 data. The excess capacity was determined to be caused by a $O^{2-/1-}$ redox process characterized by a low energy feature in the oxygen K-edge in *ex-situ* XAS studies of cycled cells which has been shown to be caused by oxygen 2p holes.[76]

Cycling cells to various SOCs yielded insight into voltage ranges responsible for different electrochemical mechanisms responsible for both reversible and irreversible capacity. These results were very consistent with work done on ordered Li_4SbFeO_2 which exhibited very similar electrochemistry to the disordered materials studied in this work.[63]

The results from this thesis demonstrate the potential for lithium-rich disordered materials, however also shows structural and electrochemical complications that must be considered in future studies and design of these materials. If disordered positive electrode materials can be well understood and designed in such a way as to maximize reversible capacity and structural stability, these materials may be able to achieve high energy density and low cost, making them suitable for use in next generation lithium ion batteries.

6.2 Future Work

In this work only the $Li_{(1+x)}Ti_{2x}Fe_{(1-3x)}O_2$ ($0.00 \leq x \leq 0.28$) solid solution with various degrees of disorder was tested. Though further studies on this material can be done, in order to prove this model can be applied to any disordered material, similar studies should be done on other systems. Solid solutions which allow for both redox limited capacity regions as well as systems that contain sufficient redox capacity and are only limited by 0-TM lithium should be explored. In order to design materials of future commercial interest, cost must also be minimized by designing materials with low raw materials and manufacturing costs, higher capacity, and longer lifetime.

6.2.1 Further Studies on the $Li_{(1+x)}Ti_{2x}Fe_{(1-3x)}O_2$ System

Cost of materials and synthesis may be explored by continuing to use techniques from this work, such as using cheap and abundant materials (TiO_2 and Fe_2O_3). Solid state synthesis is also a very scalable and cost effective process. Exploring the effect of different synthesis methods and chemistries will ultimately lead to the optimization of cost and performance. In this work the effect of different heating times and cooling rates on

ordering, other structural parameters, and electrochemistry were not explored. By quench-cooling materials from 800°C, a higher amount of disorder may be possible than observed in this work, and the amount of disorder may be controlled through both synthesis temperature and cooling rates. Decreasing heating times may also aid in reducing the observed lithium loss while increasing disorder by using higher temperatures.

Cycling these materials at different temperatures should also be explored in order to determine the effect of temperature on the kinetic properties of lithium percolation. It was unclear in the experimental conditions used in this study whether temperature, conductivity, or both played a role in the poor rate performance and reversible capacity. One such experiment could be to cycle many cells until stable capacity is reached. Cells could then be charged at 20°C, 40°C, and 60°C. At a fully charged state, cells at each temperature could be transferred into the other temperature boxes and discharged (with a reference cell remaining at each temperature). Trends in reversible capacity could then be found and thermal kinetic effects explored. Once temperature dependence is understood, rate performance may be explored at both optimal and non-optimal ambient cycling conditions.

Though relatively high capacities were reached by materials in this work, the $Li_{(1+x)}Ti_{2x}Fe_{(1-3x)}O_2$ series will not likely become commercially viable due to the poor reversible capacity and large hysteresis. Doping of this material with other transition metals in order to increase stability and reversibility of cation migration could be explored, as well as coating particles with carbon or other coatings in order to increase conductivity (improving rate capabilities), protect the surface and possibly decrease the large hysteresis.

Further work in O K-edge XAS studies in disordered materials will help understand and characterize SOCs at which oxygen redox and oxygen release charge compensation mechanisms occur, the reversibility of these processes, and what effect different TM choices have on the negative charge transfer process, which typically happens in heavier 3d transition metals (Mn, Fe, Co, Ni, Cu), explaining the charge compensation found in Li_2MnO_3.[30,77] Future preparation for *ex-situ* XAS work should be done either more consistently with the Dahn Lab procedures and instruments or performed in-house if possible in order to minimize discrepancy between electrochemical results. Smaller voltage steps should be measured and multiple cells at each capacity should be made to ensure reproducibility and a higher success rate in cell disassembly. Both charge and discharge should be explored in future studies in order to understand any reversible oxygen processes. Other compositions such as $x = 0.13$ should also be used for such studies, as the $x = 0.19$ material was not assumed to have any reversible O redox.

The current O, Ti and Fe K-edge data will be explored further in a more comprehensive study on the cycled electrodes. Ti and Fe K-edge XANES and EXAFS will be collected at the CLS and the electrodes will be used for ICP and XRD analysis in order to compare the remaining lithium content with the theoretical amount of lithium due to the observed capacity. Excess capacity can be attributed to oxygen compensation processes or electrolyte decomposition in the cells. XRD analysis of the cycled electrodes will give insight into potential structural changes during cycling. The low temperature cycling (room temperature) may create challenges in the analysis, due to the poor rate capability limiting the amount of utilized electrode. XRD patterns of the surface of the electrode as well as the average of surface and bulk, by grinding the material, should be collected in

case of phase transitions occurring during charge. Similar surface and bulk sampling should be used for ICP analysis. XANES simulations of both O and TM K-edges should be done in order to demonstrate an agreement between the proposed experimental mechanisms and theory. Models of the structure at each charge state can be made using ICP and XRD results of charged electrodes. Software such as ARTEMIS, FDMNES and Wien2K may be used in order to carry out XANES and EXAFS simulations.[53,78,79] Difficulties will arise in computing sufficiently large cluster sizes while controlling other calculation constraints in order to reduce computation time, as well as modelling the electron configuration of Fe and O at various states of charge. By comparing lithium composition, the electrochemically active $Fe^{3+/4+}$ and inactive Ti^{4+} K-edge XANES, electrochemical data, structural data from XRD and EXAFS and XAS simulations, a more complete understanding of the electrochemical role of oxygen charge compensation may be achieved. Once this process has been characterized, future XAS work using many structures and chemistries exhibiting oxygen charge compensation may be studied and understood.

In-situ XRD measurements are also planned for the $x = 0.19$ material in order to investigate possible phase changes, structural stability and reversibility during the first cycles, as well as after multiple cycles. A coin cell with a beryllium window acting as the positive electrode current collector will be used. This type of measurement was attempted during this work, however no changes were observed and the capacity of the cell was much lower than observed during electrochemical testing discussed in this work (~40%). This may have been due to the poor conductivity of the material, poor cell construction creating a poor electrode coating on the Be window, leaks in the cell casing, or connection of the

cell causing a short. Future *in-situ* cells must be made carefully and charged at a very low rate due to the room temperature conditions in the XRD charging apparatus.

Due to lithium loss during heating, it was possible that lithium vacancies were formed in these materials. Vacancies may aid in the reversibility of structural changes by providing excess unoccupied networks. When transition metal migration occurs, vacant sites may provide additional pathways to blocked networks. Studies to investigate the effects of vacancies may be possible by inducing lithium loss with different heating times. Samples may then be characterised using ICP-OES to determine lithium content, XRD to determine unit cell volume and theoretical density and pycnometry to measure the actual density of the materials. Electrochemical measurements may then be used to observe any changes to electrochemistry, primarily to the reversible capacity.

Finally, further studies of the amorphous-like background in disordered materials could lead to better XRD fitting and understanding of short range ordering. Low levels of ordering are difficult to fit due to the relative orders of magnitude of the (003) peak and background, so high resolution XRD is needed to minimize uncertainty in fitting.

6.2.2 Other Compositions

The $Li_{(1+x)}Ti_{2x}Fe_{(1-3x)}O_2$ solid solution was found to approximately agree with the theory by Lee *et al.*, however other disordered systems should be explored. Various synthesis methods and combinations of transition metals can be used in order to confirm the model further and explore charge compensation methods for other systems.

In order to increase capacity, TM species which have multiple oxidation states which allow for more 0-TM Li to be utilized by redox reactions must be understood. Possible

TM choices include Cr^{3+} and Mo^{4+}, which Lee *et al.* only showed one composition that agreed with theory. Other choices could include Nb^{3+}, V^{3+}, and Ni^{2+}. A separate experiment done during the course of this thesis work may show some $V^{3+/5+}$ in ordered $Li_{1.14}Ti_{0.29}V_{0.57}O_2$ using *in-situ* XAS techniques with good reversible capacity. The effect of V-doping on $Li_{(1+x)}Ti_{2x}Fe_{(1-3x)}O_2$ or similar disordered materials could be explored in order to maximize 0-TM and reversible capacity in these materials. An example of the charge-discharge data for $Li_{1.14}Ti_{0.29}V_{0.57}O_2$ is shown in Figure 6.1. *In-situ* XANES measurements will be modelled in order to determine the oxidation states of V during cycling and the reversibility of V redox. This material exhibited very reversible capacity once cycled to a low voltage cut off of 0.5 volts, demonstrating anodic properties like that of other Ti and V containing negative electrode materials. Dopants such as vanadium, however typically present in layered materials, may increase the theoretical and reversible capacity as well as rate capability in disordered materials. Work by Ren *et al.* demonstrated disordered $Li_2V_{(1-x)}Cr_xO_2F$ with up to 400 mAh/g and 70% capacity retention over 60 cycles.[80] By exploring the effects of other TM dopants on disordered oxides and oxyfluorides such as these materials, materials with high capacity and stable cycling may be possible.

These future materials may also contain various degrees of disorder, and the effect of disorder on irreversible capacity can be explored both lithium and redox limited systems. If slightly ordered structures can be shown to improve or provide acceptable cycling and rate performance, dopants and TMs choices which exhibit preferential ordering of the structure, such as Ti in this work, can be used to control structural stability while still increasing capacity (in the case of electrochemically active TMs) and increasing lifetime.
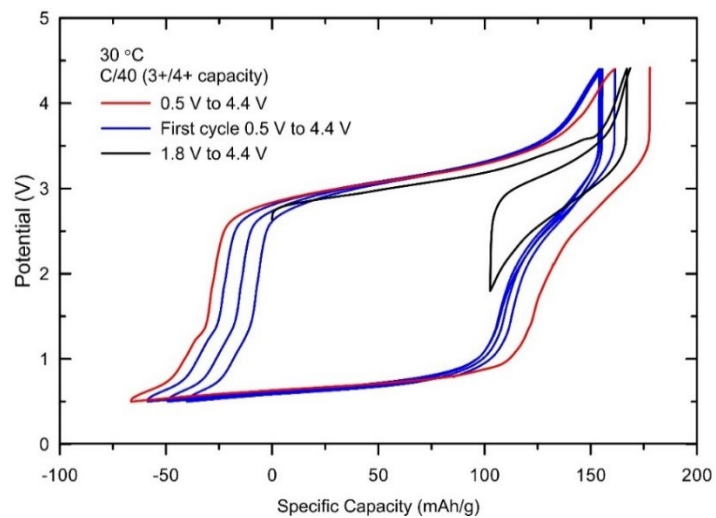
Figure 6.1: Charge-discharge profile for $Li_{1.15}Ti_{0.29}V_{0.56}O_2$ with up to 248 mAh/g discharge capacity during low voltage cycling. Theoretical capacity due to $V^{3+/4+}$ was 180 mAh/g.

References:

(1)   Canadian Vehicle Survey: Quarterly: Table 3-1 — Estimates of number of vehicles in scope for Canada — by type of vehicle and jurisdiction http://www.statcan.gc.ca/pub/53f0004x/2009004/t058-eng.htm (accessed Jun 4, 2015).

(2)   Canadian Vehicle Survey: Quarterly: Table 4-1 — Estimates of vehicle-kilometres for Canada — by type of vehicle and jurisdiction http://www.statcan.gc.ca/pub/53f0004x/2009004/t071-eng.htm (accessed Jun 4, 2015).

(3)   Government of Canada, N. R. C. Average Retail Prices in Canada | Energy Sources http://www2.nrcan.gc.ca/eneene/sources/pripri/prices_bycity_e.cfm?PriceYear=0& ProductID=1&LocationID=66,39&dummy=#PriceGraph (accessed Jun 4, 2015).

(4)   Ford - Cars, SUVs, Trucks & Crossovers | Ford Vehicles | The Official Site of Ford Vehicles | Ford.com http://www.ford.ca/cars/fusion/2015/ (accessed Jun 4, 2015).

(5)   Alternative Fuels Data Center: Maintenance and Safety of Hybrid and Plug-In Electric Vehicles http://www.afdc.energy.gov/vehicles/electric_maintenance.html (accessed Jun 21, 2015).

(6)   Electric Vehicles 35% Cheaper To Maintain Than Comparable Cars http://www.2050publications.com/electric-vehicles-35-cheaper-to-maintain-than-comparable-cars/ (accessed Jun 21, 2015).

(7)   EPRI | EPRI Study Shows that Lifetime Cost of Ownership of Electric Vehicles is Comparable with Conventional Vehicles http://www.epri.com/Press-Releases/Pages/EPRI-Study-Shows-that-Lifetime-Cost-of-Ownership-of-Electric-Vehicles-is-Comparable-with-Conventional-Vehicles.aspx (accessed Jun 21, 2015).

(8)   Model S | Tesla Motors http://www.teslamotors.com/models (accessed Jun 4, 2015).

(9)   BMW i3 : At a glance http://www.bmw.com/com/en/newvehicles/i/i3/2013/showroom/index.html (accessed Jun 4, 2015).

(10)   2015 Spark EV Electric Vehicles | Chevrolet http://www.chevrolet.com/spark-ev-electric-vehicle.html (accessed Jun 4, 2015).

(11)   2015 Focus Electric | View Focus Electric Highlights | Ford.com http://www.ford.com/cars/focus/trim/electric/ (accessed Jun 4, 2015).

(12)   Brodd, R. J. *Meet. Abstr.* **2010**, *MA2010-03* (1), 649–649.

(13) Takahashi, Y.; Tode, S.; Kinoshita, A.; Fujimoto, H.; Nakane, I.; Fujitani, S. *J. Electrochem. Soc.* **2008**, *155* (7), A537–A541.

(14) Chen, Z.; Dahn, J. R. *Electrochem. Solid-State Lett.* **2004**, *7* (1), A11–A14.

(15) Johnson, C. S.; Li, N.; Lefief, C.; Thackeray, M. M. *Electrochem. Commun.* **2007**, *9* (4), 787–795.

(16) Shaju, K. M.; Rao, G. V. S.; Chowdari, B. V. R. *Electrochimica Acta* **2002**, *48* (2), 145–151.

(17) Yabuuchi, N.; Ohzuku, T. *J. Power Sources* **2003**, *119*, 171–174.

(18) McCalla, E.; Rowe, A. W.; Shunmugasundaram, R.; Dahn, J. R. *Chem. Mater.* **2013**, *25* (6), 989–999.

(19) Brown, C. R.; McCalla, E.; Watson, C.; Dahn, J. R. *ACS Comb. Sci.* **2015**.

(20) McCalla, E.; Dahn, J. R. *Solid State Ion.* **2013**, *242*, 1–9.

(21) Rowe, A. W.; Camardese, J.; McCalla, E.; Dahn, J. R. *J. Electrochem. Soc.* **2014**, *161* (9), A1189–A1193.

(22) Lu, Z. H.; MacNeil, D. D.; Dahn, J. R. *Electrochem. Solid State Lett.* **2001**, *4* (11), A191–A194.

(23) Li, J.; Klöpsch, R.; Stan, M. C.; Nowak, S.; Kunze, M.; Winter, M.; Passerini, S. *J. Power Sources* **2011**, *196* (10), 4821–4825.

(24) Shigemura, H.; Tabuchi, M.; Sakaebe, H.; Kobayashi, H.; Kageyama, H. *J. Electrochem. Soc.* **2003**, *150* (5), A638–A644.

(25) Tabuchi, M.; Nakashima, A.; Shigemura, H.; Ado, K.; Kobayashi, H.; Sakaebe, H.; Tatsumi, K.; Kageyama, H.; Nakamura, T.; Kanno, R. *J. Mater. Chem.* **2003**, *13* (7), 1747–1757.

(26) Obrovac, M. N.; Mao, O.; Dahn, J. R. *Solid State Ion.* **1998**, *112* (1–2), 9–19.

(27) Lee, J.; Urban, A.; Li, X.; Su, D.; Hautier, G.; Ceder, G. *Science* **2014**, *343* (6170), 519–522.

(28) Urban, A.; Lee, J.; Ceder, G. *Adv. Energy Mater.* **2014**, *4* (13), 1400478.

(29) Newman, M. E. J.; Ziff, R. M. *Phys. Rev. E* **2001**, *64* (1), 016706.

(30) Robertson, A. D.; Bruce, P. G. *Chem. Mater.* **2003**, *15* (10), 1984–1992.

(31) Twu, N.; Li, X.; Urban, A.; Balasubramanian, M.; Lee, J.; Liu, L.; Ceder, G. *Nano Lett.* **2015**, *15* (1), 596–602.
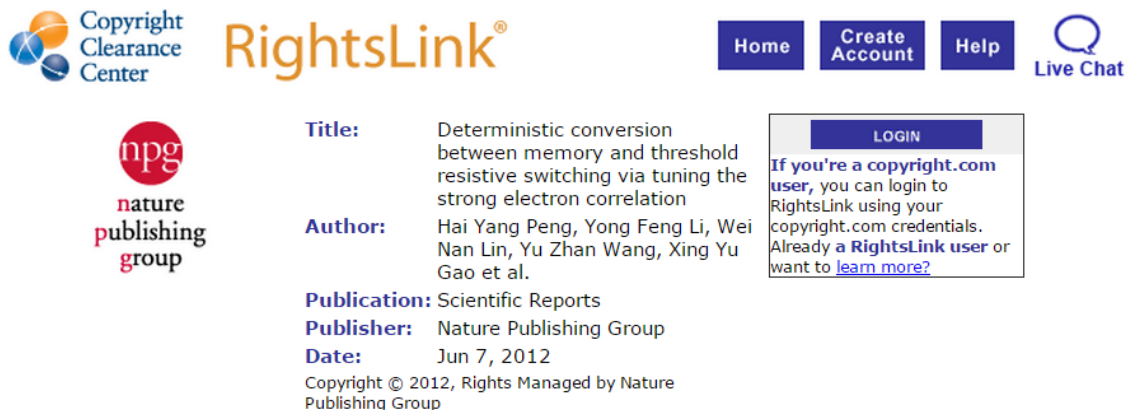
(32) Yabuuchi, N.; Takeuchi, M.; Nakayama, M.; Shiiba, H.; Ogawa, M.; Nakayama, K.; Ohta, T.; Endo, D.; Ozaki, T.; Inamasu, T.; Sato, K.; Komaba, S. *Proc. Natl. Acad. Sci.* **2015**, 201504901.

(33) Hou, X.; Jones, T., B. In *Encyclopedia of Analytical Chemistry*; John Wiley & Sons Ltd.: Chichester, 2000; pp 9468–9485.

(34) Optima 8000 ICP-OES Spectrometer | PerkinElmer http://www.perkinelmer.ca/en-ca/Catalog/Product/ID/OPTIMA8000 (accessed Jun 23, 2015).

(35) G. V. Samsonov. In *A Configurational Model of Matter*; Springer Science & Business Media, 2012; p 132.

(36) Keywords "field-emission electron gun" | Keywords "field-emission electron gun" | Glossary of TEM Terms | JEOL Ltd. http://www.jeol.co.jp/en/words/emterms/search_result.html?keyword=field-emission%20electron%20gun (accessed Jul 3, 2015).

(37) Reimer, L. *Transmission Electron Microscopy: Physics of Image Formation and Microanalysis*; Springer, 2013.

(38) Warren, B. E. *X-ray Diffraction*; Addison-Wesley: Massachusetts, 1969.

(39) Center for X-Ray Optics; Advanced Light Source. *X-Ray Data Booklet*; Lawrence Berkeley National Laboratory, 2009.

(40) Canadian Light Source / Centre Canadien de rayonnement synchrotron http://www.lightsource.ca/ (accessed Jun 29, 2015).

(41) Brian H. Toby, R. B. V. D. *J. Appl. Crystallogr.* **2013**, *46*, 544–549.

(42) Rietveld, H. M. *J. Appl. Chryst.* **1969**, *2*, 65–71.

(43) Cullity, B. D.; Stock, S. R. *Elements of X-ray Diffraction*; Prentice Hall, 2001.

(44) US Department of Commerce, N. NIST X-Ray Form Factor, Atten., and Scattering Database http://www.nist.gov/pml/data/ffast/index.cfm (accessed Jun 28, 2015).

(45) Peng, L.-M.; Ren, G.; Dudarev, S. L.; Whelan, M. J. *Acta Crystallogr. Sect. A* **1996**, *52* (3), 456–470.

(46) Sears, V. F.; Shelley, S. A. *Acta Crystallogr. Sect. A* **1991**, *47* (4), 441–446.

(47) Hunter, B. A. *International Union of Crystallography Commission on Powder Diffraction Newsletter* **1998**, *20*.

(48) Crystallography Open Database http://www.crystallography.net/ (accessed Jul 1, 2015).

(49) Wyckoff, R. W. G. *Crystal Structures*; Interscience Publishers, 1958.

(50) Whittingham, M. S. *Chem. Rev.* **2004**, *104* (10), 4271–4302.

(51) Agarwal, B. K. *X-Ray Spectroscopy: An Introduction*; Springer, 2013.

(52) Marr, G. V. *Handbook on Synchrotron Radiation*; North Holland: Amsterdam, 1987; Vol. 2.

(53) Ravel, B.; Newville, M. *J. Synchrotron Radiat.* **2005**, *12* (4), 537–541.

(54) 8.4. XAFS: Fourier Transforms for XAFS — larch 0.9.24 documentation http://cars.uchicago.edu/xraylarch/xafs/xafsft.html (accessed Aug 19, 2015).

(55) Groot, F. de; Kotani, A. *Core Level Spectroscopy of Solids*; CRC Press, 2008.

(56) Marks, T.; Trussler, S.; Smith, A. J.; Xiong, D.; Dahn, J. R. *J. Electrochem. Soc.* **2011**, *158* (1), A51–A57.

(57) Crystal Impact. *Match!*; Crystal Impact, 2013.

(58) ICDD Products - PDF-2 http://www.icdd.com/products/pdf2.htm (accessed Jul 6, 2015).

(59) Sakuda, A.; Takeuchi, T.; Okamura, K.; Kobayashi, H.; Sakaebe, H.; Tatsumi, K.; Ogumi, Z. *Sci. Rep.* **2014**, *4*.

(60) Lin, T.-Y.; Lin, S.-S.; Chen, S.-Y.; Shen, P. *CrystEngComm* **2015**, *17* (18), 3468–3477.

(61) Thorne, J. S.; Chowdhury, S.; Dunlap, R. A.; Obrovac, M. N. *J. Electrochem. Soc.* **2014**, *161* (12), A1801–A1805.

(62) Thorne, J. S.; Dunlap, R. A.; Obrovac, M. N. *J. Electrochem. Soc.* **2013**, *160* (2), A361–A367.

(63) McCalla, E.; Sougrati, M. T.; Rousse, G.; Berg, E. J.; Abakumov, A.; Recham, N.; Ramesha, K.; Sathiya, M.; Dominko, R.; Van Tendeloo, G.; Novák, P.; Tarascon, J.-M. *J. Am. Chem. Soc.* **2015**, *137* (14), 4804–4814.

(64) McCalla, E.; Abakumov, A.; Rousse, G.; Reynaud, M.; Sougrati, M. T.; Budic, B.; Mahmoud, A.; Dominko, R.; Van Tendeloo, G.; Hermann, R. P.; Tarascon, J.-M. *Chem. Mater.* **2015**, *27* (5), 1699–1708.

(65) Zhou, J.; Hong, D.; Wang, J.; Hu, Y.; Xie, X.; Fang, H. *Phys. Chem. Chem. Phys. PCCP* **2014**, *16* (27), 13838–13842.

(66) Atsushi Ito, Y. S. *J. Power Sources* **2011**, *196* (16), 6828–6834.

(67)   Lützenkirchen-Hecht, D.; Wagemaker, M.; van Well, A. A.; Frahm, R. *Phys. Scr.* **2005**, *2005* (T115), 390.

(68)   Peng, Y. H.; Xie, Z.; He, J. F.; Liu, Q. H.; Pan, Z. Y.; Cheng, W. R.; Wei, S. Q. *J. Phys. Conf. Ser.* **2013**, *430* (1), 012136.

(69)   Kuzmin, A.; Mironova, N.; Purans, J. *J. Phys. Condens. Matter* **1997**, *9* (24), 5277.

(70)   Sarangi, R. *Coord. Chem. Rev.* **2013**, *257* (2), 459–472.

(71)   DuBois, J. L. M.; Chemistry, S. U. D. of. *Application of x-ray absorption spectroscopy to O2-reactive metalloenzymes and inorganic complexes*; Stanford University, 2000.

(72)   Newville, M.; Ravel, B.; Haskel, D.; Rehr, J. J.; Stern, E. A.; Yacoby, Y. *Phys. B Condens. Matter* **1995**, *208–209*, 154–156.

(73)   Chen, J. G. *Surf. Sci. Rep.* **1997**, *30* (1–3), 1–152.

(74)   Zhou, J.; Hong, D.; Wang, J.; Hu, Y.; Xie, X.; Fang, H. *Phys. Chem. Chem. Phys.* **2014**, *16* (27), 13838–13842.

(75)   Zhou, J.; Zhou, X.; Li, R.; Sun, X.; Ding, Z.; Cutler, J.; Sham, T.-K. *Chem. Phys. Lett.* **2009**, *474* (4–6), 320–324.

(76)   Peng, H. Y.; Li, Y. F.; Lin, W. N.; Wang, Y. Z.; Gao, X. Y.; Wu, T. *Sci. Rep.* **2012**, *2*.

(77)   Khomskii, D. *Lith. J. Phys.* **1997**, *37*, 65.

(78)   Joly, Y.; Bunău, O.; Lorenzo, J. E.; Galéra, R. M.; Grenier, S.; Thompson, B. *J. Phys. Conf. Ser.* **2009**, *190* (1), 012007.

(79)   Blaha, P.; Schwarz, K.; Madsen, G. K.; Kvasnicka, D.; Luitz, J. 2001.

(80)   Ren, S.; Chen, R.; Maawad, E.; Dolotko, O.; Guda, A. A.; Shapovalov, V.; Wang, D.; Hahn, H.; Fichtner, M. *Adv. Sci.* **2015**, 1500128.

Appendix

Permissions for Figure 5.3

113